

LA-UR-18-28283 (Accepted Manuscript)

Metal Oxide Nanocomposites: A Perspective from Strain, Defect, and Interface

Chen, Aiping
Su, Qing
Han, Hyungkyu
Enriquez, Erik
Jia, Quanxi

Provided by the author(s) and the Los Alamos National Laboratory (2019-04-01).

To be published in: Advanced Materials

DOI to publisher's version: 10.1002/adma.201803241

Permalink to record: <http://permalink.lanl.gov/object/view?what=info:lanl-repo/lareport/LA-UR-18-28283>

Disclaimer:

Los Alamos National Laboratory, an affirmative action/equal opportunity employer, is operated by Triad National Security, LLC for the National Nuclear Security Administration of U.S. Department of Energy under contract 89233218CNA000001. By approving this article, the publisher recognizes that the U.S. Government retains nonexclusive, royalty-free license to publish or reproduce the published form of this contribution, or to allow others to do so, for U.S. Government purposes. Los Alamos National Laboratory requests that the publisher identify this article as work performed under the auspices of the U.S. Department of Energy. Los Alamos National Laboratory strongly supports academic freedom and a researcher's right to publish; as an institution, however, the Laboratory does not endorse the viewpoint of a publication or guarantee its technical correctness.



DOI: 10.1002/adma.201803241

Article type: Review

Metal Oxide Nanocomposites: A Perspective from Strain, Defect and Interface

Aiping Chen^{1*}, Qing Su², Hyungkyu Han¹, Erik Enriquez¹, and Quanxi Jia^{3,4}

¹ Center for Integrated Nanotechnologies (CINT), Los Alamos National Laboratory, Los Alamos, NM 87545, USA

² Nebraska Center for Energy Sciences Research, University of Nebraska-Lincoln, Lincoln, NE 68583, USA

³ Department of Materials Design and Innovation, University at Buffalo - The State University of New York, Buffalo, NY 14260, USA

⁴ Division of Quantum Phases and Devices, Department of Physics, Konkuk University, Seoul 143-701, South Korea

* Email: apchen@lanl.gov

Abstract

Vertically aligned nanocomposite (VAN) thin films with ordered two phases, grown epitaxially on substrates, have attracted tremendous interest in the past decade. These unique nanostructured composite thin films with large vertical interfacial area, controllable vertical lattice strain and defects provide an intriguing playground, allowing for the manipulation of a variety of functional properties of the materials via the interplay among strain, defect and interface. This field has evolved from basic growth and characterization to functionality tuning as well as potential applications in energy conversion and memory storage. Here, the remarkable progress achieved in vertically aligned nanocomposite thin films from a perspective of tuning functionalities through control of strain, defect and interface is summarized.

This is the author manuscript accepted for publication and has undergone full peer review but has not been through the copyediting, typesetting, pagination and proofreading process, which may lead to differences between this version and the [Version of Record](#). Please cite this article as [doi: 10.1002/adma.201803241](https://doi.org/10.1002/adma.201803241).

This article is protected by copyright. All rights reserved.

1 Introduction

Complex metal oxides, which show a variety of functional properties such as ferromagnetism, ferroelectricity, multiferroelectricity, superconductivity and ionic conduction, have attracted much attention in the past decades. These exotic physical properties arise from a complex hierarchy of competing interactions among spin, charge, orbital and lattice degrees of freedom. The development of advanced characterization techniques such as electron microscopy, neutron scattering, synchrotron radiation, high magnetic fields and others has enabled us to study the interactions among these degrees of freedom coupled with strain, defect and interface on functionality. Recent advances in thin film growth technologies such as pulsed laser deposition (PLD) and molecular beam epitaxy have facilitated the growth of high quality epitaxial heterostructures, superlattices and nanocomposites with certain controllability in strain, defect and interface.^[1-6] In the metal oxide films, the interplay between adjacent layers including substrate and film can be synergistically utilized to tune the functionality. Biaxial strain in epitaxial thin films plays a critical role in determining the physical properties of the materials, including magnetoresistance, magnetic anisotropy, ionic conduction and electric polarization. Using interface to induce emergent phenomena in metal oxide films is another research focus. Emergent interfacial functionalities such as two dimensional electron gas (2DEG) at SrTiO₃/LaAlO₃ interface,^[7] exchange bias in LaMnO₃/LaNiO₃ superlattices,^[8] colossal ionic conductivity in ZrO₂:Y₂O₃/SrTiO₃ (STO) multilayers,^[9] topological Hall effect at SrRuO₃/SrIrO₃ interface^[10] and anomalous Hall effect at SrMnO₃/SrIrO₃ interface^[11] often involve competing degrees of freedom at interfaces.^[12] Even in the mostly studied manganites La_xSr_{1-x}MnO₃ (LSMO) films epitaxially grown on STO substrates, different mechanisms have been proposed to explain the anomalous interfacial properties. For instance, epitaxial strain, interfacial chemistry, charge discontinuity, octahedral rotation and off-stoichiometry have been proposed to explain the observed experimental results.^[13-23] In order to understand 2DEG at oxide interfaces, different mechanisms such as cation off-stoichiometry,^[24] surface reconstruction,^[25] oxygen vacancies,^[26] cation intermixing^[27] and structural distortions^[28] have been proposed. It is clear that strain, defect and interface play critical roles in controlling the functional properties of heterostructures of metal oxides.

Vertically aligned nanocomposites (VANs) with vertical 1D structure (e.g., nanopillars, nanosheets, nanowires, *etc*) of one phase embedded in a film matrix of another phase, where the whole assembly is epitaxially grown on a substrate, have attracted much attention.^[29, 30] As shown in **Figure 1**, VANs exhibit several different characteristics from lateral heterostructures. First of all, a vertical lattice strain, stemming from the elastic coupling of two phases at the vertical interface, could exist in thick films. As we will discuss in this review article, such a vertical strain has been used to control functional properties in a variety of materials systems. In addition, owing to the unique growth

patterns of two different phases, VANs exhibit large vertical interface area which could be effectively used to enhance the interfacial functionalities such as ionic conduction and magnetoelectric coupling. Moreover, defects such as oxygen vacancy and cation off-stoichiometry introduced by the phase change across the vertical interfaces and the large vertical lattice strain can be also used to tune the functionalities. These unique features make VANs an interesting platform to study the critical roles of strain, defect and interface on functional properties in complex metal oxides. In addition, VANs have been recently explored as the platform for applications in electronics and energy conversion.

In this review article, section 2 gives a quick overview of strain engineering in lateral heterostructures. Section 3 focuses on strain engineering in VANs. A few critical issues including the origin of vertical strain, strain distribution and strain design principle in VANs are discussed in this section. Section 4 discusses the correlation among strain, defect and interface. It covers two important topics including microstructure formation resulted from competing strain energy and interfacial energy, and defects formation due to elastic interactions. Section 5 focuses on the tuning of functional properties of metal oxides based VANs by controlling strain, defect and interface. A variety of functional properties such as magnetic anisotropy, magnetotransport, ferroelectricity, magnetoelectric coupling, superconductivity, electric/ionic conduction and electrochemistry are discussed. Possible future research directions and challenges are discussed in section 6.

2 Mismatch and Strain

2.1 Lattice mismatch

During the growth of epitaxial heterostructures, the lattice constant difference between the film and the substrate could induce epitaxial biaxial strain. The lattice mismatch f of the simple cubic lattice is given by,

$$f = \frac{a_s - a_0}{a_0} \quad (1)$$

where a_s and a_0 are the unstrained lattice parameters of substrate and film, respectively. When $f \approx 0$, lattice-matched epitaxial heterostructure can be formed with a coherent interface which is similar to homoepitaxy. If the misfit can be maintained in the range of $0 < |f| < 7\%$, fully strained lattice is considered to be possible with a coherent interface. A film can be coherently grown on a substrate up to a critical thickness (h_c) where dislocations formation becomes energetically favorable.^[31] **Figure 2a** shows a coherent interface with atomically abrupt interface in LSMO/STO superlattices investigated by scanning transmission electron microscopy (STEM).^[32] The interface roughness strongly depends

on techniques and processing parameters used to grow the films. When $|f| > 7\%$, domain matching epitaxy (DME) is generally preferred.^[33] A lattice misfit f can be defined by the matching of m film planes with $m\pm 1$ substrate planes. This matching leaves a residual misfit (f_r), which is given by,

$$f_r = \frac{(m\pm 1)a_s - ma_0}{(m\pm 1)a_s} \quad (2)$$

where m is a simple integer. DME has been reported in many different systems including TiN/Si, AlN/Si, and ZnO/ α -Al₂O₃.^[34] In the STO/MgO system, the large lattice mismatch ($\sim 7.8\%$) between STO and MgO favors DME. As shown in Figure 2b, misfit dislocations, marked by red arrows, can be clearly seen at the film-substrate interface. It can be seen that 14 (020) STO lattices match with 13 (020) MgO lattices, resulting in a residual mismatch of 0.13%. To show these dislocations, geometric phase analysis (GPA) was applied. Figure 2c shows the edge dislocation cores in Bragg images obtained via applying GPA.^[35] The misfit dislocation spacing $d_s = \frac{a_0 \times a_s}{2(a_0 - a_s)}$, is estimated to be 26.9 Å which is consistent with 26.7 Å measured from the phase image.

2.2 Strain Engineering

Biaxial strain of several percent can be tolerated in thin film form. This epitaxial strain is not only a unique approach to tune and manipulate their functionalities but also an interesting approach to stabilize phases that are not stable under ambient condition. For instance, elastic strain engineering is one of the most interesting approaches to tune physical properties.^[36-43] Other approaches to manipulate the functional properties of thin films include chemical doping,^[44] interface engineering,^[19, 45-50] octahedral rotation,^[51-53] epitaxial stabilization, polarization doping^[54] and dimensional confinement.^[55-57] By carefully selecting substrates and/or buffer layers, different strain states can be achieved in materials in thin film form. By using ferroelectric substrates, functional properties of thin films can be tuned via ferroelectric phase transition, elastic strain and charge effect.^[58-60]

For isotropic films, the in-plane biaxial strain is given by,

$$\varepsilon_{xx} = \varepsilon_{yy} = \frac{a_{||} - a_0}{a_0} \quad (3)$$

The out-of-plane strain is given by,

$$\varepsilon_{zz} = \frac{a_{\perp} - a_0}{a_0} \quad (4)$$

where a_0 is the lattice parameter of unstrained film, $a_{||}$ and a_{\perp} are the in-plane and out-of-plane lattice parameter of the strained film on a given substrate. Under elastic deformation, the Poisson ratio ν of a strained film is given by,

$$\nu = \frac{\varepsilon_{zz}}{\varepsilon_{zz} - 2\varepsilon_{xx}} = \frac{a_{\perp} - a_0}{a_{\perp} + a_0 - 2a_{||}} \quad (5)$$

ν is found to be between 0.33-0.37 for manganite perovskite thin films.^[61] The Poisson ratio ν , a material character, can be also obtained by,

$$\nu = \frac{c_{12}}{c_{11} + c_{12}} \quad (6)$$

where c_{11} and c_{12} are elastic moduli of the film material.

Epitaxial strain gradually changes with film thickness in perovskite manganites. **Figure 3** shows reciprocal space mapping or RSM (103) of $\text{La}_{0.7}\text{Ca}_{0.3}\text{MnO}_3$ (LCMO) films on STO (001) substrates. It captures the gradual strain relaxation process with increasing film thickness in manganite thin films. When the film is very thin, the interface is coherent with $a_{||} = a_s$ (Figure 3a). Therefore, the absolute number of in-plane biaxial strain in Eq. 3 is the same as lattice mismatch in Eq. 1. With increasing of film thickness, the top layer (above the critical film thickness of h_c) of the film starts to relax (e.g., via misfit dislocations) and the in-plane lattice parameter starts to deviate from the substrate (Figure 3b). Further increase of film thickness results in a full strain relaxation of the top layer (Figure 3c). As proposed in People-Bean model, the elastic strain energy is stored in the film and it increases with film thickness.^[62] The critical thickness is where the elastic energy is equal to misfit dislocations formation energy. In the mechanical equilibrium model, the total energy is minimized at the critical thickness.^[63] Eom and coworkers used these two models to estimate the critical thickness of SrRuO_3 and BaTiO_3 films on DyScO_3 and GdScO_3 substrates, respectively. The energy balance model shows that h_c of this system with a 2% mismatch is about 20 nm, and that is about 100 nm for this system with 1% mismatch, as shown in Figure 3d.^[64]

It is always energetically favorable for the strained system to relax the elastic energy induced by epitaxial strain. Many other mechanisms could be responsible for strain relaxation besides misfit dislocations formation. For example, composition change was found to partially relax the strain in SiGe layers in semiconductor films.^[65] In addition, oxygen octahedral rotation/tilt,^[66] oxygen vacancy formation and ordering^[67, 68] and structural phase transition^[69, 70] have been attributed to the strain

relaxation in oxide heterostructures. Interestingly, BiFeO₃ (BFO) and LSMO films with low symmetry like rhombohedral and monoclinic structures tend to form twin domains and twin tilt for strain relaxation when grown on STO substrate.^[66, 71-75] Antiphase boundary formation is also observed as a strain relaxation approach.^[76]

The lattice mismatch f provides the source to the intrinsic lattice strain, which develops during nucleation and growth. The in-plane thermal expansion coefficient (α) mismatch between the film and the substrate could induce a thermal stress during cool down process. For example, in the case of InN ($\alpha = 3.6 \times 10^{-6}/\text{K}$) films grown on sapphire ($\alpha = 7.5 \times 10^{-6}/\text{K}$), the biaxial in-plane strain induced from the mismatch of the thermal expansion coefficient is expected to be compressive with a value of 0.27%.^[77] Interestingly, thermal expansion mismatch has been proposed to enable strain tuning. Janolin *et al.* grew Ba_{0.8}Sr_{0.2}TiO₃ thin films on MgO substrates and achieved continuous strain tuning depending on film thickness and growth temperature.^[78] Conventional strain engineering requires coherent interface to deliver the epitaxial strain, while strain engineering via the difference in thermal expansion coefficients requires incommensurate interfaces to generate the strain. This type of strain can be controlled via the density of dislocations by varying the film thickness. Recently, Zhang *et al.* investigated the thermal strain engineering in STO/Si heterostructures and achieved tunable strain ranging from 0.42% to 0.62% for films grown at 600 ~ 800 °C.^[79]

Epitaxial strain plays an important role in ferromagnetic perovskite oxide films. Epitaxial strain affects Jahn-Teller distortion, which results in rotation and elongation of the oxygen octahedron (BO₆). Since the electronic structure of ferromagnetic perovskite oxide films are determined by the octahedral, strain could significantly tune the physical properties. For instance, magnetic anisotropy,^[80] magnetic domain structure^[81] and magnetization/magnetotransport^[82-85] of perovskite manganite thin films can be manipulated by epitaxial strain. In ferroelectric films, epitaxial strain is often used to enhance the polarization and the Curie temperature in BiFeO₃ and BaTiO₃. Epitaxial strain has also been used to produce polarization in SrTiO₃.^[39, 40, 86-94]

3 Vertical Strain Engineering

3.1 Elastic and Inelastic Origin

The epitaxial strain induced by single-crystal substrates has been demonstrated to be a fascinating way to tune and manipulate physical properties of materials. As demonstrated in Figure 3, the strain

relaxes above h_c which is usually between a few nanometers to a few tens of nanometers, depending on the degree of lattice mismatch. Thus, tuning physical properties by uniform epitaxial strain in thick films is difficult. The heteroepitaxial VANs provide several advantages: (1) vertical interfacial strain in thick films, (2) large vertical interface area, (3) tunable microstructure and (4) controllable defects at vertical interfaces.

In VANs, strain exists at both lateral and vertical interfaces. When the film is several times thicker than the feature size of the nanopillars, vertical strain dominates. In lateral heterostructures, strain is limited to heterointerfaces. VANs, on the other hand, have distributed vertical interfaces that allow for strain to be controlled throughout the film thickness.^[30] Tuning functional properties by the vertical strain has been achieved in thick films.^[95, 96] Therefore, vertical strain overcomes the limitation of critical thickness in lateral heterostructures.

MacManus-Driscoll and coworkers discussed the origin of the vertical lattice strain in VANs via DME along the vertical interfaces.^[30] It shows that the strain in VANs is dominated by the vertical interfaces rather than the film/substrate interfaces in relatively thick films. Taken $\text{La}_{0.7}\text{Sr}_{0.3}\text{MnO}_3:\text{ZnO}$ (LSMO:ZnO) on STO (001) as an example, the LSMO phase is in tension out-of-plane. In a pure LSMO film on STO, the LSMO phase is in compression out-of-plane due to the biaxial tensile strain imposed by STO substrate. It was found that 6 ZnO (110) planes ($6 \times 3.24 \text{ \AA} = 19.44 \text{ \AA}$) matches with 5 LSMO (001) planes ($5 \times 3.87 \text{ \AA} = 19.35 \text{ \AA}$), which induces a tensile strain in the LSMO phase.^[97] BiFeO_3 (BFO) is in tension (marked T) out-of-plane and Sm_2O_3 is in compression (marked C) out-of-plane when they are grown individually on STO, as shown in **Figure 4a**. In BFO: Sm_2O_3 VANs, the BFO phase switches from T to C while the Sm_2O_3 phase switches from C to T along the out-of-plane.^[30] Bi *et al.* discussed in details regarding the vertical strain tuning between BFO and Sm_2O_3 phases along the vertical direction.^[98] The strain in VANs could be controlled by vertical interface rather than lateral interface in heterostructures. Such effect changed the orientation of SrRuO_3 phase from [111] to [011] in $\text{SrRuO}_3:\text{ZnO}/\text{STO}$ (111) VANs by increasing the film thickness.^[99] The vertical strain stems from the elastic coupling of the vertical interfaces between the two phases.

The lattice parameter of VANs before and after removing one phase provides a direct evidence of the origin of the lattice strain. Dix *et al.* reported the growth of BFO:CFO VANs in which BFO films consist of strained and relaxed regions while CFO nanopillars are fully strained.^[100] After a selective etching of BFO film matrix, the lattice parameter of CFO is unchanged. It is possible that etching off BFO film is not fully completed and strained BFO region (close to CFO) remained after etching. Wang *et al.* annealed BFO:CFO VANs at 900 °C in air to evaporate Bi and etched off the iron oxides

with dilute acid.^[101] Out-of-plane easy axis in CFO nanopillars disappears after removing the BFO film matrix. A direct evidence of vertical strain relaxation after removing the secondary phase is observed in STO:MgO VANs. In a STO:MgO VAN film grown on STO (001) at 800 °C, the out-of-plane lattice parameter of the STO phase is 3.928 Å (+0.59%) due to the vertical interface strain between STO and MgO (black curve in Figure 4b). After etching off the MgO nanopillars, the STO film peak relaxes to 3.911 Å (red curve in Figure 4b). A relaxation of the out-of-plane lattice parameter of STO phase after removing MgO nanopillars demonstrates that vertical strain is elastic along the vertical interfaces. It should be noted that the STO lattice parameter after etching off the pillars is still slightly higher than the bulk value. This effect can be attributed to the cation non-stoichiometry, which strongly depends on the growth condition.^[102] Elastic strain can modify the lattice parameters, but the change of lattice parameters may not be totally from the elastic deformation. In perovskite oxides, it is common that both cation and anion off-stoichiometry can modify the unit cell volume and lattice parameters.^[103, 104]

3.2 Vertical Strain Distribution

The vertical lattice strain state is directly related to nanopillar size, density and spacing which can be controlled by phase composition^[105] and growth temperature.^[106] For example, the out-of-plane lattice parameter as well as the magnetic/transport properties of the LCMO matrix in LCMO:MgO nanocomposites can be modified by changing the MgO composition.^[105] Via changing the growth temperature, the strain and the magnetic anisotropy of CFO pillars in BTO:CFO VANs can be tuned.^[106] Two key questions are: what are the major factors that control the vertical lattice strain and how to control the vertical strain effectively?

For each pillar in a VAN system, stress can be aligned along two axes: radial and axial. By analytically analyzing the elastic energy in VAN pillars, Schuler *et. al.*^[107] found that the elastic energy density of a pillar is reduced by a factor of 2 when the axial strain is eliminated and by a factor of 5.4 when the radial strain is eliminated. Thus, it is energetically favorable for radial strain to be relieved first. In metal:oxide VANs, well-defined Ni nanopillars with a diameter of 3.4 nm were embedded in a dielectric matrix such as STO and CeO₂, as shown in **Figure 5a-5c**. A radial strain of 0.03% and an axial strain of 1.55% were reported throughout the length of the nanopillars. The axial strain is determined by the minimization of interface and elastic energies. Interface energy scales linearly with pillar diameter (d), and is zero when the axial strain is equal to the strain generated by the lattice misfit. On the other hand, elastic energy scales with d^2 , and is minimized when the axial strain is zero. This indicates that the equilibrium value of axial strain scales at d^{-1} , as shown in Figure 5d.^[107] This is consistent with Chen's results that strain is proportional to the total surface area (S) of nanopillars. In a nanocomposite with uniform nanopillars embedded in the film matrix, $V = m \times \pi d^2 \times$

h ; where V is the total volume of nanopillar phase, m is the number of nanopillars and h is the film thickness or pillar height. It can be found that $S = m \times 2\pi d \times h = 2\pi d \times V/(\pi d^2) = 2V/d$.^[95] In the case of fixed nanopillar volume with different pillar diameter, S is proportional to d^{-1} . Strain scaled with d^{-1} indicates that it is proportional to S . In the case of nanocomposites with fixed nanopillar size but different volume, both V and strain are linearly proportional to S . It should be noted that the linear relationship between strain and S is only valid when nanopillar density is low. The linear increase of strain in the $\text{YBa}_2\text{Cu}_3\text{O}_{7-\delta}$ (YBCO) phase was reported in YBCO: BaSnO_3 ($V < 20\%$) and YBCO: BaZrO_3 ($V < 16\%$) nanocomposites.^[108-110] In LSMO:MgO, the linear relationship between strain and volume of MgO exists when $V < 20\%$. This deviates from the linear relationship at higher MgO volume which indicates other factors come into play.^[95] Another key factor is the misfit dislocation density ρ at vertical interfaces. The misfit dislocation density, $\rho = \frac{2(a_1 - a_2)}{(a_1 \times a_2)}$, where a_1 and a_2 are the lattice parameters of two grown phases at room temperature, is directly related to d and V . When increasing the secondary phase volume or pillar diameter, the difference between a_1 and a_2 increases. This will result in an increase of misfit dislocation density. As discussed by Artemev *et al.*, the degree of vertical interface coherency depends on the size of the nanopillars. This effect is similar to the thickness dependence misfit dislocations formation at film/substrate interfaces.^[111] The density of interfacial dislocations increases nonlinearly with the nanopillar volume fraction, which induces a nonlinear dependence of strain on volume fraction. It should be noted that a linear relationship between strain and nanopillar volume fraction indicates that the ρ is constant when V is low, as observed in YBCO: BaSnO_3 .^[108] However, the dislocation density is expected to increase in nanocomposites where the volume of secondary phase is high or the pillar size is large.

Strain distribution in nanopillars and film matrix is an interesting but less studied subject. For simplicity, most of the literature assumed a uniform distribution of vertical strain along the radical direction. However, the strain distribution strongly depends on the nanopillar density and spacing. In a VAN with vertical pillars of nanometers in size embedded in a film matrix, a critical feature size (d_c) of nanopillars and a critical length of film matrix along the radical direction could exist. For simplicity, the d_c along the radical direction in a VAN is considered as the same as the critical thickness of an epitaxial film. In the mechanical equilibrium model,^[63]

$$d_c = \frac{b}{2\pi f} \frac{(1-\nu \cos^2 \alpha)}{(1+\nu) \cos \theta} \left(\ln \frac{d_c}{b} + 1 \right) \quad (7)$$

where ν is Poisson ratio, b is the magnitude of the Burgers vector, f is the lattice mismatch of these two grown phases in the VAN, α is the angle between the dislocation line and its Burgers vector and θ is the angle between the slip direction and the Burgers vector. In the BTO:CFO VANs, with $f = 3.8\%$, $\nu = 0.26$, $b = 4.195 \text{ \AA}$, $\alpha = \pi/2$ and $\theta = 0$, the d_c is about 48 \AA in CFO nanopillars. Such a strain relaxation induces an interesting core/shell magnetic structure in the CFO phase.^[112] The existence of

both strained and relaxed region in the BFO film matrix in BFO:CFO VANs suggests strain relaxation along the axial direction.^[100] This is reasonable since BFO:CFO VANs always exhibit large pillar size in the range of 50-100 nm.

3.3 Vertical Strain Design Principles

In VANs, two possible lattice matchings (direct lattice matching or domain lattice matching) exist along the vertical interface. For direct lattice matching of strained lattices, m lattices of phase A match with km lattices of phase B (m and k are positive integer numbers). For domain matching, m lattices of phase A match with $m+1$ lattices of phase B. Table 1 summarizes the lattice mismatch and experimental strain for direct lattice matching. The calculated lattice mismatch ranges from 2.3% to 8.7%, while the experimental strain ranges from 1.0% to 2.2%. Therefore, direct lattice matching can produce large strain in VANs if the right components are selected. Table 2 summarizes the domain matching scenario. The lattice mismatch after domain matching is often quite small. For instance, a vertical strain of 0.5% in LSMO was reported in LSMO:ZnO VANs.^[113] In some cases, domain matching can also provide decent strain effect, as reported in BFO:Sm₂O₃.^[30] The direct lattice matching requires a misfit strain less than ~7% in lateral heterostructures.^[33] Interestingly, VANs can tolerate higher lattice mismatch (~9%) for the direct lattice matching. This difference is mainly because both phases in VANs are in nanoscale while heteroepitaxial layer can be completely strained to the substrate. Therefore, a large strain can be designed by carefully considering the epitaxial framework, lattice parameters, elastic constants and thermal expansion coefficients.^[95, 114] For a specific system, the ultimate strain depends on the coherent interfacial area between these two phases,^[95] and the interface coherency can be directly controlled by growth dynamics (nanopillar size, density and spacing) and volume fraction.

Author

Table 1. Summary of vertical lattice strain reported in different materials systems with *direct lattice matching*. The data taken with permission from [95]. Copyright 2016, American Association for the Advancement of Science.

System	a_{bulk} (Å)	k	$ f $	$ \epsilon_{zz} $	Ref
LSMO:MgO	3.87 : 4.21	1	8.41%	2.0%	[95]
LCMO:MgO	3.86 : 4.21	1	8.67%	2.1%	[105]
BFO:CFO	3.96 : 8.39	2	5.76%	1.0%	[115]
BTO:CFO	4.04 : 8.39	2	3.76%	1.6%	[106]
BFO:LSMO	3.96 : 3.87	1	2.29%	1.3%	[116]
BZO:YBCO	11.679 : 4.193	3	7.70%	1.0%	[117]

Table 2. Summary of vertical lattice strain reported in different materials systems with *domain matching*. The data taken with permission from [95]. Copyright 2016, American Association for the Advancement of Science.

System*	a_{bulk} (Å)	m	$m:m+1$	$ f $	$ \epsilon_{zz} $	Ref
LSMO (001): ZnO (110)	3.87 : 3.24	5.14	5:6	0.46%	~0.5%, & 1.0%	[30, 97]
LSMO (111): ZnO (0001)	6.70:5.21	3.50	3:4+4:5	$8.5 \times 10^{-3}\%$	0	[118, 119]
CeO ₂ :LSMO	5.41 : 3.87	2.51	2:3+3:4	0.13%	<0.1%	[120]
CeO ₂ :Ni	5.41 : 3.52	1.94	2:3	2.4%	0.9%	[107]
SrZrO ₃ :Gd ₂ O ₃ [†]	4.09 : 2.70	1.94	2:3	0.98%	0.9%	[121]
BTO:Sm ₂ O ₃	4.04 : 2.73	2.08	2:3	1.17%	2.35%	[122]
BFO:Sm ₂ O ₃	3.96 : 2.73	2.22	2:3+2:3+3:4	1.71%	~1.4%	[30]
STO:Sm ₂ O ₃	3.905 : 2.73	2.32	2:3+2:3+3:4	0.31%	--	[123]

* The calculated m value is 2.51 for CeO₂:LSMO, therefore, m can be valued as 2 or 3. Therefore, both 2:3 and 3:4 matchings exist and align alternatively (50%:50%). In the STO:Sm₂O₃ system, m is 2.32. m can be either 2 or 3. Both 2:3 and 3:4 matchings exist with a frequency of 66% 2:3 and 34% 3:4. In the SrZrO₃:Gd₂O₃ system, the calculated m is 1.94, therefore, the m is set to 2 for domain matching.

[†] Bulk lattice constant of Gd₂O₃ is 10.80 Å. The plane spacing for Gd₂O₃ (004) is 10.80 Å/4 = 2.7 Å.

4 Strain, Defect and Microstructure Correlation

4.1 Microstructures via Competition of Strain and Interfacial Energies

The nanocomposite design and growth have been discussed in previous review articles.^[124-127] MacManus-Driscoll *et al.* discussed in details about the growth mechanisms of two-phase nanocomposites, including nucleation and growth, spinodal decomposition and pseudospinodal decomposition.^[124] The growth mechanisms largely depend on the miscibility of cations in the starting materials.^[128]

The growth of two-phase materials into a nanocomposite has generated a variety of nanostructures with different morphologies. Vertical nanocomposites consist of one phase embedded in a film matrix, where arrays of circular and rectangular nanopillars or laminar precipitation are oriented perpendicular to the substrate surface. Generally, the microstructure of VANs is driven by the minimization of the total free energy, which is related to the elastic and interfacial energies.^[111, 129] The elastic and interfacial energies are related to lattice parameter, surface energy, elastic moduli, volume fraction and film thickness. In fact, both elastic and interfacial interactions are also strongly influenced by thermodynamics and growth kinetics, as shown in **Figure 6**.

Understanding microstructure formation and evolution in nanocomposites has gained extensive attention from theory perspectives. Simulation results show that elastic interactions between these two phases and substrate constraint are critical to microstructure formation and evolution.^[111, 130-132] A three-dimensional phase field microelasticity model predicts that it is necessary to have both modulus and lattice mismatch for the formation of VAN structures. It shows that larger modulus difference in strain energy minimization favors the formation of vertical nanopillars. In addition, the stiffer phase often forms pillars while the softer phase forms matrix.^[132] It should be noted that both modulus and lattice mismatch play key roles for the vertical strain tuning.^[95] In addition, checkerboard formation driven by pseudospinodal decomposition has been experimentally observed in $\text{Zn}(\text{Ga}, \text{Mn})_2\text{O}_4$,^[133] $\text{Mg}(\text{Fe}, \text{Mn})_2\text{O}_4$,^[134] $(\text{Nd}, \text{Li})\text{TiO}_3$,^[135] and Mn doped CoFe_2O_4 .^[136] Simulations show that the checkerboard formation is associated with the symmetry-lifting crystal lattice rearrangement.^[137, 138] (Pseudo)spinodal decomposition favors composition fluctuations, which generates nanoscale phase separation with different lattice parameter, symmetry and chemical composition to minimize total free energy of the system. This phase separation reduces the volume strain energy via the formation of two regions with different compositions, rather than the formation of misfit dislocations.

During thin film synthesis, interfacial interactions could overcome elastic interactions and dominate the microstructure formation. With an in-plane anisotropy strain, labyrinth structure was proposed^[111] and observed in the LSMO:ZnO^[97] and ZrN:AlN^[139] systems. In an isotropic system, the changes of the microstructure with volume fractions is mainly controlled by the total interface energy minimization. When the secondary phase fraction is low, it favors circular nanopillar formation. This has been observed in both metal:oxide and oxide:oxide systems. Circular metal nanopillars in oxide film matrix have been reported in Fe:LaSrFeO₄,^[140] Co:CeO₂,^[141] Co:BaZrO₃,^[142] Ni:CeO₂,^[143] Ni:BaZr_{0.8}Y_{0.2}O₃^[144] and CoNi:(BaSr)TiO₃.^[145]

One of the important aspects in synthesizing VANs is the manipulation of feature size of the nanopillar phase. Zheng *et al.* suggested a diffusion controlled growth mechanism, where the growth temperature (T) and pillar feature size (d) can be fitted to an Arrhenius behavior.^[146] The surface mean diffusion length can be described by $l = \sqrt{4Dt}$ with D as the surface diffusivity and t as the time to grow one unit cell layer. The diffusivity can be expressed as $D = D_0 e^{-E_a/kT}$, where k is Boltzmann's constant, T is the growth temperature, E_a is the activation energy for surface diffusion and D_0 is the surface diffusion constant. If d is approximately assumed to be equal to the diffusion length, then,^[147]

$$\ln(d) = \frac{\ln(4D_0t)}{2} - \frac{E_a}{2kT} \quad (8)$$

It is clear that $\ln(d)$ is inversely proportional to T . The surface diffusion energy was reported to be 1.2 eV for Fe:LaSrFeO₄,^[140] 0.18 eV for Ni:BaZr_{0.8}Y_{0.2}O₃,^[144] and 1.56-1.66 eV for BFO:CFO and BTO:CFO.^[147] The Arrhenius-like dependence of d in VANs indicates that nanopillar formation takes place at the growth temperature. The pillar size d is the competing result between strain and interfacial energies, driven by thermodynamics and growth kinetics. In an elastic energy model of strain lattice, Shi *et al.* calculated the nanorod diameter in YBCO films by minimizing the energy of nanorods formation, the elastic energy of the matrix and nanorods, and the interfacial energy on the nanorod surface.^[148] Simulation shows that d is related to the decay of lattice strain inside the nanopillars and the elastic constant of the nanopillars. The spacing between these nanopillars can be also estimated based on the surface diffusion length. It was found that E_a is 1.66 eV and D_0 is $1.34 \pm 0.91 \times 10^{10}$ nm²/sec for the CFO phase in BFO:CFO VANs, which gives a diffusion length of 55 ± 26 nm.^[149]

Thermodynamics and growth kinetics play critical roles in elastic and interfacial interactions. For example, elastic and interfacial energies strongly rely on the secondary phase size which is directly controlled by thermodynamics and growth kinetics. As shown in Figure 6b-6d, the shape of Fe nanopillars in the LaSrFeO₄ film changes from a square (Figure 6b) to an octagonal (Figure 6c), and then to a circular shape (Figure 6d) with decreasing growth temperatures.^[140] The microstructure is a result of total free energy minimization. Cylindrical pillars with small diameters minimize the surface energy while faceted (e.g., cube or pyramidal shape) pillars minimize the elastic strain energy. When the growth temperature is low, diffusion is limited and the feature size is small. The surface energy dominates; this favors a circular shape nanopillars. Higher growth temperatures increases feature size. Therefore, the strain energy over surface energy is significantly increases. In the BTO:CFO system, the CFO nanopillar shape was reported to be both rectangular^[150] (Figure 6e) and circular^[146] (Figure 6f) in films with similar molar ratio and growth temperature. Such a shape variation could be related to the laser energy density difference. For instance, we found out that the shape of CFO changes from cylindrical to pyramidal with increasing laser energy density from 1.5 J/cm² to 2.5 J/cm² (not shown here) for BTO:CFO (mol: 35%) VANs grown at 850 °C. The shape evolution of CFO nanopillars with laser energy could be similar to the temperature dependent shape change in Fe nanopillars since higher laser energy density increases the kinetic energy of adatoms and improves the diffusion length. In BFO:CFO VANs, the CFO phase typically exhibits a rectangle shape (grown at 650 °C). The high diffusivity of BFO due to its low melting point results in a larger pillar size (50-100 nm). Such a large feature size favors the formation of pyramidal CFO nanopillars as the elastic strain energy dominates over surface energy. Therefore, the microstructure can be controlled by the thermodynamics and growth kinetics via interfacial and elastic interactions.

Different from nucleation and growth, phase separation driven by decomposition often forms nanocomposites with thermodynamically and/or kinetically more stable phases. Ross and coworkers reported the growth of an interesting three-phase VAN with Cu nanopillars ($d = 3$ nm) in cubic SrO shell embedded in a matrix of Sr(Ti, Cu)O_{3-δ} films.^[151] Chemical etching using ammonium hydroxide removed 3 nm diameter Cu nanopillars leaving porous SrO pillars in film matrix, as shown in **Figure 7(a)**. Under a vacuum growth condition, SrTi_{0.75}Cu_{0.25}O_{3-δ} can decompose into Cu + SrO + Sr(Ti, Cu)O_{3-δ}. Starting from La_{0.5}Sr_{0.5}FeO₃, Fe nanopillars and LaSrFeO₄ film matrix can be formed via decomposition under vacuum.^[140, 152-154] A very recent work shows the formation of Ir nanopillars in SrTiO_{3-δ} matrix.^[155] The starting SrTi_{1-x}Ir_xO₃ tends to decompose into Ir + SrO + SrTiO_{3-δ} at growth conditions with low oxygen partial pressures.

During self-assembled growth, vertical nanopillars are randomly distributed in the film matrix. The spacing of these nanopillars are governed by the diffusion length. Templates fabricated by e-beam lithography and focused ion beam/etching provide nucleation and growth sites for nanopillars which enable the fabrication of magnetic nanopillar arrays with controlled periodicity. Comes *et al.* reported the fabrication of square CFO nanopillars arrays in BFO films, which was achieved by the patterning of CFO films into nanopillars arrays via lithography, followed by the growth of a BFO layer.^[149] Ross and coworkers reported the growth of square magnetic nanopillar arrays in BFO films via a selective growth of the magnetic CFO phase.^[156] In this process, dots and lines with controlled spacing and diameter were first written on substrates by a focused ion beam. Ordered arrays of pits and trenches were formed after selectively etching away the ion-damaged regions. A thin seed layer of CFO was then grown with a low growth rate followed by post-annealing to promote the formation of CFO nanoislands on the ordered defect sites. These CFO nanoislands provide the sites for the directed growth of subsequent CFO nanopillars. Figure 7b shows a plan-view SEM image of $\text{Co}_{0.5}\text{Ni}_{0.5}\text{Fe}_2\text{O}_4$ square nanopillars embedded in BFO matrix fabricated by this method. Using a nucleation-induced self-assembly growth, Stratulat *et al.* reported ordered CFO nanopillars embedded in a BFO matrix.^[157] Taking advantages of anodic aluminum oxide and lithography, the CFO nucleation centers were synthesized before the growth of VANs. Well-defined rectangle CFO nanopillars with pyramids in the BFO matrix were achieved as shown in Figure 7c and 7d, which is consistent with the self-assembly growth. Except these top-down approaches, a bottom up approach was reported recently. By using a simple thermal annealing, parallel SrO and TiO_2 termination stripes can be formed alternatively on STO substrate. Wang and coworkers have achieved the selective growth of LSMO: CeO_2 VANs on SrO terminated STO substrates.^[158]

4.2 Elastic Interactions Driven Defects Formation

4.2.1 Defects Modulation

In lateral heterostructures, misfit dislocations form at the critical thickness. This rule also applies to vertical nanostructures. **Figures 8a** and **8b** show a cross section high angle annular dark field (HAADF)-STEM image and the corresponding fast Fourier transform (FFT) image of a LSMO:MgO VAN grown on a STO (001) substrate. In the axial direction, a misfit dislocation, parallel to MgO nanopillar, is formed in nanopillar at about 19 unit cells to the STO substrate. This is very different from the formation of misfit dislocations right at the MgO/STO interfaces when MgO film is directly grown on STO substrate. The MgO nanopillar with a feature size of 4-5 nm allows the strain energy

relaxation at much larger thickness. In the radial direction, misfit dislocations form at nanopillar/matrix interfaces when pillar feature size (d) reaches a critical value. Figure 8c shows a plan-view HAADF-STEM image of a LSMO:ZrO₂ VAN film with ZrO₂ nanopillars in LSMO matrix. The FFT image (Figure 8d) shows the formation of misfit dislocations at the vertical heterointerfaces. The critical feature size d_c for misfit dislocation formation is rarely explored in VANs. Interestingly, as shown in Figure 8c, two ZrO₂ nanopillars are connected by one dark line. Zhou *et al.* argued that these lines are antiphase phase boundaries (APBs).^[159] Electron energy loss spectroscopy (EELS) shows these APBs is Mn rich (Figure 8e-8h), which is consistent with the lower contrast in the STEM images. Dislocations symmetrically formed on the circumference of pillars help to relax the radial strain.^[160, 161] It is noted that nanopillars connected by APBs show unpaired dislocations, as shown in Figure 8d. Interestingly, the Burgers vector of the missing misfit dislocation is parallel to a component of the APB translation vector. This indicates that the APB formation assists strain relaxation. In addition, APBs are only observed between two pillars with a short spacing as the APB energy increases with distance. In the lateral heterostructures, the formation of APBs in the highly epitaxial oxide thin films is often related to film/substrate lattice mismatch, substrate surface-step-terrace dimension and miscut angle.^[162-164] In VANs, except these factors, the elastic strain at the vertical interface plays an important role for the APB formation. APB is one of the most common defects in VANs to accommodate the large vertical lattice mismatch. This has been observed in many different materials systems including LaNiO₃:NiO^[165] and others we have grown (e.g., BTO:CFO, STO:Sm₂O₃, and LSMO:MgO).

4.2.2 Microstructure Modulation

As discussed above, microstructure is often entangled with strain. Experimental results have shown that microstructure modulation is one of the most common mechanisms for strain relaxation. For instance, double perovskite Bi₂FeMnO₆ films can be grown on STO substrates, while a bismuth-based supercell structure with a highly strain interfacial layer can be grown on LaAlO₃ (LAO) substrates. Interestingly, the bismuth-based self-assembled supercell structure can be enabled on a CeO₂ layer buffered STO.^[45, 69, 70, 166, 167] The interfacial structural modulation is also observed during the growth of Bi₂AlMnO₆ on STO (001)^[168] and La_{2/3}Sr_{1/3}MnO₃ on LaSrAlO₄ (001).^[169] In the strained ZnMnGaO₄ films, spinodal decomposition induces the formation of two nanorod materials which are chemically different and spatially ordered with coherent interfaces. Such a unique microstructure relieves the volume strain energy and suppresses misfit dislocations formation.^[133] In addition, the formation of twin tilt, rather than misfit dislocations, in oxide films with low symmetry has been observed in lightly doped LaMnO₃ and BiFeO₃ thin films on STO substrates.^[74, 75]

One of the interesting microstructure modulations in VANs has been reported in the YBCO:BZO system. With increasing the BZO volume ratio, the system evolves from a vertical structure of BZO nanopillars embedded in YBCO film matrix to a lateral multilayer structure of YBCO/BZO.^[170] The microstructure transition, together with a significant relaxation of out-of-plane strain in the YBCO phase and an increase of critical temperature,^[171] indicates that the microstructure transition is mainly driven by the relaxation of strain energy.^[117] In addition, to accommodate the large lattice mismatch and elastic modulus mismatch, secondary phase such as BZO and BSO pillars in YBCO films tend to grow tilted away from the perfect zone axis. In LSMO:MgO and BFO:CFO VANs, the formation of a few of unit cells of LSMO and BFO on STO have been observed before the growth of MgO and CFO phases, respectively. Possible reasons for the LSMO or BFO layer formation at the very early stage of film deposition could come from the smaller lattice mismatch, similar crystal structure and symmetry. In the STO:MgO VANs, we have found the formation of TiO_x phase in MgO nanopillars when the MgO nanopillar size exceeds 10 nm (not shown here). The larger MgO nanopillars impose significant strain energy in the nanocomposite since the lattice mismatch between the MgO and the STO is 7.8%. The strain energy can be reduced by the formation of TiO_x/MgO core-shell structure, producing a similar effect as by reducing the MgO nanopillar feature size. The formation of a three-phase VAN with Cu nanopillars in cubic SrO shell embedded in a matrix of Sr(Ti, Cu)O_{3-δ} films could be driven by the same mechanism (Figure 7a).^[151] The formation of cubic SrO nanopillars ($d = \sim 9$ nm) indicates the large elastic strain energy between the SrO and the Sr(Ti, Cu)O_{3-δ}. The Cu cores formed in the SrO cubic nanopillars could relax the elastic strain energy and total free energy.

4.2.3 Cation Stoichiometry Modulation

In lateral heterostructures, stoichiometry modulation can be induced by strain and symmetry mismatch.^[34, 65, 172] A structurally and electronically modified transition layer was formed between VO₂ and sapphire or TiO₂ and sapphire heterostructures.^[34, 172] The formation of a transition layer is driven by the interfacial free energy minimization to accommodate the symmetry mismatch between the substrate and the film.

In a LSMO:NiO VAN system, plan-view HAADF STEM image shows 3-5 nm NiO nanopillars are randomly embedded in the LSMO film matrix, as shown in **Figure 9**.^[173] Interestingly, ring-shape white contrast is seen around the NiO nanopillars (Figure 9a). The higher Z contrast indicates possible La excess around NiO nanopillars. The energy dispersive X-ray spectroscopy (EDS) color mapping of the same region confirms that La and Mn compositions near the NiO nanopillars are higher than that at regions far away from nanopillars (Figure 10b-10d).^[174] La and Mn rich compositions with La>Mn strongly indicates the formation of La_{1+δ}MnO₃ ($\delta > 0$) phase. The cation excess could be expressed as

the formation of oxygen vacancies ($\text{LaMn}_{1/(1+\delta)}\text{O}_{3/(1+\delta)}$). Considering the Ni^{2+} substitution of Mn^{3+} , charge balance requires the formation of oxygen vacancy. For most perovskite oxides, the out-of-plane lattice parameter is sensitive to oxygen deficiency and cation off-stoichiometry.^[104, 175-177] The formation of an interfacial layer (oxide deficient LaMnO_{3-x} phase), probably driven by the spinodal decomposition, could create composition change to reduce lattice mismatch (as large as 8.7%) and strain energy. This is consistent with the STEM-EELS study in a $\text{LSMO}:\text{ZrO}_2$ VAN (mismatch 5.3%~7.5%).^[160] Enhanced La and Mn concentrations and reduced Sr concentration were observed at the vertical nanopillar-matrix interface. EELS shows that the Mn valence state drops from the matrix to the pillar. Charge balance requires the formation of oxygen vacancies at the vertical interface. Overall, the interface composition resembles LaMnO_{3-x} with an oxygen vacancy concentration of 8%. Along with the formation of oxygen vacancy, the substitution of Zr^{4+} (0.72 Å) to Mn^{4+} (0.53 Å) site increases the lattice parameter of LSMO, both of which reduce the lattice mismatch at the nanopillar/matrix interface.

4.2.4 Oxygen Vacancies Modulation

Oxygen vacancy is one of the most common defects in oxide thin films. Oxygen vacancy formation and ordering have been discussed in lateral heterostructures to accommodate the strain relaxation^[67, 178] and compensate for the chemical potential mismatch.^[179] Three main approaches have been mostly used to accommodate oxygen vacancies: (I) by generating corresponding vacancies in cation sites; (II) by altering the valence state of cations without altering cation stoichiometry and (III) by incorporating both cation vacancies and change of valence state. During the growth of metal oxides without cation multiple valence states such as SrTiO_3 or BaTiO_3 , oxygen vacancy formation can be driven by the cation vacancy formation which is strongly tied to thermodynamics and growth kinetics. Charge balance requires the formation of cation-anion vacancy pairs. In oxides with multiple cation valence states, oxygen vacancies are often compensated by the change of cation valence states. Perovskite oxides with transition metals such as V, Co, Fe, and Mn belong to this category. For instance, Lee and coworkers reported reversible temperature controlled oxygen vacancy formation in strontium cobaltite. They found that tensile strain significantly decreases the oxygen vacancy activation energy and thus enhances the cobaltite's catalytic activity.^[180-182] More recently, Yu and coworker reported controllable and reversible oxygen stoichiometry modulation in strontium cobaltite via an ion liquid gating.^[183, 184] Such a method also allows tuning of the electronic and magnetic properties by varying the oxygen content. For instance, ion liquid gating has been used to tune the functional properties via controlling oxygen ion migration in a variety of oxide thin films.^[185-190] Both the formation of cation vacancies and the change of the valence state have been observed in bulk and thin film LaMnO_3 .^[191-194]

In VANs, the formation of oxygen vacancies has been observed and discussed in RE-Ba₂Cu₃O_{7-δ} (RE: rare earth Y or mixture of Y and rare earth):BZO and STO:Sm₂O₃. **Figure 10a** shows EELS intensity profiles of Y, O, and Ba across a BZO nanopillar in a REBCO matrix. The oxygen profile (red curve) shows a clear dip outside of the BZO pillars. The oxygen depletion region close to BZO nanopillars is clearly seen in the EELS mapping, as shown in Figure 10b. In addition, the strain distribution near the REBCO/BZO vertical interface, extracted from the STEM image, shows that the strain first increases and then decreases near the BZO nanopillars. In addition to the interface dislocations, oxygen deficiency near the vertical interfaces can also relax the strain. The formation of oxygen vacancies have been attributed to the strain relaxation and T_C suppression in REBCO materials.^[109] The formation of oxygen vacancies across the vertical interface is also discussed in STO:Sm₂O₃ VANs. The strain induced defect formation can significantly modify the physical properties as discussed in the later sections of this article.

5 Functionality Tuning Driven by Strain, Defect and Interface

Vertical heteroepitaxial nanocomposites exhibit several unique characteristics which allow an unprecedented control of functionality.

- 1) The vertical strain exists in both phases and goes beyond conventional critical thickness. Functional properties can be significantly manipulated by the vertical strain.
- 2) Unique microstructure such as nanopillars and rectangle nanodomains embedded in a film matrix can be controlled to a certain degree. Such microstructure favors a large amount of vertical heterointerfaces which could improve interfacial effects such as interface couplings.
- 3) Defects such as oxygen vacancies close to the vertical interfaces can be used to control functionalities. The formation of oxygen vacancy, which strongly ties to cation stoichiometry, can be induced by vertical strain.

5.1 Ferromagnetism and Ferroelectricity

5.1.1 Strain and Microstructure Controlled Magnetic Anisotropy

Data storage applications such as perpendicular recording and magnetoresistive random access memory have made magnetic materials with strong perpendicular magnetic anisotropy an active research field for decades.^[195] In thin films, the magnetic anisotropy is determined by the competition

of magnetocrystalline anisotropy, shape anisotropy, strain anisotropy, and interface exchange anisotropy. The epitaxial strain induced magnetoelastic anisotropy energy is given by,^[196]

$$K_{me} = 3\lambda\sigma/2 \quad (9)$$

λ is the magnetostriction coefficient of the magnetic phase. Stress can be expressed as $\sigma = \epsilon Y$, (where Y is the Young's modulus that can be written in terms of the elastic moduli C_{11} and C_{12} . ϵ is the epitaxial strain). In a cubic or pseudo-cubic structure, Young's modulus can be expressed as $Y = \frac{(C_{11}-C_{12})(C_{11}+2C_{12})}{C_{11}+C_{12}} = C_{11} - 2\nu C_{12}$ by considering Eq. 6. In a VAN structure, the magnetoelastic anisotropy of magnetic nanopillars along the film growth direction is given by,

$$K_{me} = 3\lambda\epsilon_{zz}(C_{11} - 2\nu C_{12})/2 \quad (10)$$

ϵ_{zz} is the out-of-plane strain in magnetic nanopillars. In-plane strain is ignored in nanopillars as lateral interactions between nanopillars and substrate is very weak.

In a VAN structure, the magnetoelastic anisotropy of magnetic film matrix along film growth direction is given by,

$$K_{me} = 3\lambda(\epsilon_{zz} - \epsilon_{xx})(C_{11} - 2\nu C_{12})/2 \quad (11)$$

ϵ_{zz} and ϵ_{xx} are the out-of-plane and in-plane strain for the film matrix.

Shape anisotropy has important contributions in needle-like nanopillars and thin films with a large aspect ratio. The shape anisotropy is given by,

$$E_{shape} = (N_x - N_z)2\pi M^2 \quad (12)$$

N represents the demagnetization factors along the easy axis, which depends on the aspect ratio. M is the saturated magnetization. For nanopillars with a large aspect ratio, $N_x \approx 0.5$ and $N_z \approx 0$, the anisotropy energy is simplified as πM^2 . For thin films, $N_x \approx 0$ and $N_z \approx 1$, the anisotropy energy is simplified as $-2\pi M^2$. If these nanopillars have magnetic interactions, the shape anisotropy of nanopillars in VAN changes with the volume fraction. It can be estimated as,^[197]

$$E_{shape} = (1 - 3p)\pi M^2 \quad (13)$$

where p is the volume fraction of nanopillars in VAN films. When $p \rightarrow 0$, the anisotropy energy is πM^2 which corresponds to diluted nanopillars in film matrix. When $p \rightarrow 1$, the anisotropy energy is $-2\pi M^2$ which corresponds to a planar magnetic thin film. The shape anisotropy field is then given as $H_{shape} = \frac{2E_{shape}}{M}$.

Taking BTO:CFO VANs with compressive out-of-plane strain in CFO phase as an example, an out-of-plane easy axis was observed in this VAN system, as shown in **Figure 11a**. The shape anisotropy field of CFO nanopillars has been determined to be ~ 2.2 kOe (the green triangle in Figure 11b).^[106] Young's modulus of CFO is ~ 150 GPa. The magnetostriction coefficient of CFO single crystals was reported to be between $-(200\sim 590)\times 10^{-6}$ and the magnetostriction coefficient of epitaxial CFO thin films was estimated to be -188×10^{-6} .^[198] The magnetostriction coefficient of -200×10^{-6} is used in the estimation. For the VAN grown at 900°C with a ε_{zz} of -1.1% , an estimated out-of-plane strain anisotropy field is 44 kOe, which is far larger than the shape anisotropy field. The total magnetic anisotropy (51 kOe) is dominated by the strain effect. Magnetic anisotropy of CFO and NiFe_2O_4 (NFO) based nanocomposites have been widely studied and it is controlled by the compressive vertical strain.^[199-201] The direct growth of BFO:CFO VANs on LAO results in a majority of the BFO tetragonal phase. By inserting a LaNiO_3 buffer layer, the BFO rhombohedral phase was restored as well as the out-of-plane easy axis.^[202] In LSMO magnetite films with positive magnetostriction coefficient, tensile strain favors out-of-plane magnetic anisotropy. The film nature of LSMO favors in-plane anisotropy while the out-of-plane tensile strain favors out-of-plane magnetic anisotropy. It is not surprising that the magnetic anisotropy is determined by the shape effect in relaxed BFO:NFO nanocomposites.^[203] Interface exchange anisotropy across antiferromagnetic-ferromagnetic (AFM-FM) interface has been used to explain the large magnetic anisotropy in the BFO:CFO^[204] and exchange coupling in LSMO:BFO.^[116]

5.1.2 Defects and Microstructure Dominated Magnetotransport

Manganite perovskites with a colossal magnetoresistance (CMR) at large magnetic fields have been extensively studied in the past decades. Polycrystalline samples with large angle grain boundaries (GBs) and composite samples with artificial GBs (secondary phase doping) exhibit low field magnetoresistance (LFMR).^[113, 205, 206] However, epitaxial single-phase manganite thin films show very small LFMR effect. Heteroepitaxial VANs based on manganites have been designed to improve LFMR through tuning the microstructure and strain. It should be noted that the magnetoresistance in these materials is normally negative. Positive MR in perovskite oxides is rarely reported.^[207]

$\text{La}_{0.7}\text{Sr}_{0.3}\text{MnO}_3$ is a FM material that displays CMR in its bulk single-crystals but very weak LFMR in single-crystals and epitaxial thin films. To demonstrate the effect of microstructure on MR, $(\text{La}_{0.7}\text{Sr}_{0.3}\text{MnO}_3)_{1-x}(\text{ZnO})_x$ VANs were synthesized.^[95] Unlike polycrystalline composites, it was found that both $\text{La}_{0.7}\text{Sr}_{0.3}\text{MnO}_3$ and ZnO phases can epitaxially grown on STO (001) substrates. The ZnO phase forms rectangle nanodomains which are perpendicular to each other. This structure has also been reported in LSMO: CeO_2 VANs.^[208] By changing the ZnO phase volume ratio from 0% to 50%, the ZnO nanodomain density increases. The nanodomains start to connect and form ZnO nanomaze. Therefore, $\text{La}_{0.7}\text{Sr}_{0.3}\text{MnO}_3/\text{ZnO}/\text{La}_{0.7}\text{Sr}_{0.3}\text{MnO}_3$ tunneling junctions were potentially formed when the ZnO phase approaches the volume percolation threshold. This explains the significantly enhanced MR with ZnO volume ratio approaching 50%.^[97] The spin-polarized tunneling across the ferromagnetic/insulating/ferromagnetic structure could be responsible for the enhanced LFMR close to the percolation threshold. When the secondary phase is below the percolation threshold, the MR in VANs can be tuned via the domain size, microstructure, defects, interface diffusion and interface exchange coupling.^[173, 208-212]

5.1.3 Strain Dominated Magnetotransport

In complex oxides, substrate induced epitaxial strain is an alternative way to manipulate charge/orbital/spin orders. Particularly, strain has been widely used to modulate MR effect in ultrathin epitaxial manganite films,^[85, 213] as well as in two-dimensional transition metal dichalcogenides.^[214] One of the key limitations of epitaxial strain engineering is that the critical thickness of heterostructures is only a few tens of nanometers. For example, epitaxial strain significantly enhanced MR in thin strained films and MR diminished above 20 nm.^[215] Therefore, it is a challenge to tune magnetism and transport properties by epitaxial strain in relatively thick films. As discussed above, the vertical strain in VANs can exist in thick films which can be used to tune the functionalities. By

doping MgO into $\text{La}_{0.7}\text{Ca}_{0.3}\text{MnO}_3$, Moshnyaga *et al.* reported tunable magnetic properties coupled with a structural transition in composite films synthesized via a metal-organic aerosol deposition technique on MgO (100) substrates.^[105, 216] To investigate the vertical strain effect on magnetization and magnetotransport in thick films, Chen *et al.* synthesized vertically heteroepitaxial nanocomposites with MgO nanopillar arrays embedded in $\text{La}_{0.7}\text{Sr}_{0.3}\text{MnO}_3$ films by PLD method.^[95] **Figure 12a** and the inset show the cross-section and plan-view STEM images of MgO nanopillar arrays in a LSMO film matrix. Strain in this system is analyzed by phase field simulation. It shows that large vertical strain can be generated in both LSMO matrix and MgO nanopillars, which strongly depends on the volume ratio and pillar size (Figure 12b). Figure 12c shows that the strain in the $\text{La}_{0.7}\text{Sr}_{0.3}\text{MnO}_3\text{:MgO}$ VANs is much larger than that in the $\text{La}_{0.7}\text{Sr}_{0.3}\text{MnO}_3\text{:ZnO}$ VANs with the same volume of the secondary phase. Such a large vertical strain in the LSMO:MgO VANs is attributed to the larger lattice mismatch and elastic modulus mismatch. This vertical strain has significantly modified magnetization and magnetotransport properties (Figure 12d). In the LSMO:ZnO system, the jump of resistance occurs at 50% of ZnO volume but the magnetization of LSMO is almost independent of composition. This indicates that the phenomena in this system are mainly attributed to secondary phase induced volume effect. However, in LSMO:MgO system, the rise of resistance as well as the drop of magnetization happen at about 20% of MgO volume which is well below the volume induced percolation threshold, indicating this phenomenon is mainly attributed to the secondary phase induced strain effect. It should be noted that the magnetization in LSMO:MgO dropped over 10 times when the MgO volume increases from 5% (260 emu/cc) to 22% (25 emu/cc). Such a significant drop in magnetization could be related to the strain induced oxygen vacancies in the LSMO phase.^[178, 217]

5.1.4 Strain Enhanced Ferroelectricity

Epitaxial strain is a common tool used to tune the ferroelectricity in heterostructures. For example, Choi *et al.* reported a much enhanced paraelectric-to-ferroelectric transition temperature (T_C) and a saturated polarization (P_s) in compressively strained BTO films on GdScO_3 (110) and DyScO_3 (110) substrates.^[40] The 200 nm BTO films on SrRuO_3 buffered GdScO_3 ($\epsilon_{xx} = -1.0\%$) showed a T_C of 400 °C and P_r of 50 $\mu\text{C}/\text{cm}^2$. The films on DyScO_3 ($\epsilon_{xx} = -1.7\%$) showed a T_C of 540 °C and P_r of 70 $\mu\text{C}/\text{cm}^2$ which are far larger than the bulk values ($T_C = 130$ °C, $P_r = 27$ $\mu\text{C}/\text{cm}^2$).^[40] Such a method has been applied to many complex oxides including STO, PZT and BFO films.^[39] In a review article, Schlom *et al.* focused on the effect of epitaxial strain on the physical properties of ferroelectric thin films and superlattices.^[36] Measured T_C for the strained films shows a shift of hundreds of degrees which agrees with simulation.

Vertical strain in VANs shows the similar effect as discussed above. For example, Harrington, *et al.* synthesized BTO:Sm₂O₃ (50:50 molar ratio) with 10 nm Sm₂O₃ nanopillars in BTO film matrix. The out-of-plane lattice parameter of BTO phase is 4.078 Å. The nanopillars impose a tensile strain of 1.07% in BTO phase, which increases the T_C to over 330 °C.^[96] Khatkhatay *et al.* reported a slightly enhanced T_C of 175 °C and P_s of 37 $\mu\text{C}/\text{cm}^2$ in BTO:CeO₂ VANs on SRO buffered STO substrates. It was found that the out-of-plane and in-plane lattice parameters are 4.06 Å and 3.98 Å, respectively, indicating an out-of-plane tensile strain of 0.6%.^[218] Sangle *et al.* synthesized STO:Sm₂O₃ VANs with high tetragonality (c/a) (up to 1.023) in the STO phase.^[219] Owing to the large out-of-plane tensile strain, a T_C up to 300 °C was observed in STO. Similar enhancement effect was also reported in Sr-doped BTO:Sm₂O₃ VAN films with a vertical strain of 1.29-1.68%.^[220] The secondary phase induces large out-of-plane tensile strain in ferroelectric phase and increases the tetragonality which shifts the paraelectric-to-ferroelectric transition to higher temperatures.

5.2 Superconductivity

Defect engineering to enhance critical current densities (J_C) in high temperature superconductor (HTS) films is one of most studied fields.^[221] It was reported that the incorporation of oxide nanoparticles or nanorods in YBCO films produced high current densities at high magnetic fields.^[5] The self-assembled nanoprecipitates serve as the magnetic-flux pinning centers which can be controlled via growth. Different type of oxides including BaMO₃, ($M = \text{Zr, Sn, Hf, Ir, etc}$) have been incorporated in the YBCO film growth.^[5, 222-224] The effects of these nanoparticles or nanorods on superconductivity are twofold. First, the out-of-plane strain induced by the lattice mismatch between YBCO films and nanoparticles tends to suppress the critical transition temperature. For example, the T_C drops from 92 K in pure YBCO films to 84 K in (YBCO)_{0.6}:(BZO)_{0.4} nanocomposites with an increase of out-of-plane lattice parameter of the YBCO phase.^[117] On the other hand, these nanoprecipitates serve as pinning centers which enhance the critical current densities (J_C) at high field.^[225] Except these large three dimensional (3D) defects, the formation of zero dimensional (0D), one dimensional (1D) and two dimensional (2D) defects, as discussed in the growth section, are correlated to strain relaxation in nanocomposites. In fact, the pinning effect of these defects on J_C relies on the defect type and landscape.

The control of defect morphology and landscape to increase J_C is one of the main focuses of defect pinning engineering in superconducting films.^[226-229] The defect morphology and landscape are strongly influenced by the thermodynamics and growth kinetics as discussed in previous sessions. Four different types of defects are often associated with vortices pinning. 0D point defects such as substitutions, vacancies and impurities, 1D defects such as dislocations and irradiation tracks, 2D

defects such as APBs, twin boundaries, grain boundaries, and stacking faults, and 3D defects such as secondary phase nanoparticles/nanocolumns can all modify the J_C and field performance differently. Interestingly, these pinning defects work most effectively at different temperatures and fields, depending on the size and morphology, as discussed by Feighan and coworkers in a review paper.^[226]

At high temperature region (65-77 K), thermal energy is relatively large and secondary phase nanoprecipitates (3D defects) with only a large volume can provide reasonable pinning force at such a high temperature (Region 1 in **Figure 13**).^[222] The best performance at high temperature range in terms of highest J_C and highest irreversibility fields is achieved in nanocomposites with continuous nanorods of insulating secondary phases aligned along the film growth direction.^[230] At moderately low temperatures (~ 50 K), strong pinning centers (2D and 3D defects) like small precipitates (e.g., nanoparticles), and stacking faults become effective. At lower temperatures (~ 10 K), weak pinning centers such as point defects (0D defects) are active (Region 3 in Figure 13). Therefore, the defect-site volume is one of the most critical parameters to tune the pinning strength. At moderately temperatures (30-65 K), the best microstructure is a mixture of 1D/3D nanorods combined with 3D nanoparticles (Figure 13, Region 2). The enhanced performance is due to a synergic effect of these nanostructures to transfer a vortex between two near nanorods.^[226] Another advances of mixed microstructure is the reduced field angle anisotropy.

As shown in Figure 13, J_C shows strong field angle anisotropy due to the alignment of secondary phase defects. In the VANs with nanorods/nanocolumnar parallel to the film growth direction, J_C is greatly enhanced when the magnetic field is parallel to nanocolumns ($H // c$). Wee *et al.* reported the growth of self-assembled BZO nanodots in NdBCO films.^[231] By alternatively depositing (NdBCO)_{3u.c.}/(BZO)_{0.5u.c.} layers, BZO nanodots are self-assembled in the *ab* plane. J_C is enhanced to 1 MA/cm² with $H // ab$. In addition, BZO nanorods in VANs align along the out-of-plane direction, producing enhanced J_C with $H // c$. Therefore, BZO nanorods arrays were aligned in both vertical and horizontal directions in the NdBCO superconducting films which results in the maximized pinning effect and J_C performance.

5.3 Magnetolectric coupling

Multiferroics with more than one of the primary ferroic properties (e.g. ferromagnetism, ferroelectricity, ferroelasticity) are now often used to describe magnetolectric multiferroics that are simultaneously ferromagnetic and ferroelectric. Since the discovery of BiFeO₃ films with room temperature ferroelectricity and canted ferrimagnetism,^[4] multiferroics have become one of the most

studied materials in complex oxides.^[232] The revival of this field is not only because of the importance of studying the physical origin of multiferroics, but also due to the potential applications. The magnetoelectric (ME) coupling of ferroic orders has been proposed to design novel solid state memory devices with extremely low energy consumption.^[233] Single-phase multiferroic materials are very scarce due to their exclusive nature of origins.^[234, 235] An important way to achieve multiferroicity is by combining individual ferroelectric and ferromagnetic (or ferrimagnetic) materials to form composites. The current research status and future direction of bulk composites, thin film nanocomposites and heterostructures for ME couplings can be found in several comprehensive reviews.^[236-246] This section will mainly focus on the ME couplings in VANs.

Because of large vertical interface and possibly reduced substrate clamping effect in thick VANs, VANs could be more favorable for ME couplings. Zheng *et al.* pioneered the growth of multiferroic BTO:CFO VANs.^[29] A magnetization kink was observed in *M-T* curves close to the BTO phase transition temperature in VANs rather than multilayered CFO/BTO nanostructures, indicating the possible existence of ME couplings in the BTO:CFO system. Nan *et al.* has compared the ME couplings in VANs and multilayer structures by using Green's function approach and confirmed that ME coupling in VANs is larger than multilayers.^[247] Recently, Wu *et al.* simulated the misfit strain effect and ferromagnetic composition effect on the ME coupling in VANs.^[248] He found that the ME voltage coefficients of BTO:CFO nanocomposite films strongly rely on the in-plane and out-of-plane misfit strain. A large ME voltage coefficient up to 2 V/cm·Oe is predicted for the BTO:CFO VANs. In lateral heterostructures, ME coupling can be mediated by charge, strain and exchange coupling at the heterointerfaces.^[249-251] Compared to lateral multiferroic heterostructures, the ME coupling mechanisms in VANs are rarely reported. The BTO:CFO nanocomposites have recently been revisited by Schmitz-Antoniak and coworkers.^[150] Rectangular CFO nanopillars with 100~200 nm in size have been synthesized by pulsed laser deposition at 950 °C (Figure 6e). The couplings have been studied by using the soft X-ray absorption spectroscopy and circular/linear dichroism. Magnetic field was applied in both out-of-plane (*z*) direction and in-plane (*y*) direction. As shown in **Figures 14a** and **14b**, these two magnetic field directions induce different deformation in the CFO nanopillars. The in-plane magnetic field induces an electric in-plane polarization. Field-dependent soft XLD at the Ti L_{3,2} absorption edges, as shown in Figure 14c, shows that the Ti XLD (H_{main} parallel to *z*) increases three times from 2.0% to 6.5% by increasing the magnetic field strength. However, the Ti XLD (H_{main} perpendicular to *z*) only increases from 2.0% to 3.5%. Besides the BTO:CFO systems, other multiferroic nanocomposites have also been synthesized.^[252-255]

The ME coupling strength can be characterized by measuring the direct or converse ME coefficients. In the case of direct ME effect, a static magnetic field, superimposed with a small ac magnetic field, is applied to ME composites. The surface charge signal is then recorded for thin films.^[253] Oh *et al.*

investigated the ME coupling of a 300 nm BFO:CFO nanocomposite film with 1:1 volume ratio (CFO pillars in BFO matrix).^[253] A *dc* magnetic field with a small *ac* magnetic field ($H_{ac} = 4$ Oe) was used to excite the sample and induced charges (instead of voltages) were measured. The transverse ME coefficient α_{31} was ~ 60 mV/cm·Oe, which is five times larger than the longitudinal ME coefficient α_{33} . The larger transverse ME coefficient was attributed to the enhanced transverse magnetostriction of the CFO nanopillars. Through a magnetic cantilever method, direct ME coupling was also studied in BFO:CFO VANs thin films.^[256] The maximum ME coefficient was determined to be ~ 20 mV/cm·Oe. The reduced piezoelectric and piezomagnetic coefficients of the ferroelectric and ferromagnetic phases, due to substrate clamping effect, are responsible for the relatively small ME coupling coefficient. Yan *et al.* further studied the orientation effect on the ME coupling by using SrTiO₃ substrates with different orientations.^[257] The maximum ME coefficient for the *L-L* mode follows the trend of $ME_{(001)} > ME_{(110)} > ME_{(111)}$ (16, 15, and 8 mV/cm·Oe, respectively), which is correlated with the longitudinal piezoelectric coefficient d_{33} of the BiFeO₃ phase following $d_{33(001)} > d_{33(110)} > d_{33(111)}$. In addition, the strain in films with different orientations is different, following the trend of $\sigma_{(111)} > \sigma_{(110)} > \sigma_{(001)}$, which also contributes to the larger ME coupling in (001) nanocomposite films. Recently, flexible substrates have been used to grow functional oxide thin films via Van der Waals epitaxy or transfer.^[258, 259] Chu and coworkers reported the growth of BFO:CFO VANs on a flexible muscovite via van der Waals epitaxy.^[260] A ME coupling coefficient of 74 mV/cm·Oe was found in this bulk heterojunction.

In the case of the converse ME effect, electric fields are applied to ME composites and the change of magnetization is recorded. Thus, various techniques that can detect magnetic properties have been employed to validate and measure the converse ME effect in heterostructures. These methods include X-ray absorption spectroscopy,^[150, 249] ferromagnetic resonance,^[261, 262] vibrating sample magnetometer,^[199, 263] and magneto-optic Kerr effect.^[60] Regarding VANs, Fix *et al.* demonstrated tuning magnetization of La₂CoMnO₆:ZnO nanocomposite thin films by applying an electric field.^[264] Along with direct measurements, the magnetocapacitance effect can be also used to evaluate ME coupling strength. Using this method, an ME coefficient of $0.9 \mu\text{C}/\text{cm}\cdot\text{Oe}$ was estimated for BFO:CFO nanocomposites at 10 K.^[157]

Owing to the relatively conductive ferromagnetic phase penetrating through the whole film thickness of the vertically aligned nanocomposites, it is a challenge to measure the ME coupling directly by applying a large field across the nanocomposite samples. Scanning probing microscopy, a nanoscale imaging technique, has been used to characterize the ME effect in vertically aligned nanocomposites. For example, Zavaliche *et al.* investigated the electric field controlled magnetization switching in BFO:CFO VANs using magnetic force microscopy.^[265, 266] The perpendicular ME susceptibility, $\alpha_{33} = \Delta M/\Delta E$, is determined to be $0.01 \text{ Oe}\cdot\text{cm}/\text{V}$, where ΔM is the magnetization change of VANs under

different electric fields. Wang *et al.* grew BFO:CFO VANs on ferroelectric PMN-PT (001) substrates and investigated the electric field (5 kV/cm) induced magnetization changes.^[199] The electric field poling reduces out-of-plane remnant magnetizations and enhances the in-plane magnetizations. The static longitudinal ME susceptibility, α_{33} , is roughly estimated to be 0.5 Oe·cm/V. An alternative way is to measure the ferroelectric response under different magnetic fields. Such a method has been used to evaluate the DME effect in nanostructures including core-shell nanofibers and 0-3 type nanocomposites.^[267, 268]

Significant progresses have been made in multiferroic materials during the past decade. **Figure 15** summarized the ME coefficients in various single-phase and composite multiferroic materials.^[269] Single-phase multiferroic materials such as Cr₂O₃ and BiFeO₃ show relatively small ME coupling coefficients. Among the bulk composites, particulate composites exhibit relatively small ME coefficients with a value typically < 100 mV/cm·Oe. Laminate-like composites can exhibit much larger ME coefficient, ranging from 0.5 to 50 V/cm·Oe. In the nanocomposite films, ME coefficients are typically below 1 V/cm·Oe. Particularly, ME coefficients of VANs are in the range of 10~400 mV/cm·Oe. One of the advantages of 2-2 type nanocomposite films is the reduced leakage current, which is an issue in VANs due to the low resistivity magnetic component running through the film thickness. This could be one of the main reason that the ME coefficients are far below theoretical predictions. On the other hand, substrate clamping effect could be a challenge for 2-2 type heterostructures.

5.4 Vertical Interface Conduction

5.4.1 Strain/Defects Controlled Electronic Conductions

VANs with ordered vertical heterointerfaces provide an interesting platform to tune the vertical transport properties. One of the challenges, however, is to understand the interplay among strain, defect, vertical interface, and electronic conduction. Reduced leakage current and dielectric loss have been reported in BFO:Sm₂O₃, and BTO:Sm₂O₃ VANs. Yang *et al.* reported the growth of BFO:Sm₂O₃ VANs. As shown in **Figure 16a**, dielectric loss in these VANs was reduced compared to pure BFO and pure Sm₂O₃ films.^[270] Figure 16b shows the cross-sectional TEM image of BFO:Sm₂O₃ VANs with the alternating alignment of BFO and Sm₂O₃ vertical nanocolumns on STO substrate. Such a VAN exhibited significantly enhanced vertical interface area compared to lateral heterostructures. These enhanced properties are attributed to the increased vertical interfacial area and reduced oxygen vacancies in the BFO phase. Bi *et al.* furthered the study by changing the growth condition and phase ratios.^[98] The dielectric loss in BFO:Sm₂O₃ VANs was correlated with the tunable lattice strain and

microstructures. Via increasing laser frequency from 1 Hz to 10 Hz, the Sm_2O_3 nanopillar size can be reduced. This will lead to an increase in the vertical interfacial area. This will also make the strain coupling much more effective.^[95] For example, the out-of-plane strain in BFO can be switched from tension (substrate strain dominated) to compression (vertical strain dominated). A reduced dielectric loss was observed in VANs with larger out-of-plane compressive strain and smaller nanopillar feature size. Reduced leakage current was also reported in $\text{BTO}:\text{Sm}_2\text{O}_3$ VANs. Li *et al.* synthesized $\text{BTO}:\text{Sm}_2\text{O}_3$ nanocomposite thin films and studied the interfacial conduction.^[271] It was proposed that because of the structural discontinuity at the vertical interface as well as a large vertical lattice strain, the vertical interfaces trap oxygen vacancies. The movement of oxygen vacancies is confined by the interfacial misfit dislocations. These effects contributed to a relaxation behavior in $\text{BTO}:\text{Sm}_2\text{O}_3$ VAN films.^[122] Similar results have been reported in $\text{BFO}:\text{Sm}_2\text{O}_3$.^[272] Taking advantage of strain enhanced ferroelectricity and interface controlled dielectric loss, Lee *et al.* further explored the dielectric tunability in $\text{Ba}_{0.6}\text{Sr}_{0.4}\text{TiO}_3:\text{Sm}_2\text{O}_3$ VANs. A high and stable dielectric tunability (75% at 200 kV/cm) and low dielectric loss values ($\tan \delta < 0.01$) were achieved at room temperature.^[220] In a $\text{STO}:\text{Sm}_2\text{O}_3$ VAN, large dielectric constant tunability (49%), low tangent loss, high commutation quality factor (> 2800) were reported in the SrTiO_3 phase.^[219] The large vertical tensile strain was attributed to the enhanced dielectric properties in BSTO and STO.

In lateral heterostructures, one of intriguing phenomena is 2DEG at $\text{LaAlO}_3/\text{SrTiO}_3$ interfaces. The conduction mechanism is still under debate. Several hypotheses have been proposed including polar gating, interfacial intermixing, oxygen and cation off-stoichiometry and structural distortions.^[24, 273-275] Tuning vertical interface conduction has been reported. In a $\text{BFO}:\text{CFO}$ VAN, Hsieh *et al.* found that the vertical interface exhibited higher conduction than both BFO matrix and CFO nanopillars.^[276] The current image shows enhanced electronic conduction at the vertical interface between CFO pillar and BFO matrix which is consistent with observation in the $\text{STO}:\text{Sm}_2\text{O}_3$ VAN.^[123] First, oxygen vacancy, serving as a donor, provides electrons to the conduction. Secondly, Fe-rich CFO phase could be formed near the vertical interface. Both oxygen vacancies accumulation and segregation of Fe^{3+} ions in CFO could be the origin of this conduction. In a follow up study, electric fields applied by conductive atomic force microscopy (c-AFM) and PFM were used to manipulate the local conduction in $\text{BFO}:\text{CFO}$ VANs. It was found that the movement of oxygen vacancies was the key factor to control the vertical conduction. For the as-grown sample, the vertical interface is relatively conductive as the out-of-plane polarization is downward. **Figure 17** shows that the vertical conduction depends on the polarization direction. The vertical conduction is blocked by applying a negative tip bias (upward polarization).^[277] The positively charged oxygen vacancies will be attracted by the negative tip bias and thus accumulate on the top surface (Figure 17a). A positive bias (downward polarization) favors the interfacial conduction. Via a combination of c-AFM, PFM, and KFM (Figures 17b-17e), the conduction was explained. The as-grown $\text{BFO}:\text{CFO}$ VANs exhibit a down polarization and the vertical interface is conducting. After switching the polarization to upward (Figure 17c), the

conductive vertical interface disappears (Figure 17d). The KFM image confirmed the negative surface potential at the poled region. In a review article, Tra *et al.* summarized the electrical conduction at lateral heterostructures and vertical nanocomposites.^[278]

Different from lateral heterostructures and superlattices, VANs exhibit much higher density of vertical interfaces. Tunable vertical conduction in VANs can be used to design memristive devices. Lee *et al.* reported forming-free resistive switching in three different VANs including STO:Sm₂O₃, BTO:Sm₂O₃, and Ba_{0.6}Sr_{0.4}TiO₃:Sm₂O₃.^[123] The vertical resistance can be modulated between 10⁵-10⁸ Ω with excellent uniformity. Tunable electroresistance in these VANs was possibly due to the joule-heating induced oxygen vacancies drift localized at vertical heterointerfaces. Oxygen vacancies confined at vertical heterointerfaces were confirmed by STEM-EELS results. Figure 18(a) shows a plan-view HAADF-STEM image of STO:Sm₂O₃ VAN with the bright contrast represents the Sm₂O₃ phase while the dark contrast represents the STO phase. EELS scans across the vertical phase boundary were conducted to investigate chemical information. It was found that the oxygen content at these vertical heterointerfaces was below the theoretical estimation, indicating the existence of oxygen vacancies (Figure 18(b)). The interface structural incompatibility between perovskite SrTiO₃ and bixbyite Sm₂O₃ gives rise to oxygen deficiency. Oxygen vacancies migration modulated interfacial electronic barrier was responsible for the observed electroresistance in these VAN films, as also reported in other binary oxides based resistive switching devices.

5.4.2 Oxygen Vacancy and Strain Enhanced Ionic Conductions

The oxygen transport properties in oxide systems are not only of fundamental importance but also of technological interest in solid state devices such as solid oxide fuel cells (SOFC) at intermediated temperatures and resistive switching memory device.^[279-281] The oxygen diffusivity scales (C) almost linearly with oxygen vacancy concentration when the value of oxygen vacancy concentration is low. On the other hand, oxygen diffusion is a thermally activated process where C can be described by the Boltzmann relationship as,^[282]

$$C = C_0 \exp\left(\frac{-E_m}{k_B T}\right) \quad (15)$$

where C_0 is a constant and E_m denotes migration enthalpies, or energy barriers along this path. Compared to linear relationship between C and oxygen vacancy concentration, C changes exponentially with E_m which makes it a critical parameter to reduce. The oxygen migration energy is affected by the microstructure, oxygen stoichiometry, elastic strain, and so on. The strain and oxygen

vacancies at heterogeneous interfaces have been used to enhance charge-carrier density and mobility.^[282] For example, Sillassen *et al.* have reported that 58 nm thick epitaxial yttria stabilized zirconia (YSZ) films on MgO exhibited very high lateral ionic conductivity and low activation energy for oxygen migration.^[283] Also, giant ionic conductance was observed in strained YSZ/STO multilayers as reported by Barriocanal and coworkers, although there is still an ongoing debate on the underlying physics of the ionic versus electronic conductance in strained YSZ films.^[9] By using combined first principles-based calculations and kinetic Monte Carlo-based atomistic calculations, Kushima and Yildiz further revealed two competing processes in YSZ for altering oxygen migration barrier in different strain status.^[284] It was found that the low tensile strain increases the migration space and thus decreases the migration barrier. However, when the local relaxations occurs at large strain, the rearranged cation-oxygen bonds start to trap the oxygen and increase the migration barrier. An optimized 4% tensile strain has been identified with fastest D_0 .

Consistent with the fast oxygen ion diffusion in strained ultrathin films, the enhancement in lateral ionic conductivity has also been reported in many multilayer systems including YSZ/SrTiO₃,^[9] YSZ/Y₂O₃,^[285] and YSZ/Ce_{0.9}Gd_{0.1}O_{1.95} (GDC).^[286] The introduction of heterogeneous interfaces and tensile strain is ascribed to the observed enhancement. Compared to the multilayer systems which have shown to boost the oxygen ion diffusion along lateral interface direction, VANs exhibit some interesting results. First, VANs allows fast oxygen ion transport along the out-of-plane direction which is the favored charge flow direction of SOFCs. In addition, there is less thickness limitation for VAN films because the strain can be maintained in thick films with thicknesses up to microns, which is important for state-of-the-art SOFCs. For example, a two-phase YSZ:GDC nanocomposite electrolyte with vertically aligned interfaces has been demonstrated for thin film solid oxide fuel cells.^[287] As shown in Figure 19, beside smaller activation energy, the ionic conductivity of YSZ:GDC VAN electrolyte is 50% higher than that of the pure GDC thin films and at least two times higher than that of the single-phase YSZ thin films. In addition, this kind of VAN electrolyte has been successfully implemented into anode-supported single cells and demonstrated enhanced power performance in samples with VAN electrolyte. These findings have demonstrated the possibility of applying VANs in fuel cells and improving the out-of-plane ionic conductivity.

In a recent review article, Lee *et al.* discussed recent ionotronic progress using a device structure based on VANs.^[288] Similar to YSZ/GDC system, the enhancement in vertical ionic conductivity has been also demonstrated in other VAN systems.^[121, 123, 289, 290] The oxygen deficiency at vertical heterointerfaces due to the structural incompatibility^[123] and/or improved crystallinity of ionic conductors were proposed to explain the enhanced ionic conductivity in the STO:Sm₂O₃ VAN films.^[289] Yang *et al.* used scanning probe microscopy to show that the fast oxygen ion diffusion channels were observed at both the vertical interface and the Sm-doped CeO₂ nanopillars.^[289] Owing

to the tunable vertical lattice strain which can be achieved by selecting materials in VAN systems with different lattice mismatch, strain provides another freedom to control vertical ionic conductivity in VAN films. One of the most effective parameters to control strain is to use stiff nanopillars. For example, a group of rare earth oxides have been used to control strain in the SrZrO₃ phase.^[121] The vertical tensile strain in the SrZrO₃ phase increases as lattice constant of rare earth oxides increases. Previous studies in plain films as well as laterally aligned heteroepitaxy films have shown that ionic conductivity increases with tensile strain and decreases with compressive strain.^[285] The enhancement of ionic conductivity in strained SrZrO₃ VANs is consistent with the trend of tensile strain in SrZrO₃.

5.5 Oxygen Reduction Reaction

SOFCS have been widely studied as a promising candidate for clean power generation.^[291-295] However, slow kinetics of the oxygen reduction reaction (ORR) at cathodes is one of the primary obstacles to make SOFC technology economically feasible. The oxygen surface exchange and the oxygen diffusion process in oxide cathodes are the major factors limiting ORR. It has been reported that both effects are sensitive to the strain state,^[295, 296] and oxygen and cation stoichiometry.^[282, 297-300] Owing to the ability to control strain, defect, and heterogeneous interfaces, the VANs provide a unique structure to manipulate ORR that cannot be obtained in individual oxide cathode. Along with this idea, several cathode/cathode and cathode/electrolyte VANs have been demonstrated to enhance the ORR kinetics in recent years.^[301-303]

Wang and coworkers incorporated La_{0.5}Sr_{0.5}CoO_{3-δ} (LSCO)/Ce_{0.9}Gd_{0.1}O_{1.95} (CGO) VAN interlayers between the LSCO cathode and the CGO electrolyte, as shown in **Figure 20a**. Figure 20b is a high-resolution TEM image showing well-defined LSCO/CGO vertical nanocolumns. By applying such a structure in SOFCs, a much enhanced maximum power density was observed. The enhanced ORR rate is attributed to both the increase of cathode/electrolyte heterogeneous interface density and the triple phase boundary length.^[303] Those findings suggest that the incorporation of VANs between electrolyte and electrode generates several advantages. Both improved reaction kinetics and reduced polarization resistance at the electrode/electrolyte interface help to enhance the power output of SOFCs. Similar enhancement has been demonstrated in other cathode/electrolyte VAN systems including PrBaCo₂O_{5+δ} (PBCO)/CGO,^[301] La_{0.8}Sr_{0.2}MnO_{3-δ} (LSM)/Zr_{0.92}Y_{0.08}O_{1.96} (YSZ),^[304] and *etc.*

In addition, Yildiz and co-workers reported fast oxygen exchange kinetics in a (La_{1-x}Sr_x)CoO₃ (LSC113)/(La_{1-x}Sr_x)₂CoO₄ (LSC214) VAN cathode. Interestingly, the ORR rate increased 10 times compared to the single phase LSC113 and LSC214 films.^[302] It was claimed that VANs stabilize cation chemistry which enhances the ORR rate. Such an enhancement has also been reported in

LSC113/LSC214 superlattices.^[305] In addition, Han *et al.* used first-principles based calculations to examine the underlying physics of the oxygen reduction activity at the LSC113/LSC214 heterogeneous interface.^[306] The simulation revealed that both the lattice strain near the interface and the strongly anisotropic oxygen incorporation kinetics on the LSC214 are two main contributors to such an enhancement.

5.6 Photoelectrochemical Solar Water Oxidation

The efficiency of solar water splitting relies on charge carrier generation, separation, and delivery process in the semiconductor photoelectrodes. Introduction of heterogeneous interface and altering oxygen stoichiometry in VANs may lead to much higher efficiency. Recent studies have shown strongly enhanced photoelectrochemical water splitting in self-assembled SrTiO₃:ZnFe₂O₄ (STO:ZFO) VAN films.^[307] The photocurrent density of STO:ZFO VAN films reaches 0.188 mA/cm² at 1.23 V, which was several times higher than that of individual STO and ZFO films, respectively. It was argued that the enhancement in water oxidation efficiency originates from enhanced photo-induced charge separation. The enhanced separation of hole and electron is due to the high crystallinity, high epitaxial quality of these vertical nanostructure.

Enhancement of photoelectrochemical solar water oxidation was also observed in quite a few of other systems. Chu and coworkers have investigated photocatalysts in BFO:ε-Fe₂O₃ VANs by investigating the band structure, ultrafast time-resolved spectroscopy and electrochemical impedance spectroscopy.^[308] It was found the VAN structure assists photoexcited carrier separation and suppresses electron-hole recombination, giving rise to enhanced photoelectrochemical performance in this VAN system as well as in the NiWO₄:WO₃ VAN system.^[309] In another approach, Abhijeet *et al.* developed substrate-supported mesoporous structures which are achieved by first growing STO:MgO VANs, followed by selective etching of MgO nanopillars.^[310] The mesoporous structure with high surface area and high crystalline shows much improved performance compared to planar STO thin films. Also, metal Ir nanopillars embedded in SrTiO₃ VAN system have been reported by Lippmaa and coworkers. A strongly enhanced photocarrier transport efficiency is observed in the Ir/SrTiO₃ Schottky space charge regions. The conducting pillars provide an efficient charge extraction path. Although enhanced photoelectrochemical performance has been observed in several VAN systems, the research about the relationship between solar water splitting process with strain, defect and interface structure is still in its early stage and warrants further exploration.

6 Conclusion and Outlook

There are many research activities in different technological fronts using VAN-based structures. It is very hard to cover all efforts in this emergent field in this review. Initial development of VANs was mainly focused on the growth and characterization of different materials systems with a significant focus on the growth and optimization. The growth mechanisms of VANs have been investigated in different theoretical themes. Recent efforts have been focused on functionality tuning as well as potential applications in electronics and ionotronics by taking advantage of the vertical strain, defect and interface. However, there are still many open questions that include, but not limited to:

- 1) How the vertical strain is relaxed laterally and how can we design uniform vertical strain in VANs? Theoretical themes in this direction are lacking and experimental efforts are rare.
- 2) VAN systems naturally form different types of defects and/or modify microstructure to accommodate large misfit strain at the vertical interface and release the strain energy. Vertical strain is certainly one of the most critical factors in tuning a variety of physical properties. However, the role of defects and unique microstructure on the physical properties such as electron transport, ionic conduction, superconductivity, and so on needs to be fully investigated. The study of using strain to control of defect/microstructure as well as the functional property is still in the early stage.
- 3) Due to the complex entanglement of defect, strain and interface, the origin of functionality tuning may not be exclusive. The complexity is not unique to VANs. It also appears in conventional heterostructures and superlattices. Isolating one factor from another is important to study the effect of defect, strain and interface on the functionality.
- 4) Taking advantage of the unique characteristics of VANs such as tunability in defect, strain, microstructure and interface, functionality tuning has been accomplished in certain materials systems. There are a variety of physical properties such as conductivity, permittivity, elastic constant, and specific heat capacity can be explored in VANs.^[311] Controlling these physical properties by the external stimuli such as electric field, magnetic field, stress, heat, and light and internal stimuli such as defect, strain and interface could provide numerous opportunities

to control functional properties. For instance, optical properties of VANs are rarely studied. Some initial reports have already shown some interesting properties.^[312-315]

- 5) Using VAN templates to control or tune functionality in other functional materials has been rarely explored. For example, combining VANs with quantum materials could open a new field to explore physics and control functionality.

Acknowledgements

The work at Los Alamos National Laboratory was supported by the NNSA's Laboratory Directed Research and Development Program and was performed, in part, at the Center for Integrated Nanotechnologies, an Office of Science User Facility operated for the U.S. Department of Energy (DOE) Office of Science. Los Alamos National Laboratory, an affirmative action equal opportunity employer, is operated by Los Alamos National Security, LLC, for the National Nuclear Security Administration of the U.S. Department of Energy under contract DE-AC52-06NA25396.

Conflict of Interest

The authors declare no conflict of interest.

References

- [1] D. G. Schlom, J. H. Haeni, J. Lettieri, C. D. Theis, W. Tian, J. C. Jiang, X. Q. Pan, *Mat. Sci. Eng. B-Solid* 2001, 87, 282.
- [2] E. J. Monkman, C. Adamo, J. A. Mundy, D. E. Shai, J. W. Harter, D. W. Shen, B. Burganov, D. A. Muller, D. G. Schlom, K. M. Shen, *Nat. Mater.* 2012, 11, 855.
- [3] J. Son, P. Moetakef, B. Jalan, O. Bierwagen, N. J. Wright, R. Engel-Herbert, S. Stemmer, *Nat. Mater.* 2010, 9, 482.
- [4] J. Wang, J. B. Neaton, H. Zheng, V. Nagarajan, S. B. Ogale, B. Liu, D. Viehland, V. Vaithyanathan, D. G. Schlom, U. V. Waghmare, N. A. Spaldin, K. M. Rabe, M. Wuttig, R. Ramesh, *Science* 2003, 299, 1719.

- [5] J. L. Macmanus-Driscoll, S. R. Foltyn, Q. X. Jia, H. Wang, A. Serquis, L. Civale, B. Maiorov, M. E. Hawley, M. P. Maley, D. E. Peterson, *Nat. Mater.* 2004, 3, 439.
- [6] H. N. Lee, H. M. Christen, M. F. Chisholm, C. M. Rouleau, D. H. Lowndes, *Nature* 2005, 433, 395.
- [7] A. Ohtomo, H. Y. Hwang, *Nature* 2004, 427, 423.
- [8] M. Gibert, P. Zubko, R. Scherwitzl, J. Iniguez, J. M. Triscone, *Nat. Mater.* 2012, 11, 195.
- [9] J. Garcia-Barriocanal, A. Rivera-Calzada, M. Varela, Z. Sefrioui, E. Iborra, C. Leon, S. J. Pennycook, J. Santamaria, *Science* 2008, 321, 676.
- [10] J. Matsuno, N. Ogawa, K. Yasuda, F. Kagawa, W. Koshibae, N. Nagaosa, Y. Tokura, M. Kawasaki, *Sci. Adv.* 2016, 2, e1600304.
- [11] J. Nichols, X. Gao, S. Lee, T. L. Meyer, J. W. Freeland, V. Lauter, D. Yi, J. Liu, D. Haskel, J. R. Petrie, E.-J. Guo, A. Herklotz, D. Lee, T. Z. Ward, G. Eres, M. R. Fitzsimmons, H. N. Lee, *Nat. Commun.* 2016, 7, 12721.
- [12] P. D. C. King, H. I. Wei, Y. F. Nie, M. Uchida, C. Adamo, S. Zhu, X. He, I. Bozovic, D. G. Schlom, K. M. Shen, *Nat. Nanotechnol.* 2014, 9, 443.
- [13] M. Huijben, L. W. Martin, Y. H. Chu, M. B. Holcomb, P. Yu, G. Rijnders, D. H. A. Blank, R. Ramesh, *Phys. Rev. B* 2008, 78, 094413.
- [14] Y. H. Sun, Y. G. Zhao, H. F. Tian, C. M. Xiong, B. T. Xie, M. H. Zhu, S. Park, W. D. Wu, Q. Li, *Phys. Rev. B* 2008, 78, 024412.
- [15] M. A. Torija, M. Sharma, M. R. Fitzsimmons, M. Varela, C. Leighton, *J. Appl. Phys.* 2008, 104, 023901.
- [16] A. Tebano, C. Aruta, P. G. Medaglia, F. Tozzi, G. Balestrino, A. A. Sidorenko, G. Allodi, R. De Renzi, G. Ghiringhelli, C. Dallera, L. Braicovich, N. B. Brookes, *Phys. Rev. B* 2006, 74, 245116.
- [17] J. S. Lee, D. A. Arena, P. Yu, C. S. Nelson, R. Fan, C. J. Kinane, S. Langridge, M. D. Rossell, R. Ramesh, C. C. Kao, *Phys. Rev. Lett.* 2010, 105, 257204.
- [18] F. Y. Bruno, J. Garcia-Barriocanal, M. Varela, N. M. Nemes, P. Thakur, J. C. Cezar, N. B. Brookes, A. Rivera-Calzada, M. Garcia-Hernandez, C. Leon, S. Okamoto, S. J. Pennycook, J. Santamaria, *Phys. Rev. Lett.* 2011, 106, 147205.
- [19] H. Boschker, J. Verbeeck, R. Egoavil, S. Bals, G. van Tendeloo, M. Huijben, E. P. Houwman, G. Koster, D. H. A. Blank, G. Rijnders, *Adv. Funct. Mater.* 2012, 22, 2235.
- [20] R. Peng, H. C. Xu, M. Xia, M. Xia, J. F. Zhao, X. Xie, D. F. Xu, B. P. Xie, D. L. Feng, *Appl. Phys. Lett.* 2014, 104, 081606.

- [21] A. P. Chen, Q. Wang, M. R. Fitzsimmons, E. Enriquez, M. Weigand, Z. Harrell, B. McFarland, X. Lü, P. Dowden, J. L. MacManus-Driscoll, D. Yarotski, Q. X. Jia, *Adv. Mater.* 2017, 29, 1700672.
- [22] E. J. Moon, P. V. Balachandran, B. J. Kirby, D. J. Keavney, R. J. Sichel-Tissot, C. M. Schlepütz, E. Karapetrova, X. M. Cheng, J. M. Rondinelli, S. J. May, *Nano Lett.* 2014, 14, 2509.
- [23] Z. Liao, M. Huijben, Z. Zhong, N. Gauquelin, S. Macke, R. J. Green, S. Van Aert, J. Verbeeck, G. Van Tendeloo, K. Held, G. A. Sawatzky, G. Koster, G. Rijnders, *Nat. Mater.* 2016, 15, 425.
- [24] M. P. Warusawithana, C. Richter, J. A. Mundy, P. Roy, J. Ludwig, S. Paetel, T. Heeg, A. A. Pawlicki, L. F. Kourkoutis, M. Zheng, M. Lee, B. Mulcahy, W. Zander, Y. Zhu, J. Schubert, J. N. Eckstein, D. A. Muller, C. S. Hellberg, J. Mannhart, D. G. Schlom, *Nat. Commun.* 2013, 4, 2351.
- [25] X. J. Lu, A. P. Chen, Y. K. Luo, P. Lu, Y. M. Dai, E. Enriquez, P. Dowden, H. W. Xu, P. G. Kotula, A. K. Azad, D. A. Yarotski, R. P. Prasankumar, A. J. Taylor, J. D. Thompson, Q. X. Jia, *Nano Lett.* 2016, 16, 5751.
- [26] A. Kalabukhov, R. Gunnarsson, J. Borjesson, E. Olsson, T. Claeson, D. Winkler, *Phys. Rev. B* 2007, 75, 121404.
- [27] L. Qiao, T. C. Droubay, V. Shutthanandan, Z. Zhu, P. V. Sushko, S. A. Chambers, *J. Phys.-Condens. Mat.* 2010, 22, 312201.
- [28] F. Schoofs, M. A. Carpenter, M. E. Vickers, M. Egilmez, T. Fix, J. E. Kleibeuker, J. L. MacManus-Driscoll, M. G. Blamire, *J. Phys.-Condens. Mat.* 2013, 25, 175005.
- [29] H. Zheng, J. Wang, S. E. Lofland, Z. Ma, L. Mohaddes-Ardabili, T. Zhao, L. Salamanca-Riba, S. R. Shinde, S. B. Ogale, F. Bai, D. Viehland, Y. Jia, D. G. Schlom, M. Wuttig, A. Roytburd, R. Ramesh, *Science* 2004, 303, 661.
- [30] J. L. MacManus-Driscoll, P. Zerrer, H. Y. Wang, H. Yang, J. Yoon, A. Fouchet, R. Yu, M. G. Blamire, Q. X. Jia, *Nat. Mater.* 2008, 7, 314.
- [31] R. People, J. C. Bean, *Appl. Phys. Lett.* 1985, 47, 322.
- [32] L. F. Kourkoutis, J. H. Song, H. Y. Hwang, D. A. Muller, *P. Natl. Acad. Sci. U. S. A.* 2010, 107, 11682.
- [33] J. Narayan, B. C. Larson, *J. Appl. Phys.* 2003, 93, 278.
- [34] M. R. Bayati, R. Molaei, R. J. Narayan, J. Narayan, H. Zhou, S. J. Pennycook, *Appl. Phys. Lett.* 2012, 100, 251606.
- [35] Y. Y. Zhu, C. Y. Song, A. M. Minor, H. Y. Wang, *Microsc. Microanal.* 2013, 19, 706.

- [36] D. G. Schlom, L. Q. Chen, C. B. Eom, K. M. Rabe, S. K. Streiffer, J. M. Triscone, *Annu. Rev. Mater. Res.* 2007, 37, 589.
- [37] D. G. Schlom, L. Q. Chen, C. J. Fennie, V. Gopalan, D. A. Muller, X. Q. Pan, R. Ramesh, R. Uecker, *Mrs Bull* 2014, 39, 118.
- [38] W. T. Chang, J. S. Horwitz, A. C. Carter, J. M. Pond, S. W. Kirchoefer, C. M. Gilmore, D. B. Chrisey, *Appl. Phys. Lett.* 1999, 74, 1033.
- [39] J. H. Haeni, P. Irvin, W. Chang, R. Uecker, P. Reiche, Y. L. Li, S. Choudhury, W. Tian, M. E. Hawley, B. Craigo, A. K. Tagantsev, X. Q. Pan, S. K. Streiffer, L. Q. Chen, S. W. Kirchoefer, J. Levy, D. G. Schlom, *Nature* 2004, 430, 758.
- [40] K. J. Choi, M. Biegalski, Y. L. Li, A. Sharan, J. Schubert, R. Uecker, P. Reiche, Y. B. Chen, X. Q. Pan, V. Gopalan, L. Q. Chen, D. G. Schlom, C. B. Eom, *Science* 2004, 306, 1005.
- [41] E. Mikheev, A. J. Hauser, B. Himmetoglu, N. E. Moreno, A. Janotti, C. G. Van de Walle, S. Stemmer, *Sci. Adv.* 2015, 1, e1500797.
- [42] B. Jalan, S. J. Allen, G. E. Beltz, P. Moetakef, S. Stemmer, *Appl. Phys. Lett.* 2011, 98, 132102.
- [43] J. Liu, M. Kareev, B. Gray, J. Kim, P. Ryan, B. Dabrowski, J. Freeland, J. Chakhalian, *Appl. Phys. Lett.* 2010, 96, 233110.
- [44] Y. Gim, T. Hudson, Y. Fan, C. Kwon, A. T. Findikoglu, B. J. Gibbons, B. H. Park, Q. X. Jia, *Appl. Phys. Lett.* 2000, 77, 1200.
- [45] L. G. Li, W. R. Zhang, F. Khatkhatay, J. Jian, M. Fan, Q. Su, Y. Y. Zhu, A. P. Chen, P. Lu, X. H. Zhang, H. Y. Wang, *ACS Appl. Mater. Interfaces* 2015, 7, 11631.
- [46] L. Zhou, H. Song, K. Liu, Z. Luan, P. Wang, L. Sun, S. Jiang, H. Xiang, Y. Chen, J. Du, H. Ding, K. Xia, J. Xiao, D. Wu, *Sci. Adv.* 2018, 4, eaao3318.
- [47] H. Guo, Z. Wang, S. Dong, S. Ghosh, M. Saghayezhian, L. Chen, Y. Weng, A. Herklotz, T. Z. Ward, R. Jin, S. T. Pantelides, Y. Zhu, J. Zhang, E. W. Plummer, *P. Natl. Acad. Sci. U. S. A.* 2017, 114, E5062.
- [48] E. J. Guo, J. R. Petrie, M. A. Roldan, Q. Li, R. D. Desautels, T. Charlton, A. Herklotz, J. Nichols, J. van Lierop, J. W. Freeland, S. V. Kalinin, H. N. Lee, M. R. Fitzsimmons, *Adv. Mater.* 2017, 29, 1700790.
- [49] J. Chakhalian, J. W. Freeland, A. J. Millis, C. Panagopoulos, J. M. Rondinelli, *Rev Mod Phys* 2014, 86, 1189.

- [50] R. B. Comes, S. R. Spurgeon, S. M. Heald, D. M. Kepaptsoglou, L. Jones, P. V. Ong, M. E. Bowden, Q. M. Ramasse, P. V. Sushko, S. A. Chambers, *Adv. Mater. Interfaces* 2016, 3, 1500779.
- [51] J. M. Rondinelli, S. J. May, J. W. Freeland, *Mrs Bull* 2012, 37, 261.
- [52] S. J. May, J. W. Kim, J. M. Rondinelli, E. Karapetrova, N. A. Spaldin, A. Bhattacharya, P. J. Ryan, *Phys. Rev. B* 2010, 82, 014110.
- [53] J. M. Rondinelli, C. J. Fennie, *Adv. Mater.* 2012, 24, 1961.
- [54] S. R. Spurgeon, P. V. Balachandran, D. M. Kepaptsoglou, A. R. Damodaran, J. Karthik, S. Nejadi, L. Jones, H. Ambaye, V. Lauter, Q. M. Ramasse, K. K. S. Lau, L. W. Martin, J. M. Rondinelli, M. L. Taheri, *Nat. Commun.* 2015, 6, 6735.
- [55] A. K. Yadav, C. T. Nelson, S. L. Hsu, Z. Hong, J. D. Clarkson, C. M. Schlepuetz, A. R. Damodaran, P. Shafer, E. Arenholz, L. R. Dedon, D. Chen, A. Vishwanath, A. M. Minor, L. Q. Chen, J. F. Scott, L. W. Martin, R. Ramesh, *Nature* 2016, 530, 198.
- [56] G. M. Prinz, T. Gerber, A. Lorke, M. Muller, *Appl. Phys. Lett.* 2016, 109, 202401.
- [57] J. Liu, S. Okamoto, M. Van Veenendaal, M. Kareev, B. Gray, P. Ryan, J. Freeland, J. Chakhalian, *Phys. Rev. B* 2011, 83, 161102.
- [58] M. K. Lee, T. K. Nath, C. B. Eom, M. C. Smoak, F. Tsui, *Appl. Phys. Lett.* 2000, 77, 3547.
- [59] A. D. Rata, A. Herklotz, K. Nenkov, L. Schultz, K. Dorr, *Phys. Rev. Lett.* 2008, 100, 076401.
- [60] H. J. A. Molegraaf, J. Hoffman, C. A. F. Vaz, S. Gariglio, D. van der Marel, C. H. Ahn, J. M. Triscone, *Adv. Mater.* 2009, 21, 3470.
- [61] I. C. Infante, F. Sanchez, J. Fontcuberta, M. Wojcik, E. Jedryka, S. Estrade, F. Peiro, J. Arbiol, V. Laukhin, J. P. Espinos, *Phys. Rev. B* 2007, 76, 224415.
- [62] R. People, J. C. Bean, *Appl. Phys. Lett.* 1985, 47, 322.
- [63] J. W. Matthews, A. E. Blakeslee, *J. Cryst. Growth* 1974, 27, 118.
- [64] Y. B. Chen, H. P. Sun, M. B. Katz, X. Q. Pan, K. J. Choi, H. W. Jang, C. B. Eom, *Appl. Phys. Lett.* 2007, 91, 252906.
- [65] A. Malachias, S. Kycia, G. Medeiros-Ribeiro, R. Magalhaes-Paniago, T. I. Kamins, R. S. Williams, *Phys. Rev. Lett.* 2003, 91, 176101.
- [66] A. Vailionis, H. Boschker, W. Siemons, E. P. Houwman, D. H. A. Blank, G. Rijnders, G. Koster, *Phys. Rev. B* 2011, 83, 064101.

- [67] J. Gazquez, S. Bose, M. Sharma, M. A. Torija, S. J. Pennycook, C. Leighton, M. Varela, *APL Mater.* 2013, 1, 012105.
- [68] U. Aschauer, R. Pfenninger, S. M. Selbach, T. Grande, N. A. Spaldin, *Phys. Rev. B* 2013, 88, 054111.
- [69] A. P. Chen, H. H. Zhou, Z. X. Bi, Y. Y. Zhu, Z. P. Luo, A. Bayraktaroglu, J. Phillips, E. M. Choi, J. L. MacManus-Driscoll, S. J. Pennycook, J. Narayan, Q. X. Jia, X. H. Zhang, H. Y. Wang, *Adv. Mater.* 2013, 25, 1028.
- [70] Y. Y. Zhu, A. P. Chen, H. H. Zhou, W. R. Zhang, J. Narayan, J. L. MacManus-Driscoll, Q. X. Jia, H. Y. Wang, *APL Mater.* 2013, 1, 050702.
- [71] N. Farag, M. Bobeth, W. Pompe, A. E. Romanov, J. S. Speck, *J. Appl. Phys.* 2005, 97, 113516.
- [72] O. I. Lebedev, G. Van Tendeloo, S. Amelinckx, F. Razavi, H. U. Habermeier, *Philos. Mag. A* 2001, 81, 797.
- [73] J. Santiso, L. Balcells, Z. Konstantinovic, J. Roqueta, P. Ferrer, A. Pomar, B. Martinez, F. Sandiumenge, *Crystengcomm* 2013, 15, 3908.
- [74] U. Gebhardt, N. V. Kasper, A. Vigliante, P. Wochner, H. Dosch, F. S. Razavi, H. U. Habermeier, *Phys. Rev. Lett.* 2007, 98, 096101.
- [75] J. E. Giencke, C. M. Folkman, S. H. Baek, C. B. Eom, *Curr. Opin. Solid State Mater. Sci.* 2014, 18, 39.
- [76] M. Luysberg, R. Sofin, S. Arora, I. Shvets, *Phys. Rev. B* 2009, 80, 024111.
- [77] E. Dimakis, E. Iliopoulos, K. Tsagaraki, A. Adikimenakis, A. Georgakilas, *Appl. Phys. Lett.* 2006, 88, 191918.
- [78] P. E. Janolin, A. S. Anokhin, Z. Gui, V. M. Mukhortov, Y. I. Golovko, N. Guiblin, S. Ravy, M. El Marssi, Y. I. Yuzyuk, L. Bellaiche, B. Dkhil, *J. Phys.-Condens. Mat.* 2014, 26, 292201.
- [79] L. Zhang, Y. Yuan, J. Lapano, M. Brahlek, S. Lei, B. Kabius, V. Gopalan, R. Engel-Herbert, *Acs Nano* 2018, 12, 1306.
- [80] Y. Suzuki, H. Y. Hwang, S. W. Cheong, R. B. vanDover, *Appl. Phys. Lett.* 1997, 71, 140.
- [81] J. Dho, Y. N. Kim, Y. S. Hwang, J. C. Kim, N. H. Hur, *Appl. Phys. Lett.* 2003, 82, 1434.
- [82] Y. Wu, Y. Suzuki, U. Rudiger, J. Yu, A. D. Kent, T. K. Nath, C. B. Eom, *Appl. Phys. Lett.* 1999, 75, 2295.
- [83] P. Dey, T. K. Nath, A. Taraphder, *Appl. Phys. Lett.* 2007, 91, 012511.

- [84] F. Yang, N. Kemik, M. D. Biegalski, H. M. Christen, E. Arenholz, Y. Takamura, *Appl. Phys. Lett.* 2010, 97, 092503.
- [85] C. Adamo, X. Ke, H. Q. Wang, H. L. Xin, T. Heeg, M. E. Hawley, W. Zander, J. Schubert, P. Schiffer, D. A. Muller, L. Maritato, D. G. Schlom, *Appl. Phys. Lett.* 2009, 95, 112504.
- [86] N. A. Pertsev, A. K. Tagantsev, N. Setter, *Phys. Rev. B* 2000, 61, R825.
- [87] Y. S. Kim, J. S. Choi, J. Kim, S. J. Moon, B. H. Park, J. Yu, J. H. Kwon, M. Kim, J. S. Chung, T. W. Noh, J. G. Yoon, *Appl. Phys. Lett.* 2010, 97, 242907.
- [88] X. L. Zhou, L. D. Miao, I. Stern, P. Silwal, D. H. Kim, *Mat. Sci. Eng. B* 2012, 177, 685.
- [89] F. Johann, A. Morelli, D. Biggemann, M. Arredondo, I. Vrejoiu, *Phys. Rev. B* 2011, 84, 094105.
- [90] A. R. Chaudhuri, M. Arredondo, A. Hahnel, A. Morelli, M. Becker, M. Alexe, I. Vrejoiu, *Phys. Rev. B* 2011, 84, 054112.
- [91] B. Xiao, V. Avrutin, H. R. Liu, E. Rowe, J. Leach, X. Gu, U. Ozgur, H. Morkoc, W. Chang, L. M. B. Aldredge, S. W. Kirchoefer, J. M. Pond, *Appl. Phys. Lett.* 2009, 95, 012907.
- [92] M. D. Biegalski, E. Vlahos, G. Sheng, Y. L. Li, M. Bernhagen, P. Reiche, R. Uecker, S. K. Streiffer, L. Q. Chen, V. Gopalan, D. G. Schlom, S. Trolier-McKinstry, *Phys. Rev. B* 2009, 79, 224117
- [93] M. P. Warusawithana, C. Cen, C. R. Slesman, J. C. Woicik, Y. L. Li, L. F. Kourkoutis, J. A. Klug, H. Li, P. Ryan, L. P. Wang, M. Bedzyk, D. A. Muller, L. Q. Chen, J. Levy, D. G. Schlom, *Science* 2009, 324, 367.
- [94] Y. L. Li, S. Choudhury, J. H. Haeni, M. D. Biegalski, A. Vasudevarao, A. Sharan, H. Z. Ma, J. Levy, V. Gopalan, S. Trolier-McKinstry, D. G. Schlom, Q. X. Jia, L. Q. Chen, *Phys. Rev. B* 2006, 73, 184112.
- [95] A. P. Chen, J.-M. Hu, P. Lu, T. N. Yang, W. Zhang, L. Li, T. Ahmed, E. Enriquez, M. Weigand, Q. Su, H. Y. Wang, J.-X. Zhu, J. L. MacManus-Driscoll, L. Q. Chen, D. Yarotski, Q. X. Jia, *Sci. Adv.* 2016, 2, e1600245.
- [96] S. A. Harrington, J. Y. Zhai, S. Denev, V. Gopalan, H. Y. Wang, Z. X. Bi, S. A. T. Redfern, S. H. Baek, C. W. Bark, C. B. Eom, Q. X. Jia, M. E. Vickers, J. L. MacManus-Driscoll, *Nat. Nanotechnol.* 2011, 6, 491.
- [97] A. P. Chen, W. R. Zhang, F. Khatkatay, Q. Su, C. F. Tsai, L. Chen, Q. X. Jia, J. L. MacManus-Driscoll, H. Wang, *Appl. Phys. Lett.* 2013, 102, 093114.

- [98] Z. X. Bi, J. H. Lee, H. Yang, Q. X. Jia, J. L. MacManus-Driscoll, H. Y. Wang, *J. Appl. Phys.* 2009, 106, 094309.
- [99] Y. Zhu, W. S. Chang, R. Yu, R. Liu, T.-C. Wei, J.-H. He, Y.-H. Chu, Q. Zhan, *Appl. Phys. Lett.* 2015, 107, 191902.
- [100] N. Dix, R. Muralidharan, J. Guyonnet, B. Warot-Fonrose, M. Varela, P. Paruch, F. Sanchez, J. Fontcuberta, *Appl. Phys. Lett.* 2009, 95, 062907.
- [101] Z. G. Wang, R. Viswan, B. L. Hu, V. G. Harris, J. F. Li, D. Viehland, *Phys. Status Solidi-RRL* 2012, 6, 92.
- [102] R. Groenen, J. Smit, K. Orsel, A. Vailionis, B. Bastiaens, M. Huijben, K. Boller, G. Rijnders, G. Koster, *APL Mater.* 2015, 3, 070701.
- [103] E. Enriquez, A. P. Chen, Z. Harrell, P. Dowden, N. Koskelo, J. Roback, M. Janoschek, C. L. Chen, Q. X. Jia, *Sci. Rep.* 2017, 7, 46184
- [104] A. P. Chen, F. Khatkhatay, W. Zhang, C. Jacob, L. Jiao, H. Y. Wang, *J. Appl. Phys.* 2013, 114, 124101.
- [105] V. Moshnyaga, B. Damaschke, O. Shapoval, A. Belenchuk, J. Faupel, O. I. Lebedev, J. Verbeeck, G. Van Tendeloo, M. Mucksch, V. Tsurkan, R. Tidecks, K. Samwer, *Nat. Mater.* 2005, 2, 247.
- [106] H. Zheng, J. Kreisel, Y. H. Chu, R. Ramesh, L. Salamanca-Riba, *Appl. Phys. Lett.* 2007, 90, 113113.
- [107] V. Schuler, F. J. Bonilla, D. Demaille, A. Coati, A. Vlad, Y. Garreau, M. Sauvage-Simkin, A. Novikova, E. Fonda, S. Hidki, V. Etgens, F. Vidal, Y. L. Zheng, *Nano Research* 2015, 8, 1964.
- [108] Y. Y. Zhu, C. F. Tsai, J. Wang, J. H. Kwon, H. Y. Wang, C. V. Varanasi, J. Burke, L. Brunke, P. N. Barnes, *J. Mater. Res.* 2012, 27, 1763.
- [109] C. Cantoni, Y. F. Gao, S. H. Wee, E. D. Specht, J. Gazquez, J. Y. Meng, S. J. Pennycook, A. Goyal, *Acs Nano* 2011, 5, 4783.
- [110] T. Horide, T. Kitamura, A. Ichinose, K. Matsumoto, *Jpn. J. Appl. Phys.* 2014, 53, 083101.
- [111] A. Artemev, J. Slutsker, A. L. Roytburd, *Acta Mater.* 2005, 53, 3425.
- [112] T. O. Farmer, E.-J. Guo, T. Wang, R. D. Desautels, A. P. Chen, Q. X. Jia, J. Borchers, D. A. Gilbert, B. Holladay, S. K. Sinha, M. R. Fitzsimmons, Submitted 2018.
- [113] A. P. Chen, Z. X. Bi, C. F. Tsai, J. Lee, Q. Su, X. H. Zhang, Q. X. Jia, J. L. MacManus-Driscoll, H. Y. Wang, *Adv. Funct. Mater.* 2011, 21, 2423.

- [114] J. MacManus-Driscoll, A. Suwardi, A. Kursumovic, Z. X. Bi, C. F. Tsai, H. Y. Wang, Q. X. Jia, O. J. Lee, *APL Mater.* 2015, 3, 062507.
- [115] W. R. Zhang, M. Fan, L. G. Li, A. P. Chen, Q. Su, Q. X. Jia, J. L. MacManus-Driscoll, H. Y. Wang, *Appl. Phys. Lett.* 2015, 107, 212901.
- [116] W. R. Zhang, A. P. Chen, J. Jian, Y. Y. Zhu, L. Chen, P. Lu, Q. X. Jia, J. L. MacManus-Driscoll, X. H. Zhang, H. Y. Wang, *Nanoscale* 2015, 7, 13808.
- [117] R. Zhao, W. W. Li, J. H. Lee, E. M. Choi, Y. Liang, W. Zhang, R. J. Tang, H. Y. Wang, Q. X. Jia, J. L. MacManus-Driscoll, H. Yang, *Adv. Funct. Mater.* 2014, 24, 5240.
- [118] A. P. Chen, W. R. Zhang, J. Jian, H. Y. Wang, C. F. Tsai, Q. Su, Q. X. Jia, J. L. MacManus-Driscoll, *J. Mater. Res.* 2013, 28, 1707.
- [119] J. L. MacManus-Driscoll, A. Suwardi, H. Wang, *Mrs Bull* 2015, 40, 933.
- [120] A. P. Chen, Z. X. Bi, H. Hazariwala, X. H. Zhang, Q. Su, L. Chen, Q. X. Jia, J. L. MacManus-Driscoll, H. Y. Wang, *Nanotechnology* 2011, 22, 315712.
- [121] S. Lee, W. R. Zhang, F. Khatkhatay, Q. X. Jia, H. Y. Wang, J. L. MacManus-Driscoll, *Adv. Funct. Mater.* 2015, 25, 4328.
- [122] W. W. Li, W. Zhang, L. Wang, J. X. Gu, A. P. Chen, R. Zhao, Y. Liang, H. Z. Guo, R. J. Tang, C. C. Wang, K. J. Jin, H. Y. Wang, H. Yang, *Sci. Rep.* 2015, 5, 11335.
- [123] S. Lee, A. Sangle, P. Lu, A. P. Chen, W. R. Zhang, J. S. Lee, H. Y. Wang, Q. X. Jia, J. L. MacManus-Driscoll, *Adv. Mater.* 2014, 26, 6284.
- [124] J. L. MacManus-Driscoll, *Adv. Funct. Mater.* 2010, 20, 2035.
- [125] A. P. Chen, Z. X. Bi, Q. X. Jia, J. L. MacManus-Driscoll, H. Y. Wang, *Acta Mater.* 2013, 61, 2783.
- [126] W. R. Zhang, A. P. Chen, Z. K. Bi, Q. X. Jia, J. L. MacManus-Driscoll, H. Y. Wang, *Curr. Opin. Solid State Mater. Sci.* 2014, 18, 6.
- [127] J. Huang, J. L. MacManus Driscoll, H. Y. Wang, *J. Mater. Res.* 2017, 32, 4054.
- [128] D. H. Kim, X. Sun, T. C. Kim, Y. J. Eun, T. Lee, S. G. Jeong, C. A. Ross, *ACS Appl. Mater. Interfaces* 2016, 8, 2673.
- [129] I. Levin, J. H. Li, J. Slutsker, A. L. Roytburd, *Adv. Mater.* 2006, 18, 2044.
- [130] Y. U. Wang, Y. M. Jin, A. G. Khachatryan, *Appl. Phys. Lett.* 2002, 80, 4513.
- [131] D. J. Seol, S. Y. Hu, Y. L. Li, J. Shen, K. H. Oh, L. Q. Chen, *Met Mater-Int* 2003, 9, 61.

- [132] X. B. Liao, Y. Ni, H. Yang, L. H. He, *Appl. Phys. Lett.* 2013, 103, 141903.
- [133] S. Park, Y. Horibe, T. Asada, L. S. Wielunski, N. Lee, P. L. Bonanno, S. M. O'Malley, A. A. Sirenko, A. Kazimirov, M. Tanimura, T. Gustafsson, S. W. Cheong, *Nano Lett.* 2008, 8, 720.
- [134] C. L. Zhang, S. Yeo, Y. Horibe, Y. J. Choi, S. Guha, M. Croft, S. W. Cheong, S. Mori, *Appl. Phys. Lett.* 2007, 90, 133123.
- [135] B. S. Gupton, P. K. Davies, *Nat. Mater.* 2007, 6, 586.
- [136] C. L. Zhang, C. M. Tseng, C. H. Chen, S. Yeo, Y. J. Choi, S. W. Cheong, *Appl. Phys. Lett.* 2007, 91, 233110.
- [137] Y. Ni, W. F. Rao, A. G. Khachatryan, *Nano Lett.* 2009, 9, 3275.
- [138] Y. Ni, A. G. Khachatryan, *Nat. Mater.* 2009, 8, 410.
- [139] N. Ghafoor, L. J. S. Johnson, D. O. Klenov, J. Demeulemeester, P. Desjardins, I. Petrov, L. Hultman, M. Oden, *APL Mater.* 2013, 1, 022105.
- [140] L. Mohaddes-Ardabili, H. Zheng, S. B. Ogale, B. Hannoyer, W. Tian, J. Wang, S. E. Lofland, S. R. Shinde, T. Zhao, Y. Jia, L. Salamanca-Riba, D. G. Schlom, M. Wuttig, R. Ramesh, *Nat. Mater.* 2004, 3, 533.
- [141] Y. Roussigne, S. M. Cherif, A. A. Stashkevich, F. Vidal, Y. Zheng, *J. Appl. Phys.* 2015, 118, 233903.
- [142] J. J. Huang, L. G. Li, P. Lu, Z. M. Qi, X. Sun, X. H. Zhang, H. Y. Wang, *Nanoscale* 2017, 9, 7970.
- [143] F. J. Bonilla, A. Novikova, F. Vidal, Y. L. Zheng, E. Fonda, D. Demaille, V. Schuler, A. Coati, A. Vlad, Y. Garreau, M. S. Simkin, Y. Dumont, S. Hidki, V. Etgens, *Acs Nano* 2013, 7, 4022.
- [144] Q. Su, W. R. Zhang, P. Lu, S. M. Fang, F. Khatkhatay, J. Jian, L. G. Li, F. L. Chen, X. H. Zhang, J. L. MacManus-Driscoll, A. P. Chen, Q. X. Jia, H. Y. Wang, *ACS Appl. Mater. Interfaces* 2016, 8, 20283.
- [145] V. Schuler, J. Milano, A. Coati, A. Vlad, M. Sauvage-Simkin, Y. Garreau, D. Demaille, S. Hidki, A. Novikova, E. Fonda, Y. Zheng, F. Vidal, *Nanotechnology* 2016, 27, 495601.
- [146] H. Zheng, J. Wang, L. Mohaddes-Ardabili, M. Wuttig, L. Salamanca-Riba, D. G. Schlom, R. Ramesh, *Appl. Phys. Lett.* 2004, 85, 2035.
- [147] H. Zheng, F. Straub, Q. Zhan, P. L. Yang, W. K. Hsieh, F. Zavaliche, Y. H. Chu, U. Dahmen, R. Ramesh, *Adv. Mater.* 2006, 18, 2747.
- [148] J. J. Shi, J. Z. Wu, *J. Appl. Phys.* 2015, 118, 164301.

- [149] R. Comes, H. X. Liu, M. Kholchov, R. Kasica, J. W. Lu, S. A. Wolf, *Nano Lett.* 2012, 12, 2367.
- [150] C. Schmitz-Antoniak, D. Schmitz, P. Borisov, F. M. F. de Groot, S. Stienen, A. Warland, B. Krumme, R. Feyherm, E. Dudzik, W. Kleemann, H. Wende, *Nat. Commun.* 2013, 4, 2051.
- [151] D. H. Kim, X. Y. Sun, N. M. Aimon, J. J. Kim, M. J. Campion, H. L. Tuller, L. Kornblum, F. J. Walker, C. H. Ahn, C. A. Ross, *Adv. Funct. Mater.* 2015, 25, 3091.
- [152] K. Okada, H. Tanaka, *J. Appl. Phys.* 2013, 113, 064317.
- [153] Q. G. Yan, Y. L. Jia, X. H. Li, Z. J. Liu, X. H. Dai, L. X. Ma, X. Y. Zhang, B. T. Liu, *Phys. Status Solidi A* 2014, 211, 1184.
- [154] L. Monaddes-Ardabili, H. Zheng, Q. Zhan, S. Y. Yang, R. Ramesh, L. Salamanca-Riba, M. Wuttig, S. B. Ogale, X. Pan, *Appl. Phys. Lett.* 2005, 87, 203110.
- [155] S. Kawasaki, R. Takahashi, T. Yamamoto, M. Kobayashi, H. Kumigashira, J. Yoshinobu, F. Komori, A. Kudo, M. Lippmaa, *Nat. Commun.* 2016, 7, 11818.
- [156] N. Aimon, H. K. Choi, X. Y. Sun, D. H. Kim, C. A. Ross, *Adv. Mater.* 2014, 26, 3063.
- [157] S. M. Stratulat, X. L. Lu, A. Morelli, D. Hesse, W. Erfurth, M. Alexe, *Nano Lett.* 2013, 13, 3884.
- [158] M. Fan, B. Zhang, H. Wang, J. Jian, X. Sun, J. Huang, L. Li, X. Zhang, H. Wang, *Adv. Mater.* 2017, 29, 1606861.
- [159] D. Zhou, W. Sigle, M. Kelsch, H. U. Habermeier, P. A. van Aken, *Adv. Mater. Interfaces* 2015, 2, 1500377.
- [160] D. Zhou, W. Sigle, E. Okunishi, Y. Wang, M. Kelsch, H. U. Habermeier, P. A. van Aken, *APL Mater.* 2014, 2, 127301.
- [161] X. M. Ma, Z. L. Liao, L. Li, P. Gao, *Adv. Mater. Interfaces* 2017, 4, 1700225.
- [162] C. R. Ma, M. Liu, C. L. Chen, Y. Lin, Y. R. Li, J. S. Horwitz, J. C. Jiang, E. I. Meletis, Q. Y. Zhang, *Sci. Rep.* 2013, 3, 3092.
- [163] J. C. Jiang, Y. Lin, C. L. Chen, C. W. Chu, E. I. Meletis, *J. Appl. Phys.* 2002, 91, 3188.
- [164] Y. B. Chen, M. B. Katz, X. Q. Pan, C. M. Folkman, R. R. Das, C. B. Eom, *Appl. Phys. Lett.* 2007, 91, 031902.
- [165] Z. Y. Min, D. T. Hien, T. V. Thanh, Y. Rong, C. Ying - Hao, Z. Qian, *Adv. Mater. Interfaces* 2018, 5, 1701202.

- [166] W. R. Zhang, M. T. Li, A. P. Chen, L. G. Li, Y. Y. Zhu, Z. H. Xia, P. Lu, P. Boullay, L. J. Wu, Y. M. Zhu, J. L. MacManus-Driscoll, Q. X. Jia, H. H. Zhou, J. Narayan, X. H. Zhang, H. Y. Wang, *ACS Appl. Mater. Interfaces* 2016, 8, 16845.
- [167] A. P. Chen, H. Zhou, Y. Zhu, L. Li, W. Zhang, J. Narayan, H. Y. Wang, Q. X. Jia, *J. Mater. Res.* 2016, 31, 3530.
- [168] L. Li, P. Boullay, P. Lu, X. Wang, J. Jian, J. Huang, X. Gao, S. Misra, W. Zhang, O. Perez, G. Steciuk, A. Chen, X. Zhang, H. Wang, *Nano Lett.* 2017, 17, 6575.
- [169] B. Cui, C. Song, G. Y. Wang, H. J. Mao, F. Zeng, F. Pan, *Sci. Rep.* 2013, 3, 2542
- [170] H. Yang, H. Wang, B. Maiorov, J. Lee, D. Talbayev, M. J. Hinton, D. M. Feldmann, J. L. MacManus-Driscoll, A. J. Taylor, L. Civale, T. R. Lemberger, Q. X. Jia, *J. Appl. Phys.* 2009, 106, 093914.
- [171] W. W. Li, L. Y. Wang, R. Zhao, R. J. Tang, Y. Liang, H. Yang, *J. Appl. Phys.* 2014, 116, 183904.
- [172] H. Zhou, M. F. Chisholm, T. H. Yang, S. J. Pennycook, J. Narayan, *J. Appl. Phys.* 2011, 110, 073515.
- [173] W. R. Zhang, L. G. Li, P. Lu, M. Fan, Q. Su, F. Khatkhatay, A. P. Chen, Q. X. Jia, X. H. Zhang, J. L. MacManus-Driscoll, H. Y. Wang, *ACS Appl. Mater. Interfaces* 2015, 7, 21646.
- [174] P. Lu, E. Romero, S. Lee, J. L. MacManus-Driscoll, Q. X. Jia, *Microsc. Microanal.* 2014, 20, 1782.
- [175] E. Enriquez, A. P. Chen, Z. Harrell, X. J. Lu, P. Dowden, N. Koskelo, M. Janoschek, C. L. Chen, Q. X. Jia, *Appl. Phys. Lett.* 2016, 109, 141906.
- [176] H. N. Lee, S. S. A. Seo, W. S. Choi, C. M. Rouleau, *Sci. Rep.* 2016, 6, 19941.
- [177] M. Golalikhani, Q. Y. Lei, G. Chen, J. E. Spanier, H. Ghassemi, C. L. Johnson, M. L. Taheri, X. X. Xi, *J. Appl. Phys.* 2013, 114, 027008.
- [178] U. Aschauer, R. Pfenninger, S. M. Selbach, T. Grande, N. A. Spaldin, *Phys. Rev. B* 2013, 88, 054111.
- [179] E. J. Guo, Y. Liu, C. Sohn, R. D. Desautels, A. Herklotz, Z. Liao, J. Nichols, J. W. Freeland, M. R. Fitzsimmons, H. N. Lee, *Adv. Mater.* 2018, 30, 1705904.
- [180] H. Jeon, W. S. Choi, M. D. Biegalski, C. M. Folkman, I. C. Tung, D. D. Fong, J. W. Freeland, D. Shin, H. Ohta, M. F. Chisholm, H. N. Lee, *Nat. Mater.* 2013, 12, 1057.
- [181] J. R. Petrie, H. Jeon, S. C. Barron, T. L. Meyer, H. N. Lee, *J Am Chem Soc* 2016, 138, 7252.

- [182] J. R. Petrie, C. Mitra, H. Jeon, W. S. Choi, T. Meyer, L. , F. A. Reboredo, J. W. Freeland, G. Eres, H. N. Lee, *Adv. Funct. Mater.* 2016, 26, 1564.
- [183] N. Lu, P. Zhang, Q. Zhang, R. Qiao, Q. He, H.-B. Li, Y. Wang, J. Guo, D. Zhang, Z. Duan, Z. Li, M. Wang, S. Yang, M. Yan, E. Arenholz, S. Zhou, W. Yang, L. Gu, C.-W. Nan, J. Wu, Y. Tokura, P. Yu, *Nature* 2017, 546, 124.
- [184] H.-B. Li, N. Lu, Q. Zhang, Y. Wang, D. Feng, T. Chen, S. Yang, Z. Duan, Z. Li, Y. Shi, W. Wang, W.-H. Wang, K. Jin, H. Liu, J. Ma, L. Gu, C. Nan, P. Yu, *Nat. Commun.* 2017, 8, 2156.
- [185] J. Walter, G. Yu, B. Yu, A. Grutter, B. Kirby, J. Borchers, Z. Zhang, H. Zhou, T. Birol, M. Greven, *Phys. Rev. Mater.* 2017, 1, 071403.
- [186] J. Jeong, N. Aetukuri, T. Graf, T. D. Schladt, M. G. Samant, S. S. Parkin, *Science* 2013, 339, 1402.
- [187] J. T. Ye, S. Inoue, K. Kobayashi, Y. Kasahara, H. T. Yuan, H. Shimotani, Y. Iwasa, *Nat. Mater.* 2009, 9, 125.
- [188] H. T. Yi, B. Gao, W. Xie, S.-W. Cheong, V. Podzorov, *Sci. Rep.* 2014, 4, 6604.
- [189] U. Bauer, L. Yao, A. J. Tan, P. Agrawal, S. Emori, H. L. Tuller, S. van Dijken, G. S. D. Beach, *Nat. Mater.* 2014, 14, 174.
- [190] A. L. Kruck, S. J. May, *APL Mater.* 2017, 5, 042504.
- [191] P. S. I. P. N. de Silva, F. M. Richards, L. F. Cohen, J. A. Alonso, M. J. Martinez-Lope, M. T. Casais, K. A. Thomas, J. L. MacManus-Driscoll, *J. Appl. Phys.* 1998, 83, 394.
- [192] I. Marozau, P. T. Das, M. Dobeli, J. G. Storey, M. A. Uribe-Laverde, S. Das, C. N. Wang, M. Rossle, C. Bernhard, *Phys. Rev. B* 2014, 89, 174422.
- [193] W. S. Choi, Z. Marton, S. Y. Jang, S. J. Moon, B. C. Jeon, J. H. Shin, S. S. A. Seo, T. W. Noh, K. Myung-Whun, H. N. Lee, Y. S. Lee, *J. Phys. D-Appl. Phys.* 2009, 42, 165401.
- [194] C. Aruta, M. Angeloni, G. Balestrino, N. G. Boggio, P. G. Medaglia, A. Tebano, B. Davidson, M. Baldini, D. Di Castro, P. Postorino, P. Dore, A. Sidorenko, G. Allodi, R. De Renzi, *J. Appl. Phys.* 2006, 100, 023910.
- [195] P. Carcia, A. Meinhaldt, A. Suna, *Appl. Phys. Lett.* 1985, 47, 178.
- [196] Y. Suzuki, G. Hu, R. B. van Dover, R. J. Cava, *J. Magn. Magn. Mater.* 1999, 191, 1.
- [197] A. Encinas-Oropesa, M. Demand, L. Piraux, I. Huynen, U. Ebels, *Phys. Rev. B* 2001, 63, 104415.
- [198] A. P. Chen, N. Poudyal, J. Xiong, J. P. Liu, Q. X. Jia, *Appl. Phys. Lett.* 2015, 106, 111907.

- [199] Z. G. Wang, Y. D. Yang, R. Viswan, J. F. Li, D. Viehland, *Appl. Phys. Lett.* 2011, 99, 043110.
- [200] D. H. Kim, N. M. Aimon, C. A. Ross, *APL Mater.* 2014, 2, 081101.
- [201] R. Comes, M. Khokhlov, H. X. Liu, J. W. Lu, S. A. Wolf, *J. Appl. Phys.* 2012, 111, 07D914.
- [202] N. Dix, R. Muralidharan, J. M. Rebled, S. Estrade, F. Peiro, M. Varela, J. Fontcuberta, F. Sanchez, *Acs Nano* 2010, 4, 4955.
- [203] S. P. Crane, C. Bihler, M. S. Brandt, S. T. B. Goennenwein, M. Gajek, R. Ramesh, *J. Magn. Magn. Mater.* 2009, 321, L5.
- [204] W. R. Zhang, J. Jian, A. P. Chen, L. Jiao, F. Khatkhatay, L. Li, F. Chu, Q. X. Jia, J. L. MacManus-Driscoll, *Appl. Phys. Lett.* 2014, 104, 062402.
- [205] N. D. Mathur, G. Burnell, S. P. Isaac, T. J. Jackson, B. S. Teo, J. L. MacManusDriscoll, L. F. Cohen, J. E. Evetts, M. G. Blamire, *Nature* 1997, 387, 266.
- [206] P. Schiffer, A. P. Ramirez, W. Bao, S. W. Cheong, *Phys. Rev. Lett.* 1995, 75, 3336.
- [207] J. Zhang, W.-J. Ji, J. Xu, X.-Y. Geng, J. Zhou, Z.-B. Gu, S.-H. Yao, S.-T. Zhang, *Sci. Adv.* 2017, 3, e1701473.
- [208] M. Fan, W. R. Zhang, F. Khatkhatay, L. G. Li, H. Y. Wang, *J. Appl. Phys.* 2015, 118, 065302.
- [209] X. K. Ning, Z. J. Wang, Z. D. Zhang, *Adv. Funct. Mater.* 2014, 24, 5393.
- [210] H. J. Liu, V. T. Tra, Y. J. Chen, R. Huang, C. G. Duan, Y. H. Hsieh, H. J. Lin, J. Y. Lin, C. T. Chen, Y. Ikuhara, Y. H. Chu, *Adv. Mater.* 2013, 25, 4753.
- [211] Z. X. Bi, E. Weal, H. M. Luo, A. P. Chen, J. L. MacManus-Driscoll, Q. X. Jia, H. Y. Wang, *J. Appl. Phys.* 2011, 109, 054302.
- [212] J. C. Yang, Q. He, Y. M. Zhu, J. C. Lin, H. J. Liu, Y. H. Hsieh, P. C. Wu, Y. L. Chen, S. F. Lee, Y. Y. Chin, H. J. Lin, C. T. Chen, Q. Zhan, E. Arenholz, Y. H. Chu, *Nano Lett.* 2014, 14, 6073.
- [213] H. S. Wang, Q. Li, *Appl. Phys. Lett.* 1998, 73, 2360.
- [214] J. Yang, J. Colen, J. Liu, M. C. Nguyen, G.-w. Chern, D. Louca, *Sci. Adv.* 2017, 3, eaao4949.
- [215] H. S. Wang, Q. Li, K. Liu, C. L. Chien, *Appl. Phys. Lett.* 1999, 74, 2212.
- [216] S. A. Koster, V. Moshnyaga, K. Samwer, O. I. Lebedev, G. van Tendeloo, O. Shapoval, A. Belenchuk, *Appl. Phys. Lett.* 2002, 81, 1648.
- [217] P. Agrawal, J. Guo, P. Yu, C. Hebert, D. Passerone, R. Erni, M. D. Rossell, *Phys. Rev. B* 2016, 94, 104101.

- [218] F. Khatkhatay, A. P. Chen, J. H. Lee, W. R. Zhang, H. Abdel-Raziq, H. Y. Wang, *ACS Appl. Mater. Interfaces* 2013, 5, 12541.
- [219] A. L. Sangle, O. J. Lee, A. Kursumovic, W. Zhang, A. Chen, H. Wang, J. L. MacManus-Driscoll, *Nanoscale* 2018, 10, 3460.
- [220] O. Lee, S. A. Harrington, A. Kursumovic, E. Defay, H. Y. Wang, Z. X. Bi, C. F. Tsai, L. Yan, Q. X. Jia, J. L. MacManus-Driscoll, *Nano Lett.* 2012, 12, 4311.
- [221] S. R. Foltyn, L. Civale, J. L. MacManus-Driscoll, Q. X. Jia, B. Maiorov, H. Wang, M. Maley, *Nat. Mater.* 2007, 6, 631.
- [222] P. Mele, K. Matsumoto, T. Horide, A. Ichinose, M. Mukaida, Y. Yoshida, S. Horii, R. Kita, *Supercond. Sci. Tech.* 2008, 21, 032002.
- [223] A. Xu, V. Braccini, J. Jaroszynski, Y. Xin, D. C. Larbalestier, *Phys. Rev. B* 2012, 86, 115416.
- [224] S. Awaji, Y. Yoshida, T. Suzuki, K. Watanabe, K. Hikawa, Y. Ichino, T. Izumi, *Appl. Phys. Express* 2015, 8, 023101.
- [225] T. Puig, J. Gutierrez, A. Pomar, A. Llordes, J. Gazquez, S. Ricart, F. Sandiumenge, X. Obradors, *Supercond. Sci. Tech.* 2008, 21, 034008.
- [226] J. P. F. Feighan, A. Kursumovic, J. L. MacManus-Driscoll, *Supercond. Sci. Tech.* 2017, 30, 123001.
- [227] A. Goyal, S. Kang, K. J. Leonard, P. M. Martin, A. A. Gapud, M. Varela, M. Paranthaman, A. O. Ijaduola, E. D. Specht, J. R. Thompson, D. K. Christen, S. J. Pennycook, F. A. List, *Supercond. Sci. Tech.* 2005, 18, 1533.
- [228] T. Haugan, P. N. Barnes, R. Wheeler, F. Meisenkothen, M. Sumption, *Nature* 2004, 430, 867.
- [229] A. Goyal, S. Kang, K. J. Leonard, P. M. Martin, A. A. Gapud, M. Varela, M. Paranthaman, A. O. Ijaduola, E. D. Specht, J. R. Thompson, D. K. Christen, S. J. Pennycook, F. A. List, *Supercond. Sci. Tech.* 2005, 18, 1533.
- [230] V. Selvamanickam, M. H. Gharahcheshmeh, A. Xu, E. Galstyan, L. Delgado, C. Cantoni, *Appl. Phys. Lett.* 2015, 106, 032601.
- [231] S. H. Wee, Y. F. Gao, Y. L. Zuev, K. L. More, J. Y. Meng, J. X. Zhong, G. M. Stocks, A. Goyal, *Adv. Funct. Mater.* 2013, 23, 1912.
- [232] N. A. Spaldin, M. Fiebig, *Science* 2005, 309, 391.
- [233] J. M. Hu, Z. Li, L. Q. Chen, C. W. Nan, *Nat. Commun.* 2011, 2, 553.

- [234] Y. H. Chu, L. W. Martin, M. B. Holcomb, M. Gajek, S. J. Han, Q. He, N. Balke, C. H. Yang, D. Lee, W. Hu, Q. Zhan, P. L. Yang, A. Fraile-Rodriguez, A. Scholl, S. X. Wang, R. Ramesh, *Nat. Mater.* 2008, 7, 478.
- [235] W. Prellier, M. P. Singh, P. Murugavel, *J. Phys.-Condens. Mat.* 2005, 17, R803.
- [236] J. Ma, J. M. Hu, Z. Li, C. W. Nan, *Adv. Mater.* 2011, 23, 1062.
- [237] C. W. Nan, M. I. Bichurin, S. X. Dong, D. Viehland, G. Srinivasan, *J. Appl. Phys.* 2008, 103, 031101.
- [238] C. A. F. Vaz, J. Hoffman, C. H. Ahn, R. Ramesh, *Adv. Mater.* 2010, 22, 2900.
- [239] L. W. Martin, S. P. Crane, Y. H. Chu, M. B. Holcomb, M. Gajek, M. Huijben, C. H. Yang, N. Balke, R. Ramesh, *J. Phys.-Condens. Mat.* 2008, 20, 434220.
- [240] F. Matsukura, Y. Tokura, H. Ohno, *Nat. Nanotechnol.* 2015, 10, 209.
- [241] S. Fusil, V. Garcia, A. Barthelemy, M. Bibes, *Annu. Rev. Mater. Res.* 2014, 44, 91.
- [242] L. W. Martin, R. Ramesh, *Acta Mater.* 2012, 60, 2449.
- [243] C. A. F. Vaz, *J. Phys.-Condens. Mat.* 2012, 24, 333201.
- [244] G. Lawes, G. Srinivasan, *J. Phys. D. Appl. Phys.* 2011, 44, 243001.
- [245] Y. J. Wang, J. F. Li, D. Viehland, *Mater. Today* 2014, 17, 269.
- [246] C. W. Nan, Q. X. Jia, *Mrs Bull* 2015, 40, 719.
- [247] C. W. Nan, G. Liu, Y. H. Lin, H. D. Chen, *Phys. Rev. Lett.* 2005, 94, 197203.
- [248] H. P. Wu, G. Z. Chai, T. Zhou, Z. Zhang, T. Kitamura, H. M. Zhou, *J. Appl. Phys.* 2014, 115, 114105.
- [249] C. A. F. Vaz, J. Hoffman, Y. Segal, J. W. Reiner, R. D. Grober, Z. Zhang, C. H. Ahn, F. J. Walker, *Phys. Rev. Lett.* 2010, 104, 127202.
- [250] T. X. Nan, Z. Y. Zhou, M. Liu, X. Yang, Y. Gao, B. A. Assaf, H. Lin, S. Velu, X. J. Wang, H. S. Luo, J. Chen, S. Akhtar, E. Hu, R. Rajiv, K. Krishnan, S. Sreedhar, D. Heiman, B. M. Howe, G. J. Brown, N. X. Sun, *Sci. Rep.* 2014, 4, 3688.
- [251] S. M. Wu, S. A. Cybart, P. Yu, M. D. Rossell, J. X. Zhang, R. Ramesh, R. C. Dynes, *Nat. Mater.* 2010, 9, 756.
- [252] J. X. Zhang, J. Y. Dai, W. Lu, H. L. W. Chan, B. Wu, D. X. Li, *J. Phys. D. Appl. Phys.* 2008, 41, 235405.

- [253] Y. S. Oh, S. Crane, H. Zheng, Y. H. Chu, R. Ramesh, K. H. Kim, *Appl. Phys. Lett.* 2010, 97, 052902.
- [254] Y. X. Li, Y. D. Yang, J. J. Yao, R. Viswan, Z. G. Wang, J. F. Li, D. Viehland, *Appl. Phys. Lett.* 2012, 101, 022905.
- [255] N. M. Aimon, D. H. Kim, X. Y. Sun, C. A. Ross, *ACS Appl. Mater. Interfaces* 2015, 7, 2263.
- [256] L. Yan, Z. P. Xing, Z. G. Wang, T. Wang, G. Y. Lei, J. F. Li, D. Viehland, *Appl. Phys. Lett.* 2009, 94, 192902.
- [257] L. Yan, Z. G. Wang, Z. P. Xing, J. F. Li, D. Viehland, *J. Appl. Phys.* 2010, 107, 064106.
- [258] Y.-H. Chu, *npj Quan. Mater.* 2017, 2, 67.
- [259] Y. Zhang, L. Shen, M. Liu, X. Li, X. Lu, L. Lu, C. Ma, C. You, A. Chen, C. Huang, L. Chen, M. Alexe, C.-L. Jia, *Acs Nano* 2017, 11, 8002.
- [260] T. Amrillah, Y. Bitla, K. Shin, T. Yang, Y.-H. Hsieh, Y.-Y. Chiou, H.-J. Liu, T. H. Do, D. Su, Y.-C. Chen, S.-U. Jen, L.-Q. Chen, K. H. Kim, J.-Y. Juang, Y.-H. Chu, *Acs Nano* 2017, 11, 6122.
- [261] M. Liu, O. Obi, J. Lou, Y. J. Chen, Z. H. Cai, S. Stoute, M. Espanol, M. Lew, X. Situ, K. S. Ziemer, V. G. Harris, N. X. Sun, *Adv. Funct. Mater.* 2009, 19, 1826.
- [262] J. Lou, M. Liu, D. Reed, Y. H. Ren, N. X. Sun, *Adv. Mater.* 2009, 21, 4711.
- [263] W. Eerenstein, M. Wiora, J. L. Prieto, J. F. Scott, N. D. Mathur, *Nat. Mater.* 2007, 6, 348.
- [264] T. Fix, E.-M. Choi, J. W. A. Robinson, S. B. Lee, A. P. Chen, B. Prasad, H. Wang, M. G. Blamire, J. L. MacManus-Driscoll, *Nano Lett.* 2013, 13, 5886.
- [265] F. Zavaliche, H. Zheng, L. Mohaddes-Ardabili, S. Y. Yang, Q. Zhan, P. Shafer, E. Reilly, R. Chopdekar, Y. Jia, P. Wright, D. G. Schlom, Y. Suzuki, R. Ramesh, *Nano Lett.* 2005, 5, 1793.
- [266] F. Zavaliche, T. Zhao, H. Zheng, F. Straub, M. P. Cruz, P. L. Yang, D. Hao, R. Ramesh, *Nano Lett.* 2007, 7, 1586.
- [267] S. H. Xie, F. Y. Ma, Y. M. Liu, J. Y. Li, *Nanoscale* 2011, 3, 3152.
- [268] Y. X. Li, Z. C. Wang, J. J. Yao, T. N. Yang, Z. G. Wang, J. M. Hu, C. L. Chen, R. Sun, Z. P. Tian, J. F. Li, L. Q. Chen, D. Viehland, *Nat. Commun.* 2015, 6, 6680.
- [269] A. P. Chen, Q. X. Jia, in *Multiferroic materials: Properties, techniques, and applications*, (Ed: J. L. Wang), Taylor & Francis Group, 2016.
- [270] H. Yang, H. Y. Wang, J. Yoon, Y. Q. Wang, M. Jain, D. M. Feldmann, P. C. Dowden, J. L. MacManus-Driscoll, Q. X. Jia, *Adv. Mater.* 2009, 21, 3969.

- [271] W. W. Li, R. Zhao, R. J. Tang, A. P. Chen, W. R. Zhang, X. Lu, H. Y. Wang, H. Yang, *ACS Appl. Mater. Interfaces* 2014, 6, 5356.
- [272] R. Zhao, W. W. Li, A. P. Chen, W. R. Zhang, J. Yang, Y. Liang, R. J. Tang, H. Y. Wang, H. Yang, *Appl. Phys. Lett.* 2014, 105, 072907.
- [273] A. Savoia, D. Paparo, P. Perna, Z. Ristic, M. Salluzzo, F. M. Granozio, U. S. di Uccio, C. Richter, S. Thiel, J. Mannhart, L. Marrucci, *Phys. Rev. B* 2009, 80, 075110.
- [274] Z. Q. Liu, W. Lu, S. W. Zeng, J. W. Deng, Z. Huang, C. J. Li, M. Motapothula, W. M. Lu, L. Sun, K. Han, J. Q. Zhong, P. Yang, N. N. Bao, W. Chen, J. S. Chen, Y. P. Feng, J. M. D. Coey, T. Venkatesan, Ariando, *Adv. Mater. Interfaces* 2014, 1, 1400155.
- [275] S. A. Chambers, M. H. Engelhard, V. Shutthanandan, Z. Zhu, T. C. Droubay, L. Qiao, P. Sushko, T. Feng, H. D. Lee, T. Gustafsson, *Surf. Sci. Rep.* 2010, 65, 317.
- [276] Y. H. Hsieh, J. M. Liou, B. C. Huang, C. W. Liang, Q. He, Q. Zhan, Y. P. Chiu, Y. C. Chen, Y. H. Chu, *Adv. Mater.* 2012, 24, 4564.
- [277] Y. H. Hsieh, E. Strelcov, J. M. Liou, C. Y. Shen, Y. C. Chen, S. V. Kalinin, Y. H. Chu, *Acs Nano* 2013, 7, 8627.
- [278] V. T. Tra, J. C. Yang, Y. H. Hsieh, J. Y. Lin, Y. C. Chen, Y. H. Chu, *Phys. Status Solidi-RRL* 2014, 8, 478.
- [279] A. A. Taskin, A. N. Lavrov, Y. Ando, *Appl. Phys. Lett.* 2005, 86, 091910.
- [280] G. Kim, S. Wang, A. J. Jacobson, L. Reimus, P. Brodersen, C. A. Mims, *J. Mater. Chem.* 2007, 17, 2500.
- [281] A. Tarancon, S. J. Skinner, R. J. Chater, F. Hernandez-Ramirez, J. A. Kilner, *J. Mater. Chem.* 2007, 17, 3175.
- [282] A. Chronos, B. Yildiz, A. Tarancon, D. Parfitt, J. A. Kilner, *Energy Environ. Sci.* 2011, 4, 2774.
- [283] M. Sillassen, P. Eklund, N. Pryds, E. Johnson, U. Helmersson, J. Bottiger, *Adv. Funct. Mater.* 2010, 20, 2071.
- [284] A. Kushima, B. Yildiz, *J. Mater. Chem.* 2010, 20, 4809.
- [285] C. Korte, A. Peters, J. Janek, D. Hesse, N. Zakharov, *Phys. Chem. Chem. Phys.* 2008, 10, 4623.
- [286] S. Azad, O. A. Marina, C. M. Wang, L. Saraf, V. Shutthanandan, D. E. McCready, A. El-Azab, J. E. Jaffe, M. H. Engelhard, C. H. F. Peden, S. Thevuthasan, *Appl. Phys. Lett.* 2005, 86, 131906.

- [287] Q. Su, D. Yoon, A. P. Chen, F. Khatkhatay, A. Manthiram, H. Y. Wang, *J. Power Sources* 2013, 242, 455.
- [288] S. Lee, J. L. MacManus-Driscoll, *APL Mater.* 2017, 5, 072907.
- [289] S. M. Yang, S. Lee, J. Jian, W. R. Zhang, P. Lu, Q. X. Jia, H. Y. Wang, T. W. Noh, S. V. Kalinin, J. L. MacManus-Driscoll, *Nat. Commun.* 2015, 6, 8588.
- [290] S. Lee, W. R. Zhang, F. Khatkhatay, H. Y. Wang, Q. X. Jia, J. L. MacManus-Driscoll, *Nano Lett.* 2015, 15, 7362.
- [291] S. P. Jiang, *Mater. Sci. Eng., A* 2006, 418, 199.
- [292] S. B. Adler, *Chem. Rev.* 2004, 104, 4791.
- [293] Q. Su, S. Cho, Z. Bi, A. P. Chen, H. Wang, *Electrochim. Acta* 2011, 56, 3969.
- [294] Z. Shao, S. M. Haile, *Nature* 2004, 431, 170.
- [295] M. Kubicek, Z. Cai, W. Ma, B. Yildiz, H. Hutter, J. Fleig, *Acs Nano* 2013, 7, 3276.
- [296] N. Tsvetkov, Q. Lu, Y. Chen, B. Yildiz, *Acs Nano* 2015, 9, 1613.
- [297] D. Ding, X. Li, S. Y. Lai, K. Gerdes, M. Liu, *Energy Environ. Sci.* 2014, 7, 552.
- [298] G. M. Rupp, A. K. Opitz, A. Nenning, A. Limbeck, J. Fleig, *Nat. Mater.* 2017, 16, 640.
- [299] Y. M. Kim, J. He, M. D. Biegalski, H. Ambaye, V. Lauter, H. M. Christen, S. T. Pantelides, S. J. Pennycook, S. V. Kalinin, A. Y. Borisevich, *Nat. Mater.* 2012, 11, 888.
- [300] Y.-L. Lee, J. Kleis, J. Rossmeisl, Y. Shao-Horn, D. Morgan, *Energy Environ. Sci.* 2011, 4, 3966.
- [301] S. Cho, Y. N. Kim, J. Lee, A. Manthiram, H. Wang, *Electrochim. Acta* 2012, 62, 147.
- [302] W. Ma, J. J. Kim, N. Tsvetkov, T. Daio, Y. Kuru, Z. Cai, Y. Chen, K. Sasaki, H. L. Tuller, B. Yildiz, *J. Mater. Chem. A* 2015, 3, 207.
- [303] J. Yoon, S. Cho, J. H. Kim, J. Lee, Z. X. Bi, A. Serquis, X. H. Zhang, A. Manthiram, H. Y. Wang, *Adv. Funct. Mater.* 2009, 19, 3868.
- [304] Q. Su, D. Yoon, Z. Sisman, F. Khatkhatay, Q. X. Jia, A. Manthiram, H. Wang, *Int. J. Hydrogen Energy* 2013, 38, 16320.
- [305] C. Yan, C. Zhuhua, K. Yener, M. Wen, T. H. L., Y. Bilge, *Adv Energy Mater* 2013, 3, 1221.
- [306] J. W. Han, B. Yildiz, *Energy Environ. Sci.* 2012, 5, 8598.

- [307] S. Cho, J. W. Jang, L. G. Li, J. Jian, H. Y. Wang, J. L. MacManus-Driscoll, *Chem Mater* 2016, 28, 3017.
- [308] L. T. Quynh, C. N. Van, Y. Bitla, J. W. Chen, T. H. Do, W. Y. Tzeng, S. C. Liao, K. A. Tsai, Y. C. Chen, C. L. Wu, C. H. Lai, C. W. Luo, Y. J. Hsu, Y. H. Chu, *Adv Energy Mater* 2016, 6, 1600686.
- [309] T. H. Do, C. Nguyen Van, K.-A. Tsai, L. T. Quynh, J.-W. Chen, Y.-C. Lin, Y.-C. Chen, W.-C. Chou, C.-L. Wu, Y.-J. Hsu, Y.-H. Chu, *Nano Energy* 2016, 23, 153.
- [310] A. L. Sangle, S. Singh, J. Jian, S. R. Bajpe, H. Y. Wang, N. Khare, J. L. MacManus-Driscoll, *Nano Lett.* 2016, 16, 7338.
- [311] H.-J. Liu, W.-I. Liang, Y.-H. Chu, H. Zheng, R. Ramesh, *MRS Commun.* 2014, 4, 31.
- [312] L. Li, L. Sun, J. S. Gomez-Diaz, N. L. Hogan, P. Lu, F. Khatkhatay, W. Zhang, J. Jian, J. Huang, Q. Su, M. Fan, C. Jacob, J. Li, X. Zhang, Q. X. Jia, M. Sheldon, A. Alù, X. Li, H. Wang, *Nano Lett.* 2016, 16, 3936.
- [313] C. Y. Tsai, H. M. Cheng, H. R. Chen, K. F. Huang, L. N. Tsai, Y. H. Chu, C. H. Lai, W. F. Hsieh, *Appl. Phys. Lett.* 2014, 104, 252905.
- [314] H. J. Liu, L. Y. Chen, Q. He, C. W. Liang, Y. Z. Chen, Y. S. Chien, Y. H. Hsieh, S. J. Lin, E. Arenholz, C. W. Luo, Y. L. Chueh, Y. C. Chen, Y. H. Chu, *Acs Nano* 2012, 6, 6952.
- [315] J. Lloyd-Hughes, C. D. W. Mosley, S. P. P. Jones, M. R. Lees, A. Chen, Q. X. Jia, E. M. Choi, J. L. MacManus-Driscoll, *Nano Lett* 2017, 17, 2506.

Figure captions

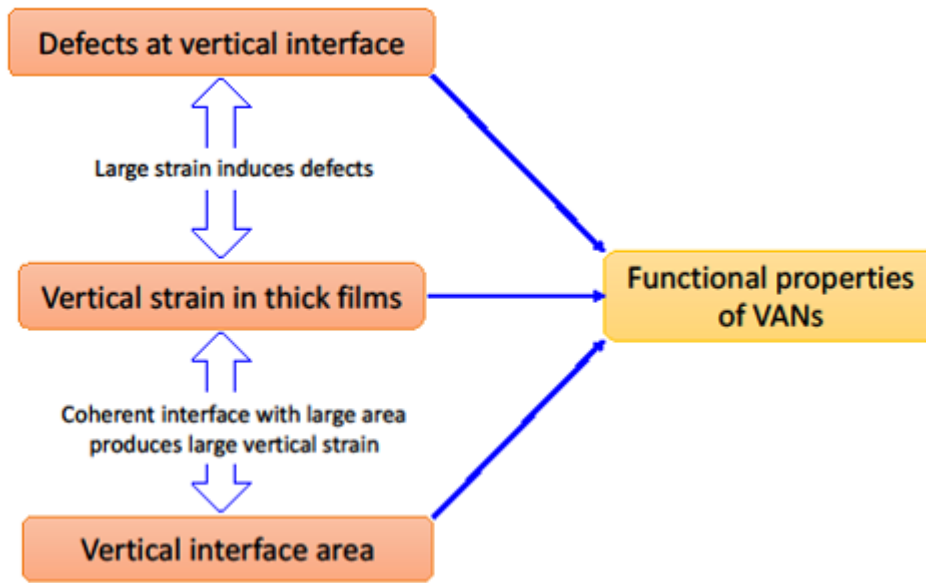


Figure 1. Three key features of VANs: strain, defect and interface along the vertical interface.

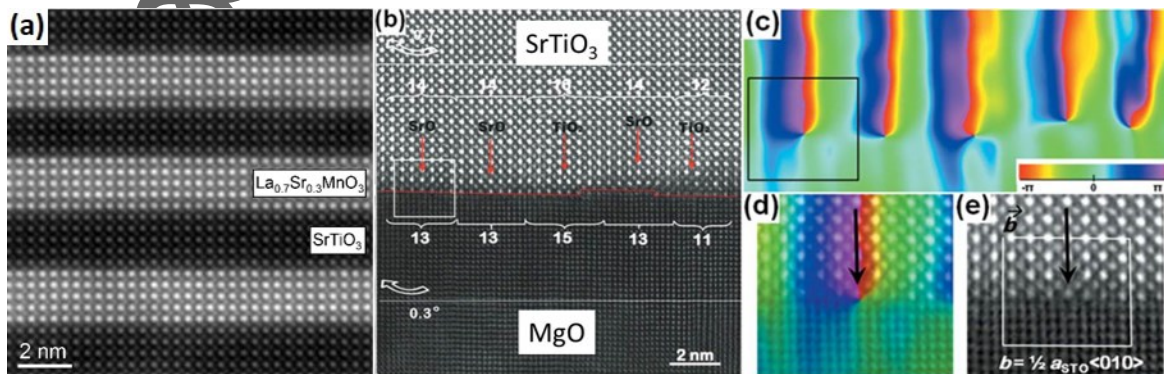


Figure 2. a) A HRSTEM image of LSMO/STO superlattices. Reproduced with permission.^[32] Copyright 2010, PNAS. b) A HRSTEM image of the STO/MgO heterostructure with five misfit dislocation cores. c) Misfit dislocations revealed by GPA. d) One misfit dislocation combined with the corresponding GPA image. The arrow shows the position of the extra-half-plane. e) A Burgers vector of $1/2 a_{\text{STO}} \langle 010 \rangle$ was found for the misfit dislocation in (d) after applying the Burgers circuit. Reproduced with permission.^[35] Copyright 2013, Microscopy Society of America.

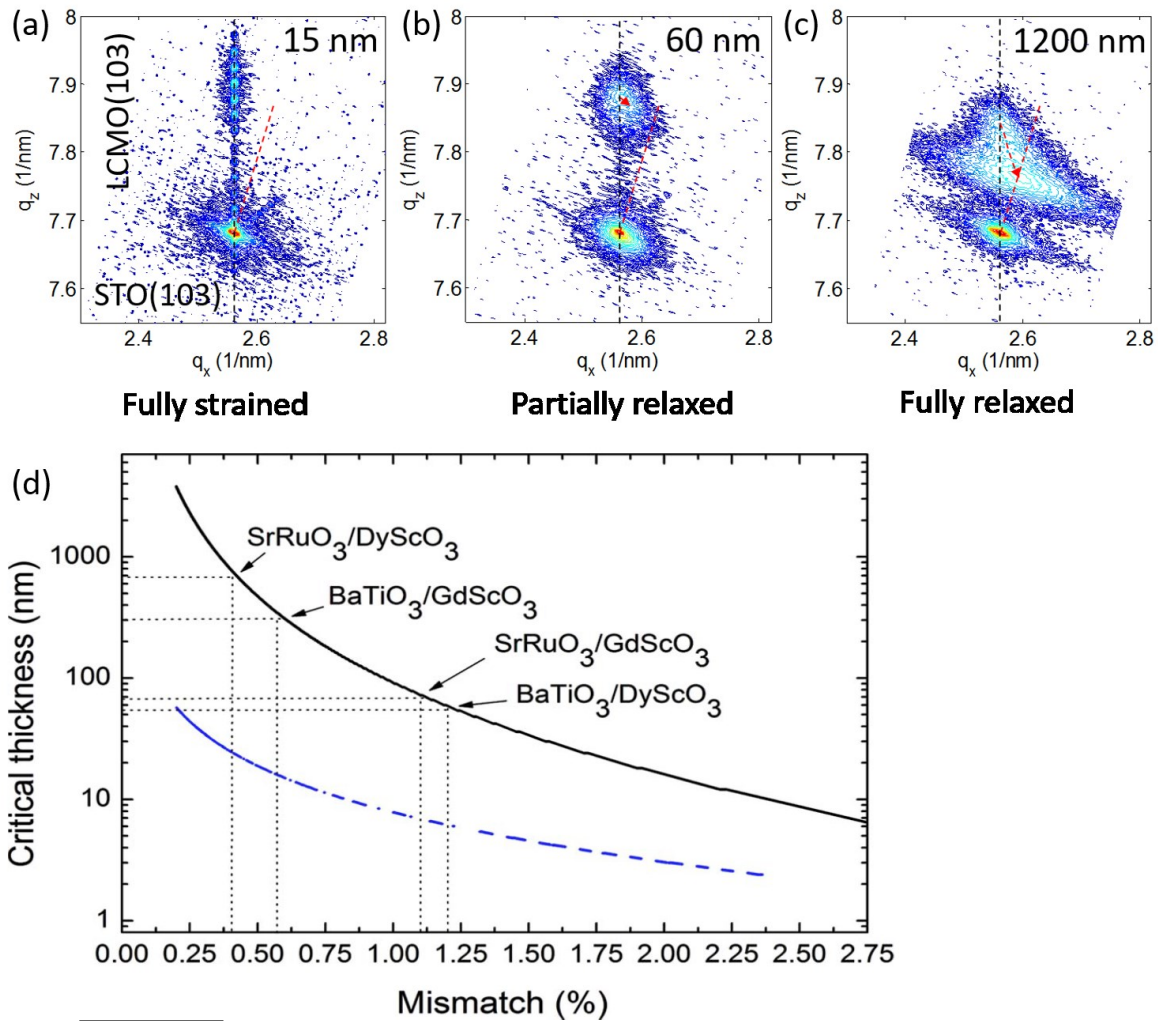


Figure 3. RSM (103) scans of $\text{La}_{0.7}\text{Ca}_{0.3}\text{MnO}_3$ films on STO (001) substrates for a) 15 nm, fully strained, b) 60 nm, partially relaxed, and c) 1200 nm, fully relaxed. d) The lattice mismatch dependent theoretical critical thickness. The black curve is estimated by using People-Bean energy balance model and the blue curve was estimated by using mechanical equilibrium model. Reproduced with permission.^[64] Copyright 2007, American Institute of Physics.

Auth

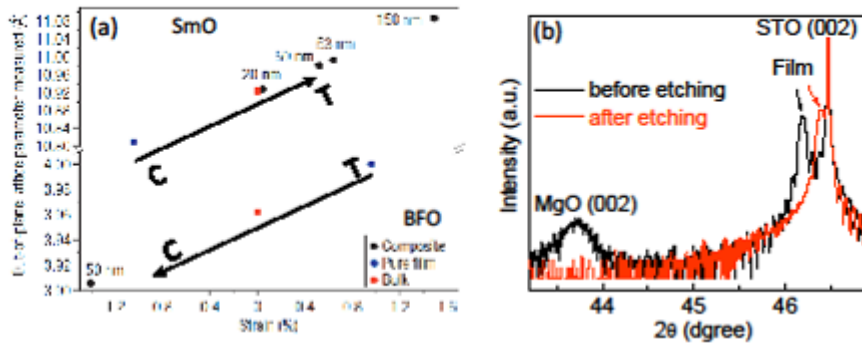


Figure 4. a) The measured out-of-plane lattice constants versus calculated out-of-plane strain (relative to the bulk lattice parameter) in nanocomposite films compared with pure film and with bulk in BFO/ Sm_2O_3 . Reproduced with permission.^[30] Copyright 2008, Nature Publishing Group. b) Local XRD θ - 2θ scans of STO:MgO VANs before and after etching off MgO.

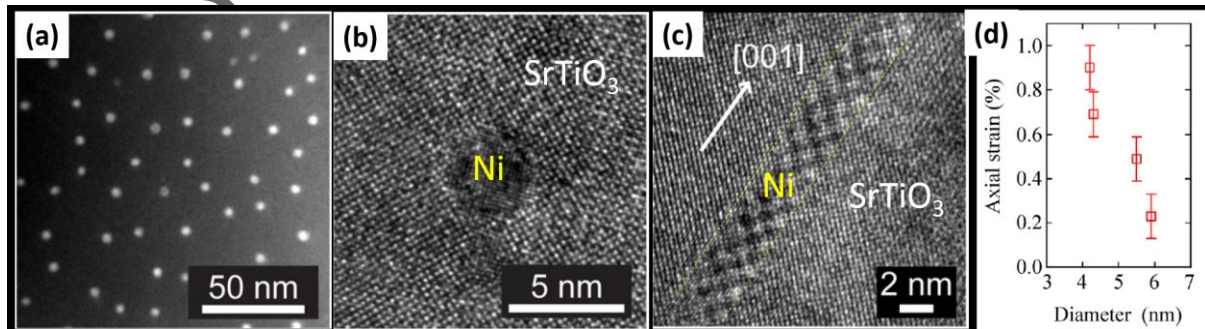


Figure 5. a) A plan-view low magnification transmission electron microscopy (TEM) image in energy filtered mode showing the growth of Ni nanopillars (3.4 ± 0.5 nm) in SrTiO₃ matrix. b) High-resolution view of a single nanopillar imaged in (a). c) High-resolution cross-sectional view of the SrTiO₃:Ni nanocomposite. d) Ni nanopillar size dependent axial strain in the Ni nanopillars. Reproduced with permission.^[107] Copyright 2015, Springer.

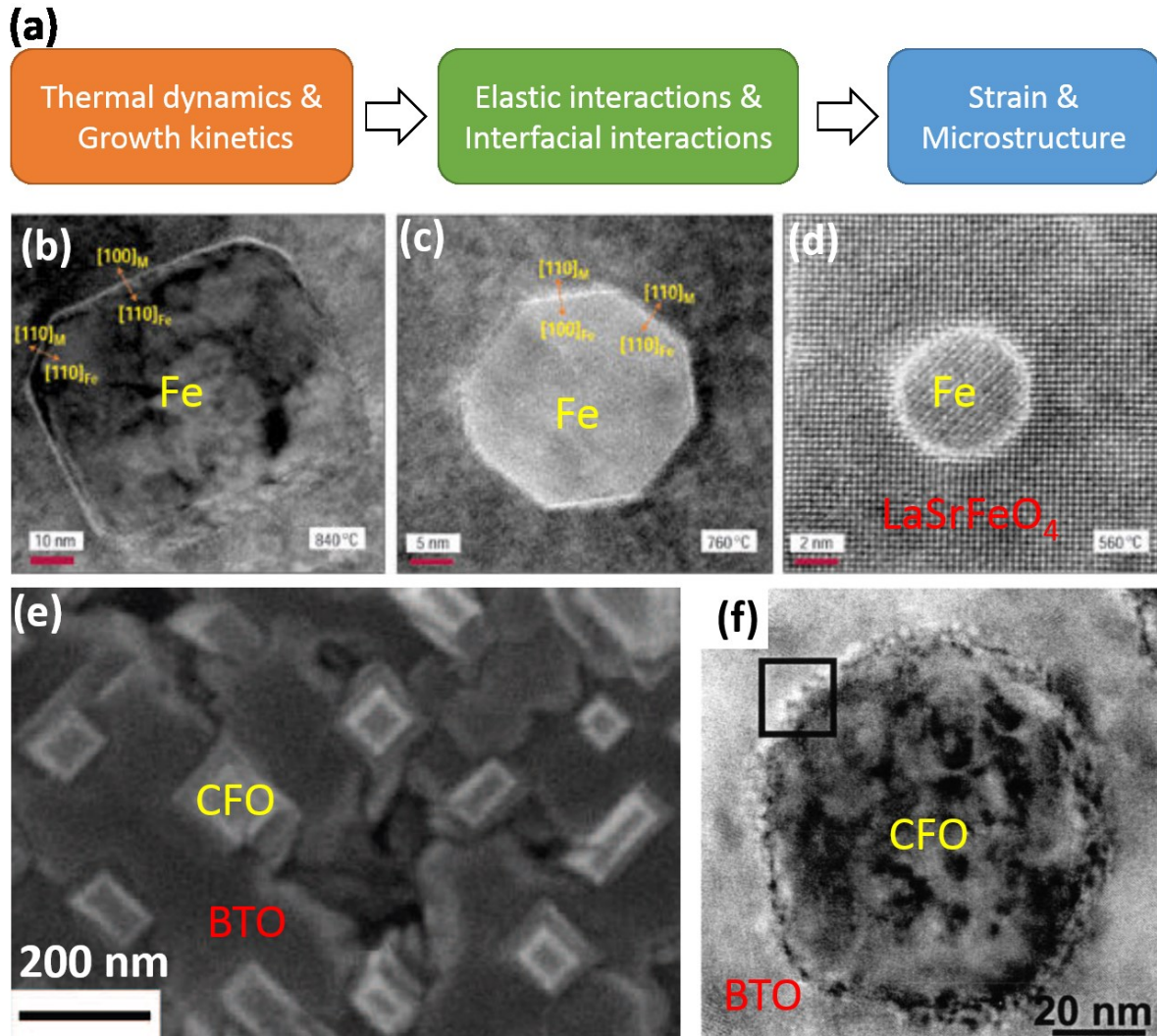


Figure 6. a) Dependence of strain and microstructure on elastic/interfacial interactions and thermodynamics/growth kinetics. b) Square-shaped ($d = 40-50$ nm) Fe nanopillars are obtained at 840 °C. c) Fe nanopillars with octagonal cross section ($d = 15-20$ nm) form at 760 °C. d) Circular Fe nanopillars form at 560 °C ($d = 4-6$ nm). Reproduced with permission.^[140] Copyright 2004, Nature Publishing Group. e) Plan-view scanning electron microscopy (SEM) image of the BTO:CFO (mol: 35%) grown at 950 °C. Reproduced with permission.^[150] Copyright 2013, Nature Publishing Group. f) Plan-view TEM image of BTO:CFO (mol: 38%) grown at 950 °C with one CFO circular pillar in BTO phase. Reproduced with permission.^[146] Copyright 2004, American Institute of Physics.

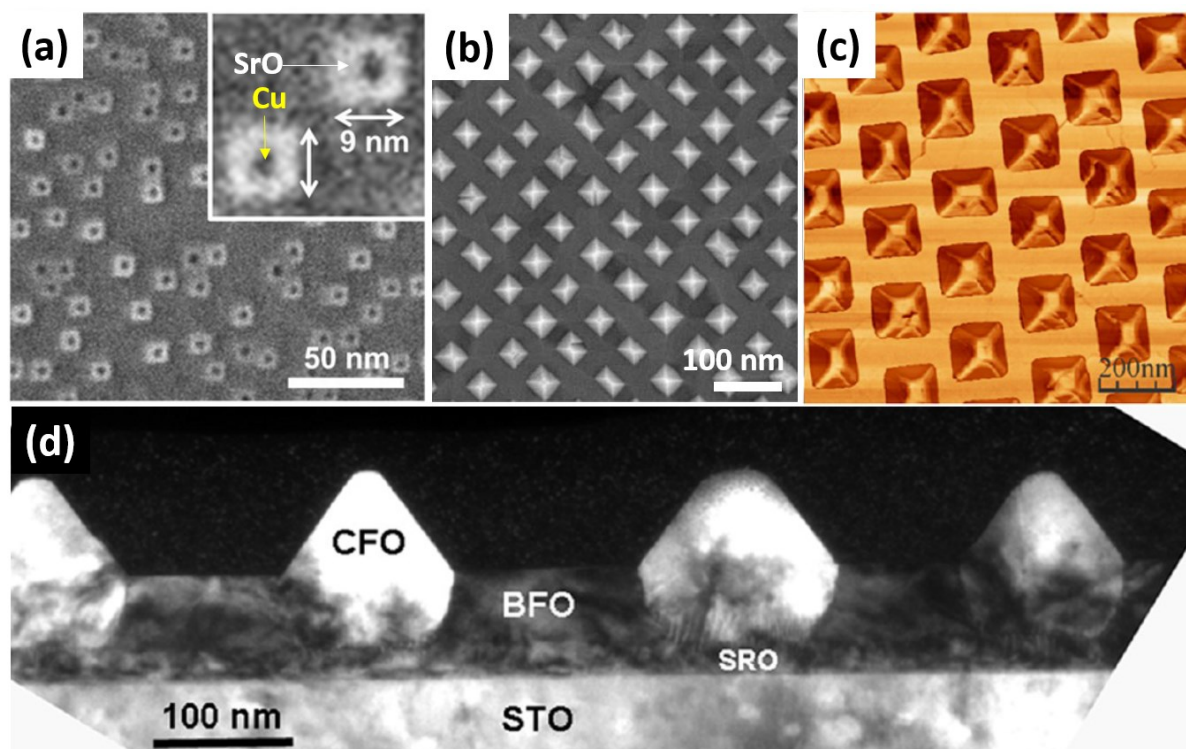


Figure 7. a) A top-view SEM image of the 30 nm $\text{Sr}(\text{Ti}, \text{Cu})\text{O}_{3.8}$ film after chemical etching. Inset shows the pores in the SrO rods after removing Cu. Reproduced with permission.^[151] Copyright 2015, Wiley. b) Square lattice of BFO/ $\text{Co}_{0.5}\text{Ni}_{0.5}\text{Fe}_2\text{O}_4$ with a period of 67 nm. Reproduced with permission.^[156] Copyright 2014, Wiley. c) Atomic force microscopy (AFM) phase image showing the perfect phase segregation of the BFO:CFO VANs. d) TEM image of the sample in (c) showing the pyramid shape of the CFO pillars. Reproduced with permission.^[157] Copyright 2013, American Chemical Society.

Author

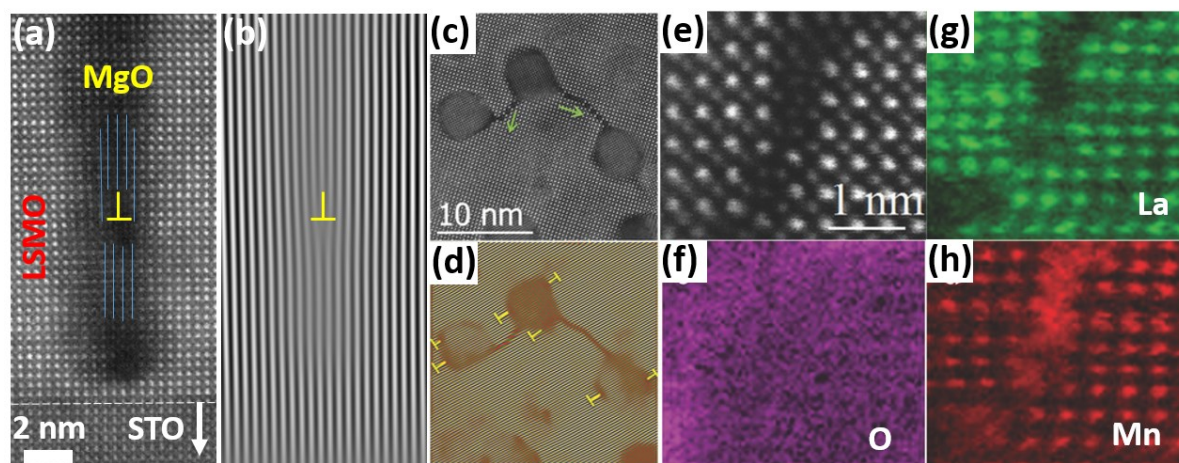


Figure 8. a) A cross-sectional HAADF-STEM image of a LSMO:MgO VAN thin film on STO (001) substrate. b) The corresponding FFT image of (a). c) A plan-view HAADF image of a LSMO:ZrO₂ (30 mol. %) VAN thin film with ZrO₂ nanopillars connected by boundaries. d) The corresponding FFT image of (c). e) A plan-view HAADF image of a LSMO:ZrO₂ VAN with 20 % of ZrO₂ in molar ratio. EELS spectrum images of f) O-K, g) La-M_{4,5}, and h) Mn-L_{2,3}. c–h) Reproduced with permission.^[159] Copyright 2017, Wiley.

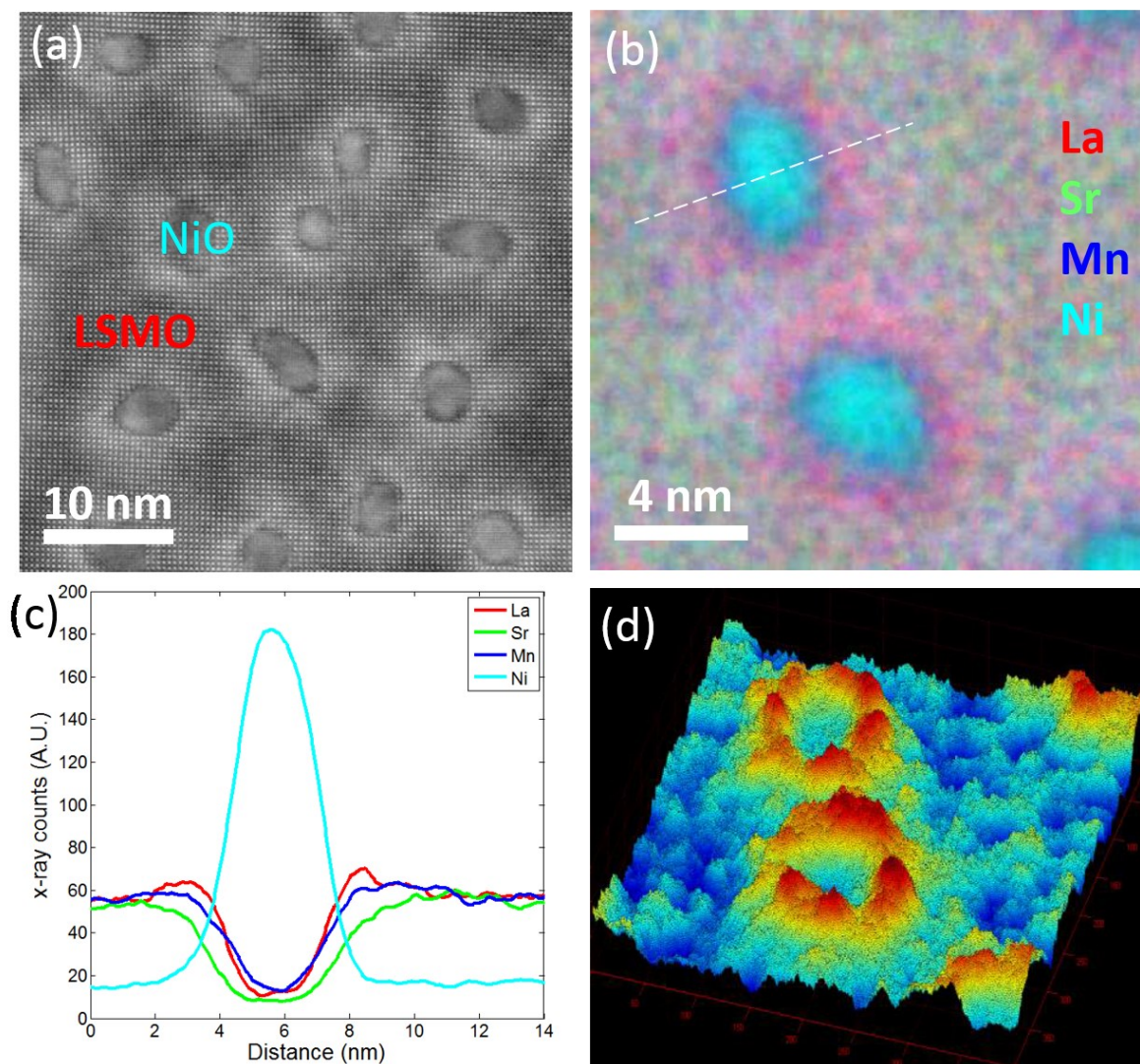


Figure 9. a) A HAADF-STEM image of a LSMO:NiO VAN thin film. b) An EDS color-map of La, Sr, Mn, and Ni elements at the local area of the VAN. c) A line-profile across the NiO nanopillar along the dashed line in (b). d) The existence of a La-rich region around NiO nanopillars. Reproduced with permission.^[17] Copyright 2015, Microscopy Society of America.

Auth

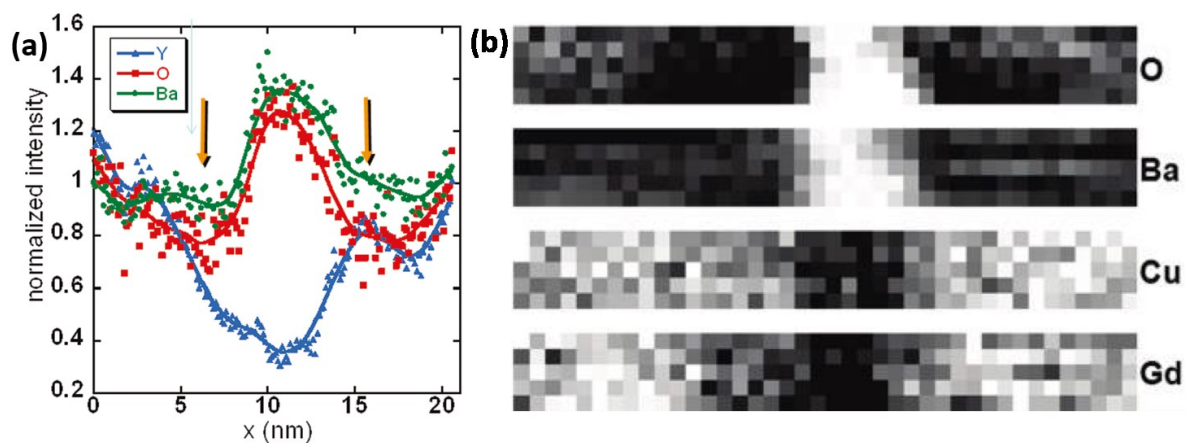


Figure 10. a) EELS analysis of elemental content across a BZO nanopillar in a REBCO matrix. The arrows point out the suppressed O signal in proximity of the BZO nanopillar. b) EELS maps of O, Ba, Cu, and Gd. Reproduced with permission.^[109] Copyright 2011, American Chemical Society.

Author Manuscript

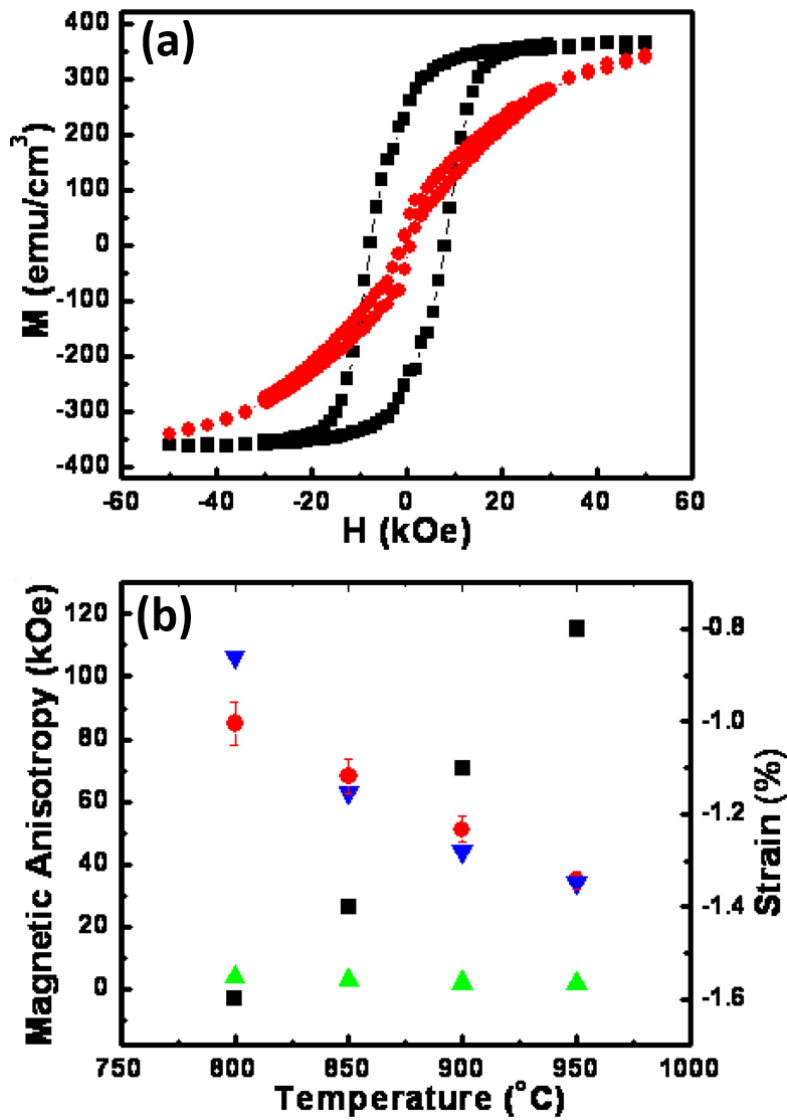


Figure 11. a) The out-of-plane (■) and in-plane (●) M - H loops of a 900 °C grown BTO:CFO VAN. b) Temperature dependent out-of-plane strain (■) and temperature dependent magnetic anisotropy (experimental data (●), stress anisotropy (▼), and shape anisotropy (▲) of VANs. Reproduced with permission.^[109] Copyright 2007, American Institute of Physics.

Author

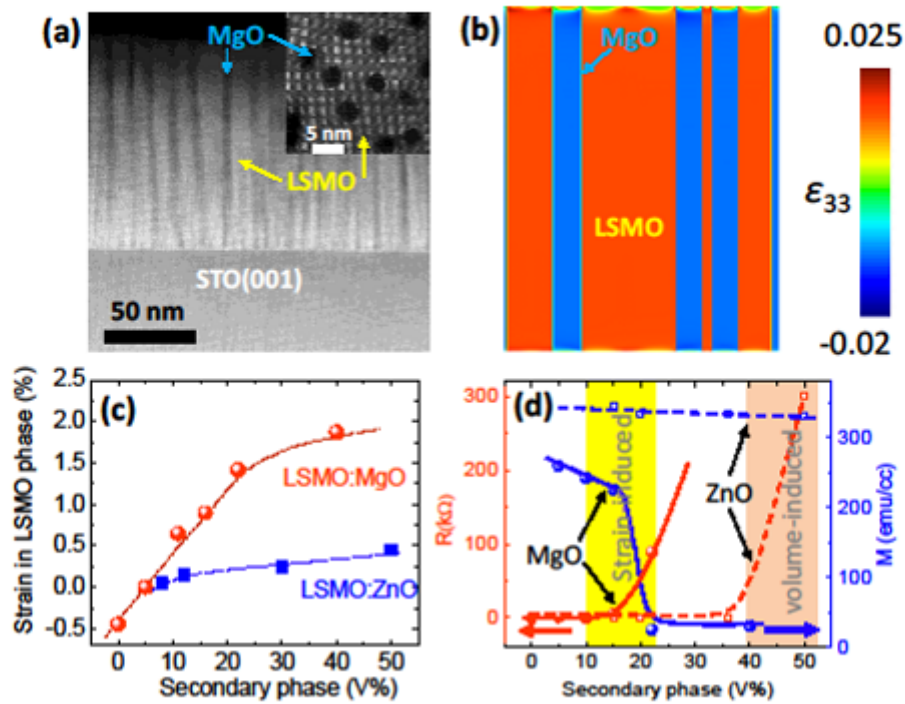


Figure 12. a) A cross-sectional STEM image of a LSMO:MgO VAN with phase separated LSMO (white) and MgO (dark) phases. Inset: A top-view STEM image of the LSMO:MgO VAN with MgO nanopillars in the LSMO matrix. The MgO volume is 22%. b) The strain distribution in the LSMO matrix and MgO nanopillars (MgO volume: 41%) calculated by phase field simulation. c) The secondary phase volume dependent vertical strain in the LSMO matrix. The red (dot) data represents the LSMO:MgO system, and the blue (square) data set represents the LSMO:ZnO system). d) The secondary phase volume dependent resistance at 100 K (red data set) and saturated magnetization (blue data set) at 20 K for the LSMO:MgO (solid curve) and LSMO:ZnO (dashed curves) VAN films. Reproduced with permission.^[95] Copyright 2016, AAAS.

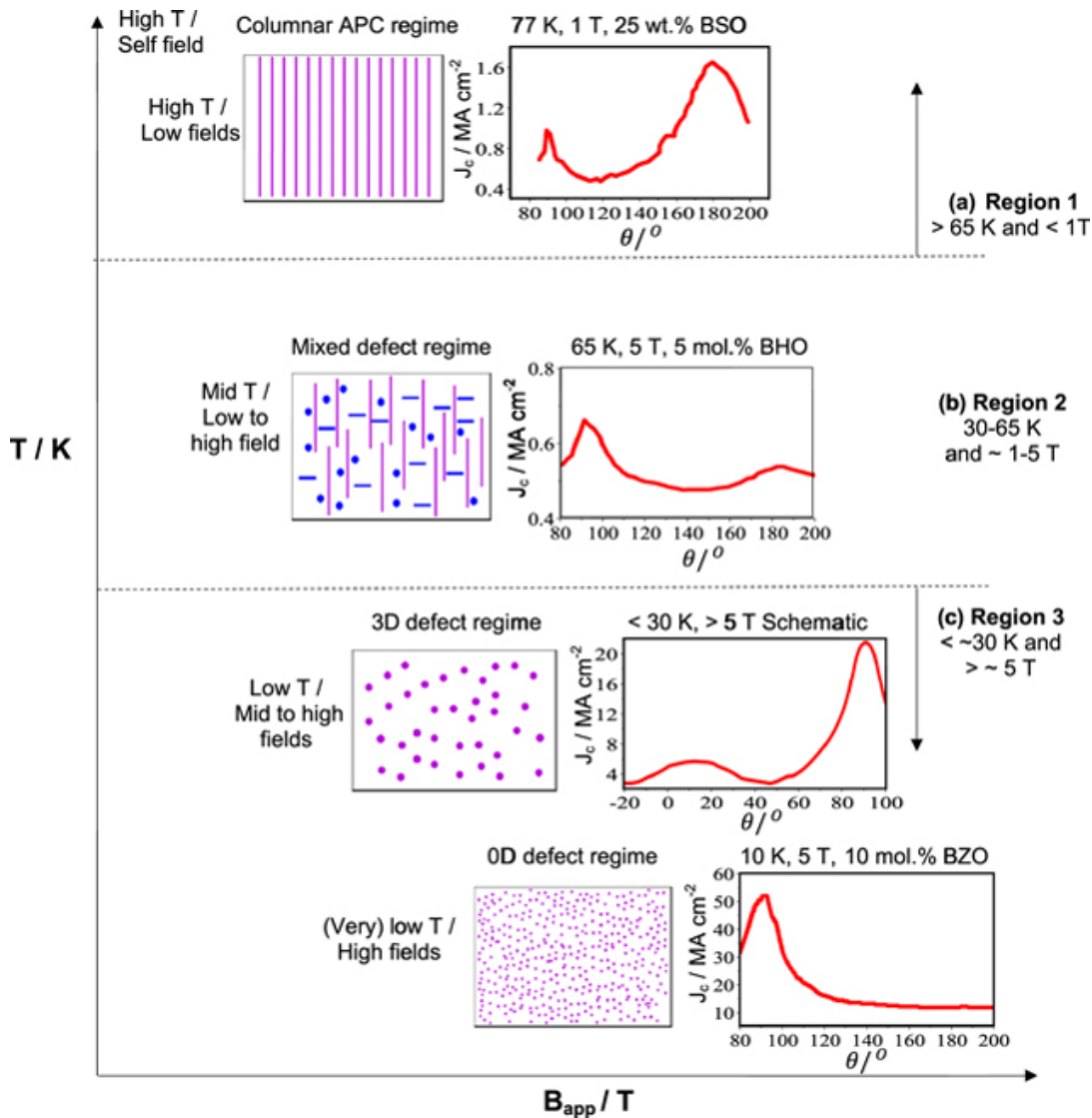


Figure 13. A schematic illustration of microstructures for doped superconducting films with corresponding $J_c - \theta$ plots. a) Region 1 shows a high-temperature/low-field regime which is induced by columnar secondary phases such as nanorods and nanowires. b) Region 2 shows a mid-temperature/mid-field regime which is induced by a mixed microstructure. c) Region 3 shows a low-temperature/high-field regime. Reproduced with permission.^[226] Copyright 2017, Institute of Physics.

Author

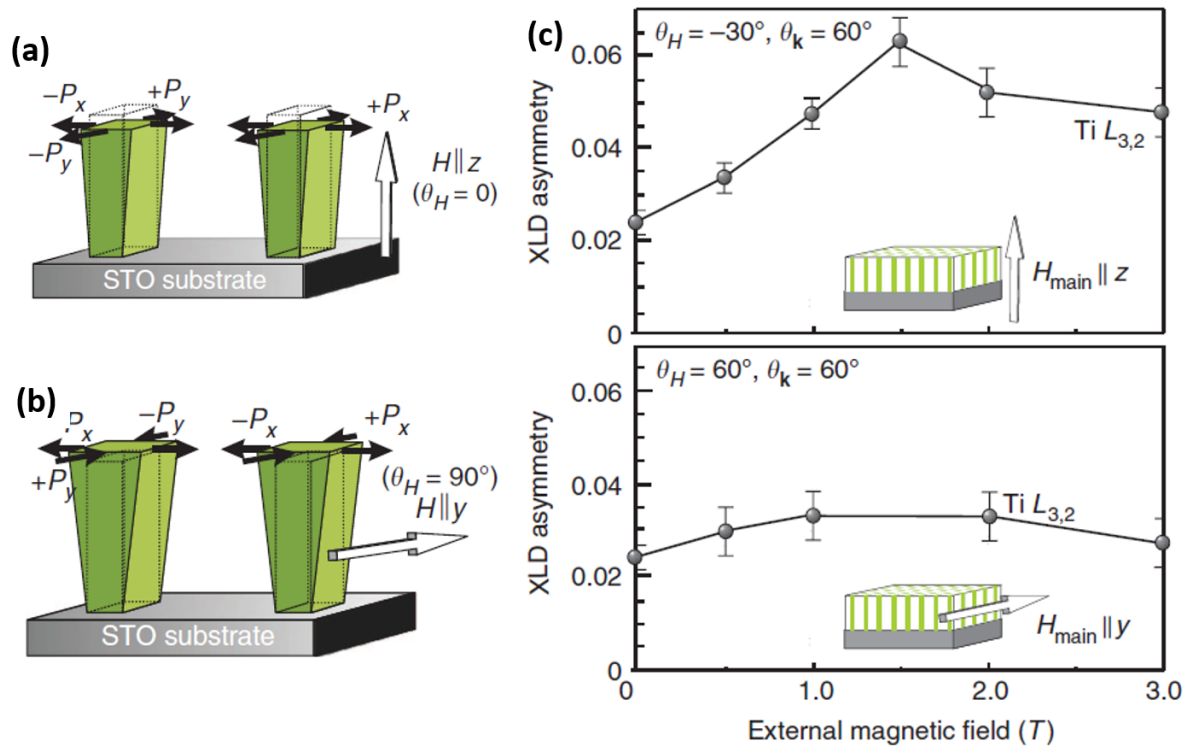


Figure 14. a,b) Illustrations of experimental setups with applying the external magnetic field along the z-axis and y-axis. c) The change of the Ti X-ray linear dichroism (XLD) by external magnetic fields. Magnetic field-dependent soft XLD (Ti $L_{3,2}$ absorption edges with H_{main} (top panel) parallel to z and (bottom panel) perpendicular to z. Reproduced with permission.^[150] Copyright 2013, Nature Publishing Group.

Author Manuscript

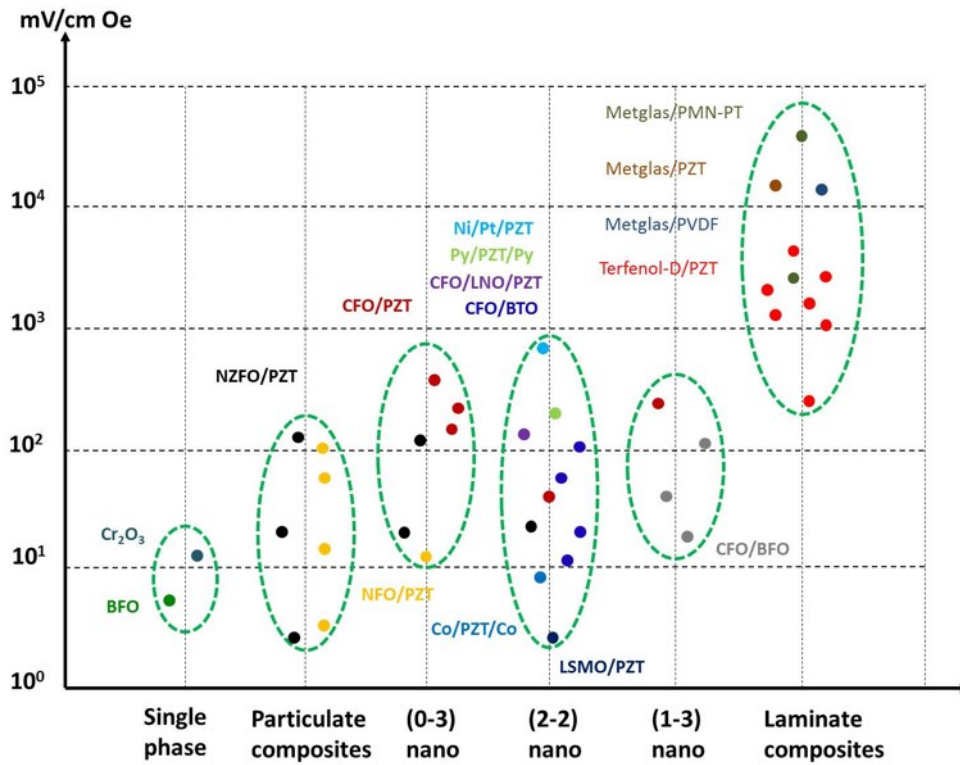


Figure 15. Comparison of ME coupling coefficients at low frequencies in different types of multiferroic materials. Reproduced with permission.^[269] Copyright 2016, Taylor & Francis Group.

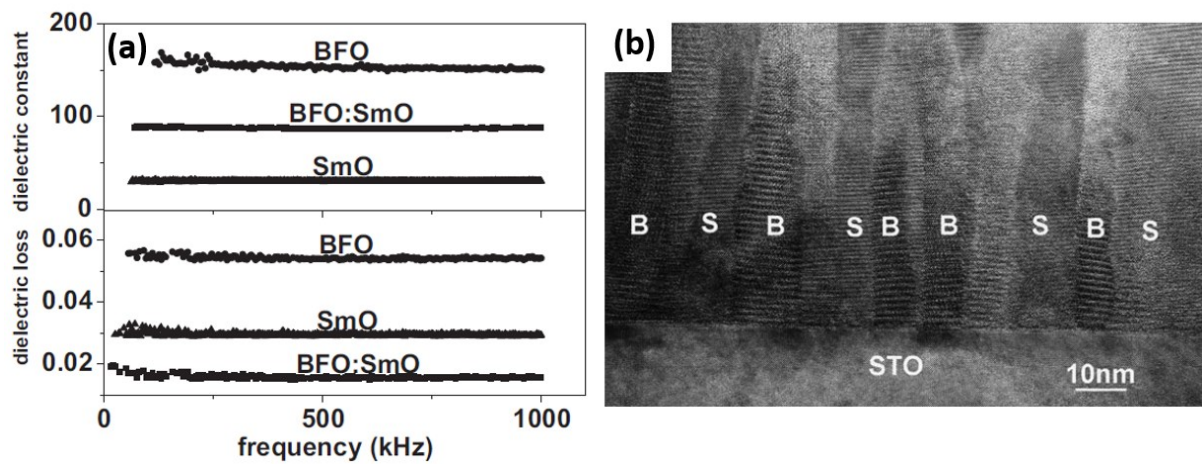


Figure 16. a) Frequency dependent dielectric constant and dielectric loss of BFO:Sm₂O₃ VAN thin films, compared to BFO and Sm₂O₃ single-phase thin films. b) A cross-sectional TEM image of a BFO:Sm₂O₃ VAN film with vertical nanocolumns of BFO and Sm₂O₃ (B represents BFO, S represents Sm₂O₃). Reproduced with permission.^[270] Copyright 2009, Wiley.

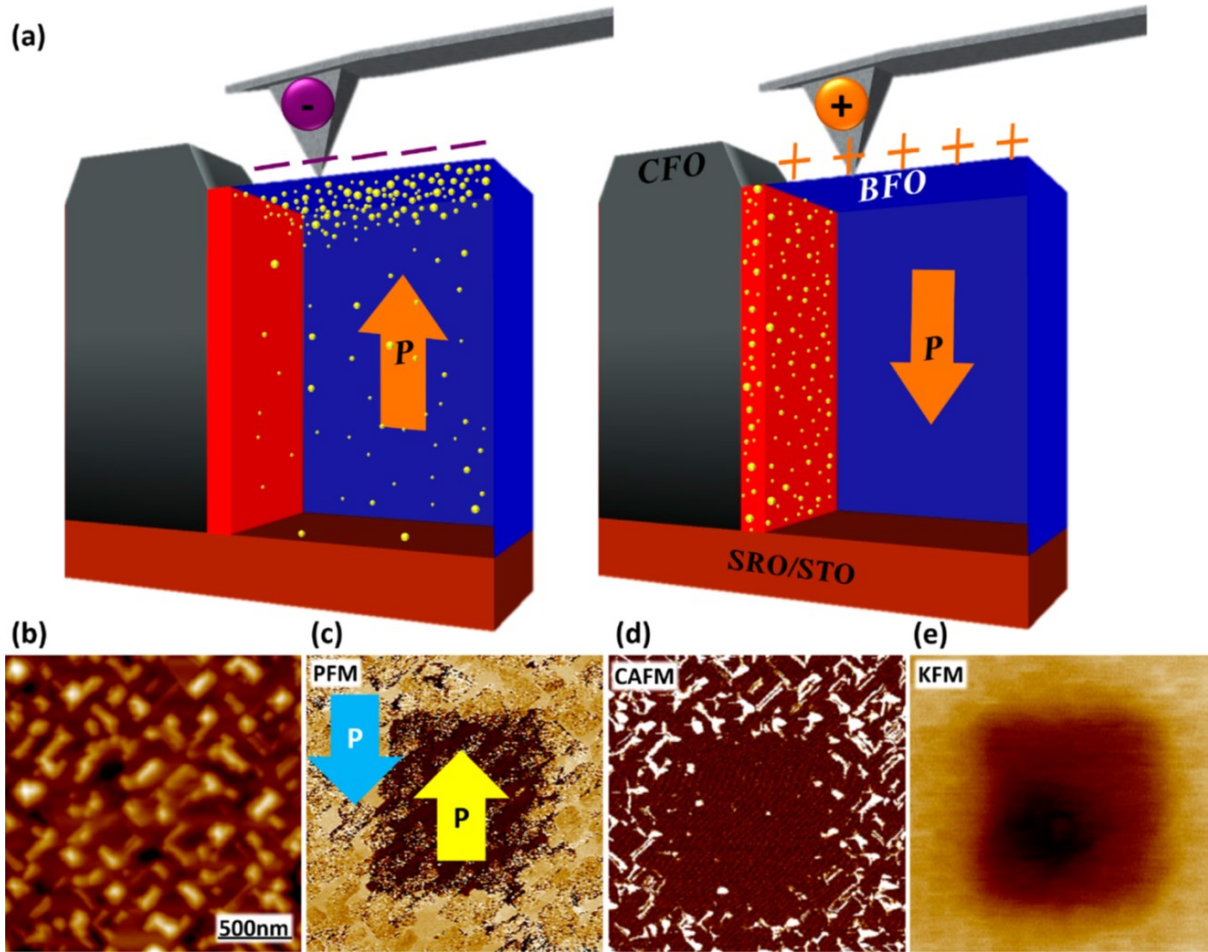


Figure 17. a) Schematic illustrations of vertical conduction controlled by polarization polarity. The top surface of a BFO:CFO VAN characterized by b) AFM, c) PFM, d) c-AFM and e) Kelvin Force Microscopy (KFM). Reproduced with permission.^[277] Copyright 2013, Wiley.

Author

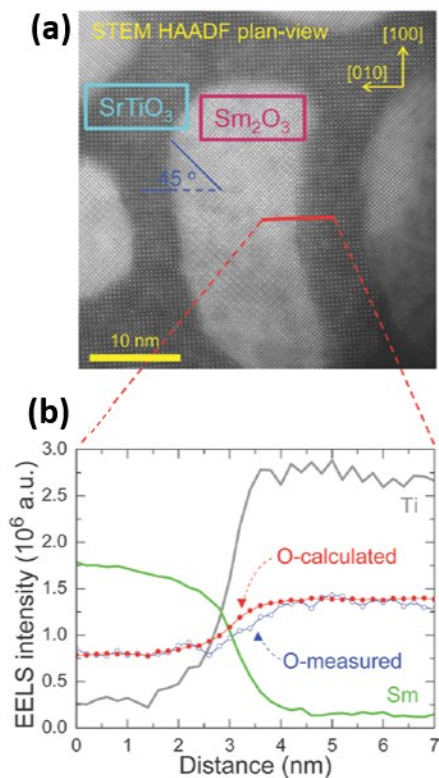


Figure 18. a) A plan-view HAADF-STEM image of a STO:Sm₂O₃ VAN. b) A EELS line scan across the vertical interface. EELS was measured along the red line in (a). Oxygen content calculated (red data) and oxygen content measured (blue data) were compared. Reproduced with permission.^[123] Copyright 2014, Wiley.

Author Manuscript

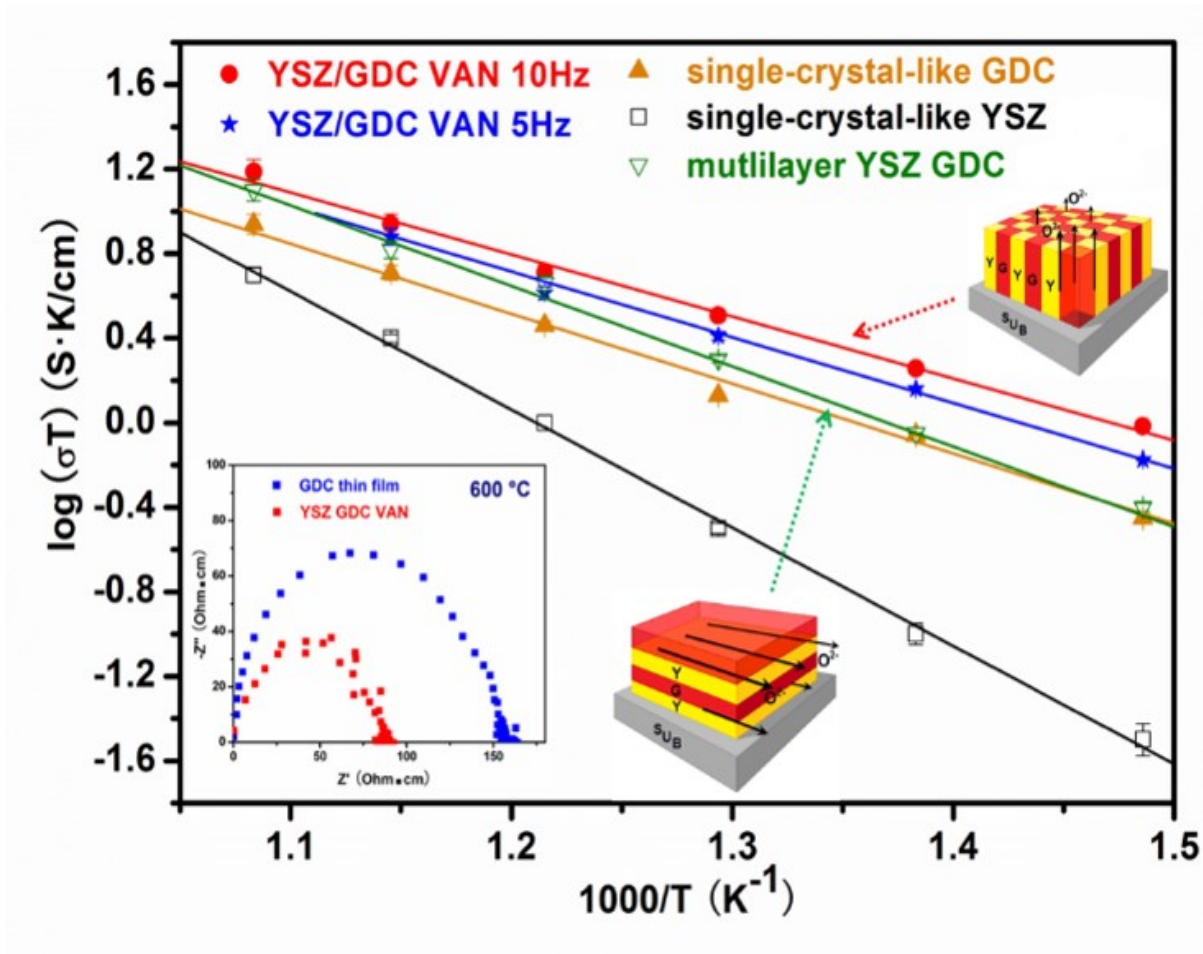


Figure 19. The temperature dependent ionic conductivity of the YSZ/GDC VAN electrolyte compared to the single-phase GDC and YSZ thin films. The inset is an impedance plot of the pure GDC film and a VAN film. Reproduced with permission.^[287] Copyright 2013, Wiley.

Author

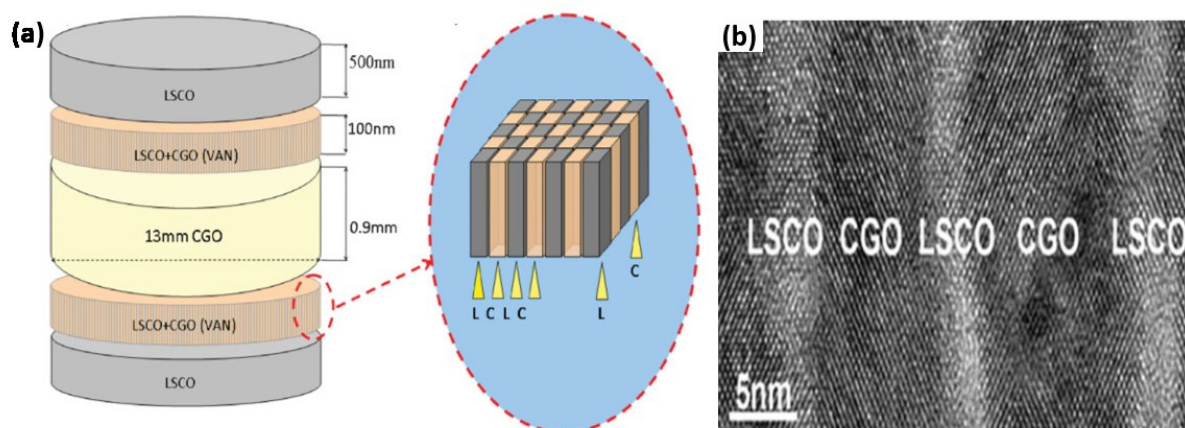


Figure 20. a) A schematic illustration of a symmetric SOFC cell with a VAN interlayer. “L” represents the LSCO phase and “C” stand for the GDC phase. b) A HRTEM image of the LSCO/GDC VAN. Reproduced with permission.^[303] Copyright 2009, Wiley.

Author Manuscript



Aiping Chen obtained his Ph.D. in Electrical Engineering from Texas A&M University and is currently a staff scientist at the Center for Integrated Nanotechnologies (CINT) at Los Alamos National Laboratory. He works on epitaxial growth of functional oxide heterostructures and nanocomposites with a focus on ferromagnetism, ferroelectricity and multiferroicity.

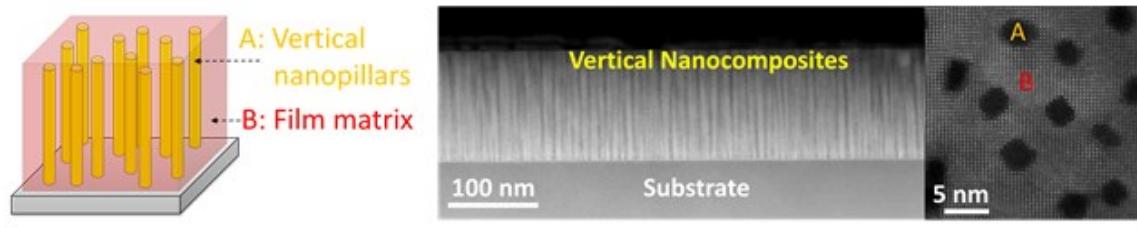


Quanxi Jia is an Empire Innovation Professor and National Grid Professor of Materials Research at the University at Buffalo (UB)—the State University of New York. He is also the Scientific Director of New York State Center for Excellence in Materials Informatics. Prior to joining UB in 2016, he was the Director of the Center for Integrated Nanotechnologies, a DOE Nanoscale Science Research Center operated jointly by Los Alamos and Sandia National Laboratories. His research includes the synthesis and study of structure–property relationships of nanostructured materials, multifunctional materials, and thin films, as well as the development of microelectronic/electro-optic devices.

TOC

Vertically aligned nanocomposite (VAN) thin films with controllable vertical interface, vertical lattice strain and defects have enabled tremendous research activities in a variety of complex oxides. Here, the remarkable progress achieved in VAN thin films is reviewed from a perspective of tuning functionalities through control of strain, defect and interface.

Keyword: Thin Films



Author